CHARACTERIZATION OF FLOW STRUCTURE AND WALL SHEAR STRESS IN PATIENT-SPECIFIC HEALTHY AND ANEURYSMAL ABDOMINAL AORTA PHANTOMS USING PARTICLE IMAGE VELOCIMETRY

A THESIS SUBMITTED TO
THE GRADUATE SCHOOL OF NATURAL AND APPLIED SCIENCES
OF
MIDDLE EAST TECHNICAL UNIVERSITY

BY

MEHMET ANIL SUSAR

IN PARTIAL FULFILLMENT OF THE REQUIREMENTS
FOR
THE DEGREE OF MASTER OF SCIENCE
IN
MECHANICAL ENGINEERING

SEPTEMBER 2023

Approval of the thesis:

CHARACTERIZATION OF FLOW STRUCTURE AND WALL SHEAR STRESS IN PATIENT-SPECIFIC HEALTHY AND ANEURYSMAL ABDOMINAL AORTA PHANTOMS USING PARTICLE IMAGE VELOCIMETRY

submitted by **MEHMET ANIL SUSAR** in partial fulfillment of the requirements for the degree of **Master of Science** i**n Mechanical Engineering, Middle East Technical University** by,

Prof. Dr. Halil Kalıpçılar
Dean, Graduate School of **Natural and Applied Sciences** _____

Prof. Dr. M. A. Sahir Arıkan
Head of the Department, **Mechanical Engineering** _____

Prof. Dr. Mehmet Metin Yavuz
Supervisor, **Mechanical Engineering, METU** _____

Examining Committee Members:

Prof. Dr. Cüneyt Sert
Mechanical Engineering, METU _____

Prof. Dr. Mehmet Metin Yavuz
Mechanical Engineering, METU _____

Assist. Prof. Dr. Ali Karakuş
Mechanical Engineering, METU _____

Assist. Prof. Dr. Özgür Uğraş Baran
Mechanical Engineering, METU _____

Assist. Prof. Dr. Onur Baş
Mechanical Engineering, TED University _____

Date: 06.09.2023

I hereby declare that all information in this document has been obtained and presented in accordance with academic rules and ethical conduct. I also declare that, as required by these rules and conduct, I have fully cited and referenced all material and results that are not original to this work.

Name Last name : Mehmet Anıl Susar

Signature :

ABSTRACT

CHARACTERIZATION OF FLOW STRUCTURE AND WALL SHEAR STRESS IN PATIENT-SPECIFIC HEALTHY AND ANEURYSMAL ABDOMINAL AORTA PHANTOMS USING PARTICLE IMAGE VELOCIMETRY

Susar, Mehmet Anıl
Master of Science, Mechanical Engineering
Supervisor : Prof. Dr. M. Metin Yavuz

September 2023, 136 pages

Abdominal Aortic Aneurysm (AAA) is an irreversible dilatation of the abdominal aorta, which can lead to rupture without proper screening and treatment, with an over 80% mortality rate for specific age groups. The enlargement of the abdominal aorta causes significant changes of hemodynamics in AAA with clear indications of flow separation and vortical structures. It is generally accepted that growth and rupture mechanisms of AAA are correlated with the disturbed hemodynamics and wall shear stress metrics such as time-averaged wall shear stress (TAWSS), oscillatory shear index (OSI), and endothelial cell activation potential (ECAP). In the present study, the flow structure and wall shear stress of patient specific healthy and aneurysmal abdominal aorta phantoms are characterized in physiological flow circulatory set-up using quantitative velocity measurement technique, particle image velocimetry (PIV). A method has been developed and implemented to calculate the wall shear stress (WSS) from PIV, which basically overcomes the difficulties of PIV both in extracting the exact wall location and in predicting the velocity gradients on the wall.

The results of the study show that the hemodynamics inside a dilated abdominal aorta differs from the healthy aorta significantly. The peak vorticity magnitude of the formed vortices in the AAA is approximately two times that of the healthy aorta. Considering the wall shear stresses, TAWSS values in the AAA sac are close to 0 Pa mainly due to flow separation, whereas it is about 0.1 Pa for most portions of the healthy aorta. There are two zones in the aneurysm, corresponding to separation and reattachment regions, with OSI values of 0.5, which is the maximum value the OSI can have. In addition, a substantial portion of the aneurysm has relatively larger ECAP values. On the contrary, the OSI and ECAP values are roughly 0 for the whole healthy aorta.

Keywords: Abdominal Aortic Aneurysm, Hemodynamics, Wall Shear Stress Parameters, Vortex Identification, Particle Image Velocimetry

ÖZ

HASTAYA ÖZEL SAĞLIKLI VE ANEVRİZMALI ABDOMİNAL AORT MODELLERİNDE AKIŞ YAPILARININ VE DUVAR KESME GERİLİMİNİN PARTİKÜL GÖRÜNTÜ VELOSİMETRİSİ KULLANILARAK KARAKTERİZASYONU

Susar, Mehmet Anıl
Yüksek Lisans, Makina Mühendisliği
Tez Yöneticisi: Prof. Dr. M. Metin Yavuz

Eylül 2023, 136 sayfa

Abdominal Aort Anevrizması (AAA) abdominal aortanın geri dönülemez bir biçimde genişlemesi olup, uygun takip ve tedavinin gerçekleştirilmediği durumlarda aortanın yırtılmasına sebep olabilir ve bu durum belirli yaş gruplarında %80'e varan bir ölüm oranıyla sonuçlanabilir. Abdominal aortanın genişlemesi AAA'nın içerisindeki hemodinamiklerde, akış ayrılmaları ve girdap yapılarının da görünür hale gelmesiyle, ciddi anlamda değişikliklere sebep olur. AAA'nın büyüme ve yırtılma mekaniklerinin bozulan hemodinamikler ve zaman ortalamalı duvar kesme gerilimi (TAWSS), salınımlı kesme indeksi (OSI) ve endotel hücre aktivasyon potansiyeli (ECAP) gibi duvar kesme gerilimi parametreleri ile ilişkili olduğu genel olarak kabul görmektedir. Bu çalışmada, hastaya özgü sağlıklı ve anevrizmalı abdominal aort modellerinin akış yapıları ve duvar kesme gerilmeleri, fizyolojik akış dolaşımı sağlayabilen deney düzeneğinde nicel bir hız ölçüm tekniği olan partikül görüntü velosimetresi kullanılarak karakterize edilmiştir. PIV'den duvar kesme gerilimi (WSS) hesaplamak için bir yöntem geliştirilmiş ve uygulanmıştır; bu yöntem, PIV'de WSS hesaplarken yaşanan duvar konumunun elde edilmesi ve

duvara yakın hız gradyanlarının tahmin edilmesi zorluklarının da üstesinden gelmektedir.

Bu çalışma, genişlemiş bir abdominal aorttaki hemodinamiklerin sağlıklı bir aorttakinden önemli ölçüde ayrıldığını göstermiştir. AAA'da oluşan girdapların maksimum büyüklüğü sağlıklı aortadakilerin yaklaşık iki katıdır. Duvar kesme gerilimleri incelendiğinde, AAA kesesindeki TAWSS değerleri akış ayrılmasına bağlı olarak 0 Pa'a yakınken, sağlıklı aortanın büyük bir bölümünde yaklaşık 0.1 Pa'dır. Anevrizmada akışın ayrıldığı ve yeniden tutunduğu alanlara denk gelen iki bölge bulunmaktadır. Bu bölgelerde OSI'nin alabileceği maksimum değer olan 0.5 gözlemlenmiştir. Buna ek olarak, anevrizmanın ciddi bir bölümünde görece daha büyük ECAP değerlerine rastlanmıştır. Öte yandan, sağlıklı aortadaki OSI ve ECAP değerleri yaklaşık olarak 0'dır.

Anahtar Kelimeler: Abdominal Aort Anevrizması, Hemodinamik, Duvar Kesme Gerilimi Parametreleri, Girdap Tanımlama, Partikül Görüntü Velosimetrisi

To my family

ACKNOWLEDGMENTS

This thesis has been conducted in collaboration with Qatar University under Qatar University International Research Collaboration Co-Funds (IRCC) Program (IRCC 2020-002).

First of all, I would like to express my sincere gratitude to my supervisor Prof. Dr. M. Metin Yavuz for his guidance, support and confronting attitude throughout this study. With his sincere help and advices these three years became so much easier.

I would like to thank to my parents Bediriye and Şeref Susar and my sister Ayça Arı for their unlimited support and love throughout not only this study but my whole life. My heartfelt thanks go to my sister Aylin Susar Arı. I consider myself an incredibly lucky person to have her in my life, providing her unwavering support and love. Thank you for always being there for me whenever I need. I also would like to express my gratitude to my brother in law Evrim Onur Arı. Thank you for being everything I could ask for in a brother, one I don't have. My special thanks go to Deniz Öztunç. My gratitude for her support in my life cannot be expressed in words.

I also would like to thank to my friends in the research group Amirhossein Fathipour, Oğuzhan Yılmaz and Kerem Tuğ Gökçek. Finally I want to thank to Mr. Mehmet Özçiftçi for his technical support and guidance.

TABLE OF CONTENTS

LIST OF TABLES

TABLES

LIST OF FIGURES

FIGURES

LIST OF ABBREVIATIONS

ABBREVIATIONS

AAA	=	Abdominal Aortic Aneurysm
PIV	=	Particle Image Velocimetry
WSS	=	Wall Shear Stress
TAWSS	=	Time Averaged Wall Shear Stress
OSI	=	Oscillatory Shear Index
ECAP	=	Endothelial Cell Activation Potential
EVAR	=	Endovascular Aneurysm Repair
PDMS	=	Polydimethylsiloxanne
BMF	=	Blood Mimicking Fluid
RI	=	Refractive Index
MRV	=	Magnetic Resonance Velocimetry
LDV	=	Laser Doppler Velocimetry

LIST OF SYMBOLS

SYMBOLS

Re	=	Reynolds Number
Re_m	=	Mean Reynolds Number
ρ	=	Fluid Denisty
u_m	=	Mean Flow Velocity
D	=	Diameter of the AAA Inlet
μ	=	Dynamic Viscosity
α	=	Womersley Number
ω	=	Angular Frequency
Stk	=	Stokes Number
ρ_p	=	Particle Density
D_p	=	Particle Diameter
V	=	Flow Velocity
L	=	Characteristic Length of the Flow Domain
$\underset{u}{\rightarrow}$	=	Velocity Field Vector
Δ	=	Δ Criterion
λ_{ci}	=	λ_{ci} Criterion
Q	=	Q Criterion
λ_2	=	λ_2 Criterion

CHAPTER 1

INTRODUCTION

Aorta is the first portion of the arterial system to which the blood is exerted directly from the heart. The blood requirement for all tissues and organs in the human body is met with the branching of the aorta. The three main portions of the human aorta are the aortic arch, descending thoracic aorta, and abdominal aorta as shown in Figure 1.1.

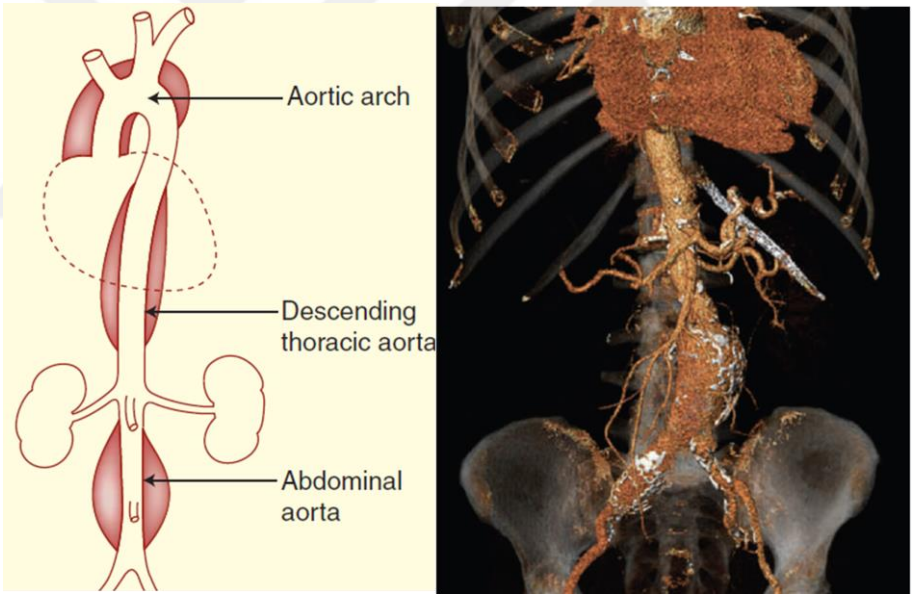

Figure 1.1. (Left) The structure and aneurysm susceptibility of the human aorta (Kuivaniemi et al., 2015), (Right) CT scan of an AAA taken from a male patient aged 76 years (Nordon et al., 2010)

Abdominal Aortic Aneurysm (AAA) is the irreversible dilatation of the abdominal aorta, which has diameters 3 cm and larger (might even exceed 5 cm in extreme cases) (Wanhainen et al., 2016), where the average diameter for the abdominal aorta is approximately 2 cm

Even though the exact mechanism behind the formation of the AAA is still unknown, the strong correlation between the AAA and aging is evident from the screening programs (Davis et al., 2013; Karthikesalingam et al., 2014; Wanhainen et al., 2016). These screening programs indicate that nearly 1.5% of the population above 65 has AAA. In addition, the mortality rate of the AAA can exceed 80% in case of the rupture.

Researchers argue that the hemodynamics inside the abdominal aorta strongly affects the formation and rupture of the AAA (Finol & Amon, 2002; Salsac et al., 2006). Even in early studies, researchers reported that flow physics inside an AAA change considerably (Yu, 2000) and might involve quite complex flow structures including flow separations and vortex rings with recirculation regions and jet flows during a cardiac cycle. In line with the hemodynamics in AAA, wall shear stress patterns and metrics such as time-averaged wall shear stress (TAWSS), oscillatory shear index (OSI), and endothelial cell activation potential (ECAP) indicate quite different and complex behavior both in magnitudes and trends, and thus must be well understood.

1.1 The Motivation of the Study

AAA is a frequently seen disease in elderly population. Without proper precautions, AAA keeps dilating and results in rupture. In depth analysis of AAA and preventive treatments can save thousands of people annually. It is generally accepted that growth and rupture mechanisms of AAA are correlated with the disturbed hemodynamics and wall shear stress metrics. In experimental point of view, accurate prediction or direct measurement of wall shear stress is quite challenging. Therefore, characterization of flow fields and shear stress for patient-specific aortas and

aneurysmal phantoms, and detecting regions with vortical structures and abnormal WSS fields by means of experimental techniques contribute to understanding of mechanisms behind AAA.

1.2 The Aim of the Study

In the present study, the flow structure and wall shear stress of patient specific two sylgard optically transparent phantoms, one healthy and one aneurysmal abdominal aorta, are characterized in physiological flow circulatory set-up using two-dimensional particle image velocimetry (PIV). A method has been developed and implemented to calculate the wall shear stress (WSS) from PIV, which basically overcomes the difficulties of PIV both in extracting the exact wall location and in predicting the velocity gradients on the wall. Phase-averaged streamlines patterns, vorticity contours, swirling strength, and wall shear stress distributions are presented along with the wall shear stress metrics including time-averaged wall shear stress (TAWSS), oscillatory shear index (OSI), and endothelial cell activation potential (ECAP).

1.3 The Outline of the Thesis

This thesis is composed of five chapters. The first chapter provides introductory information about abdominal aortic aneurysms and summarizes the aim and the motivation of the study.

The second chapter summarizes the literature survey, explains the cardiovascular system, and investigates the reasons behind the AAA. Aneurysm models, the blood-mimicking fluids, and the vortex identification methods along with the WSS metrics are also discussed in this chapter.

The third chapter presents the experimental setup including the physiological flow circulatory system and the components of the measurement techniques. Data processing and error control are also explained.

The fourth chapter demonstrates the results obtained from the PIV measurements for patient-specific healthy aorta and AAA. The identified vortex and WSS patterns are discussed in detail. WSS metrics are also calculated and presented.

Finally, the fifth chapter provides the conclusions throughout the study together with the possible recommendations for the future work.

CHAPTER 2

LITERATURE REVIEW

2.1 Cardiovascular System

It is convenient to explain the cardiovascular system before explaining Abdominal Aortic Aneurysms. The cardiovascular system consists of three components. These are the heart, blood vessels, and finally, the blood. The primary function of the cardiovascular system is to carry the necessary materials to the rest of the body. Oxygen, glucose, water, and amino acids are examples of these materials. Also, the metabolic waste and CO_2 produced by the organs are collected by the cardiovascular system (Aaronson et al., 2013, p. 13).

2.1.1 Blood

Blood is the fluid that hosts the necessary materials for the body. It mainly comprises plasma, erythrocytes (red blood cells), and white blood cells. Plasma is an aqueous solution with red and white blood cells, proteins, and electrolytes. An average 70 kg human has 5-5.5 liters of blood.

Mechanical properties of the blood is another crucial aspect of this study. Blood is, in fact, a shear-thinning fluid which makes it non-Newtonian. The viscosity of a shear-thinning fluid decreases with the increasing shear rate. This property of the blood can be explained entirely by the structure of the red blood cells. Red blood cells form rouleau-like structures when the exerted shear stress on the blood is low. These rouleau-like structures cause the interlocking of the red blood cells, resulting in increased flow resistance (Hoskins & Hardman, 2017). But since the shear rates in large portions of arteries are high, it is valid to assume blood as a Newtonian fluid in most of the arteries. On the other hand, it should also be considered that low-shear

rate areas can exist in aneurysms. These areas may be a small portion of the aneurysm, but Newtonian fluid assumption can still decrease accuracy. In this study, blood is assumed as a Newtonian fluid.

2.1.2 Heart

A pump is needed to transport blood to the rest of the body. The heart acts as a positive displacement pump in the human body. It has four chambers that can contract and relax. These four chambers are called ventricles and atriums. Contraction of the left ventricle causes an internal pressure increase from 0 mmHg to 120 mmHg. The pressure increase in the left ventricle opens the aortic valve and pushes all the oxygen-rich blood to the aorta. This phase, where the internal pressure increases, is called systole. Another phase in the cardiac cycle is called diastole, where the ventricles are relaxed. With the diastole phase, internal pressure in the left ventricle returns to 0 mmHg, but the aortic pressure does not return to 0 mmHg. Aortic pressure decreases to 80 mmHg since it has elastic walls and dampens some of the pressure. This pressure waveform in the aorta strongly affects the vortex formation inside an aneurysm. Pressure waveform during systole and diastole and the heart's structure can be seen in Figures 2.1 & 2.2

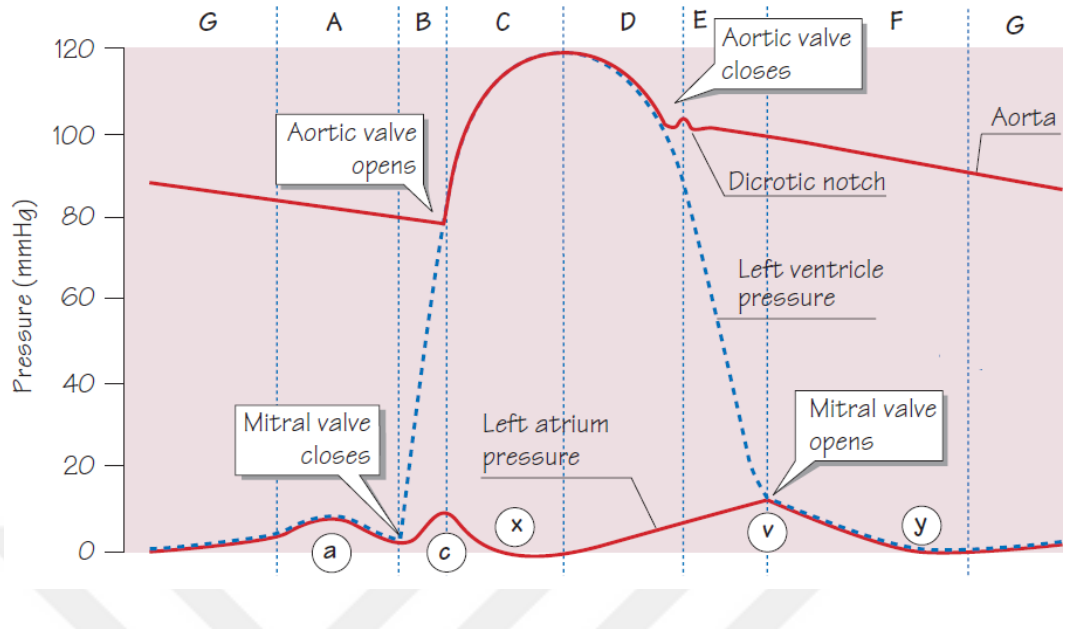

Figure 2.1. Pressure waveform during a cardiac cycle (Aaronson et al., 2013).

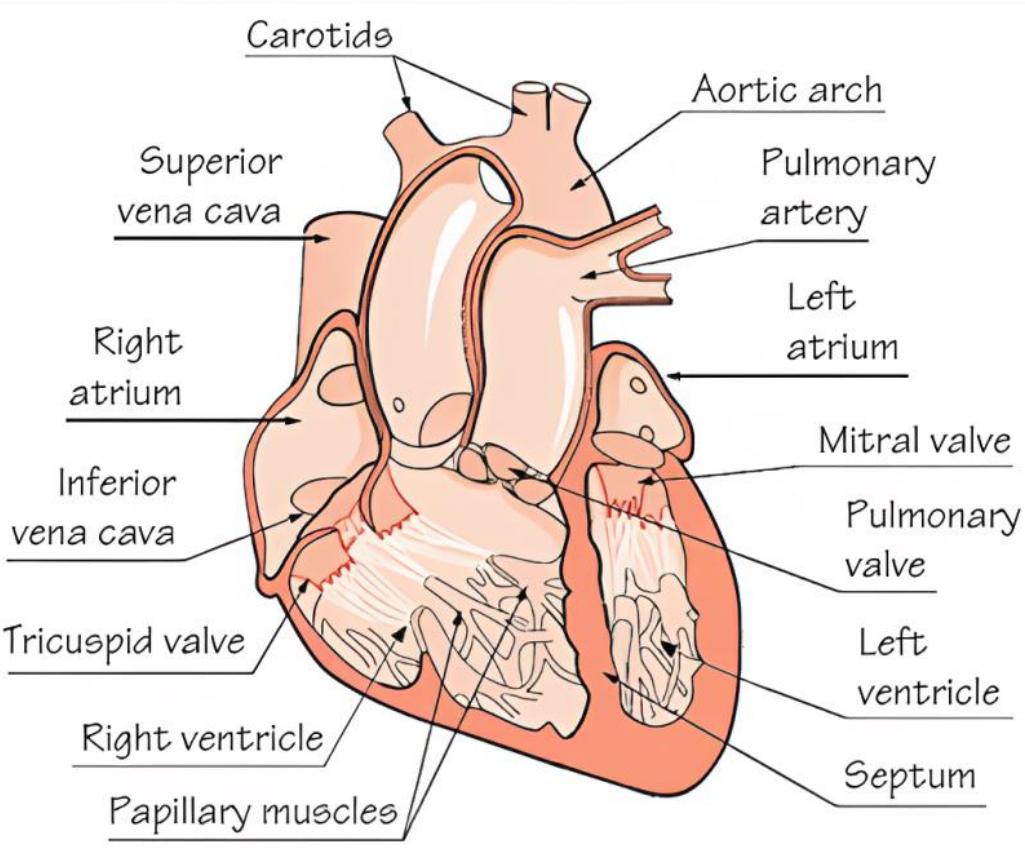

Figure 2.2. Structure of a human heart (Aaronson et al., 2013).

2.1.3 Arteries

The third and final component of the cardiovascular system is the arteries. Arteries are the cardiovascular system's transportation mediums that carry blood to tissues and organs. Arteries consist of three main layers and form a closed loop inside the body. In that sense, it is different from the other systems in the human body, like the excretory and respiratory systems, which are open systems. Blood that is pumped from the heart directly gets into the aorta. This single vessel is then divided consecutively with the increasing distance from the heart and forms an arterial network by capillaries in the human body. The anatomy of the aorta can be seen in Figure 2.3.

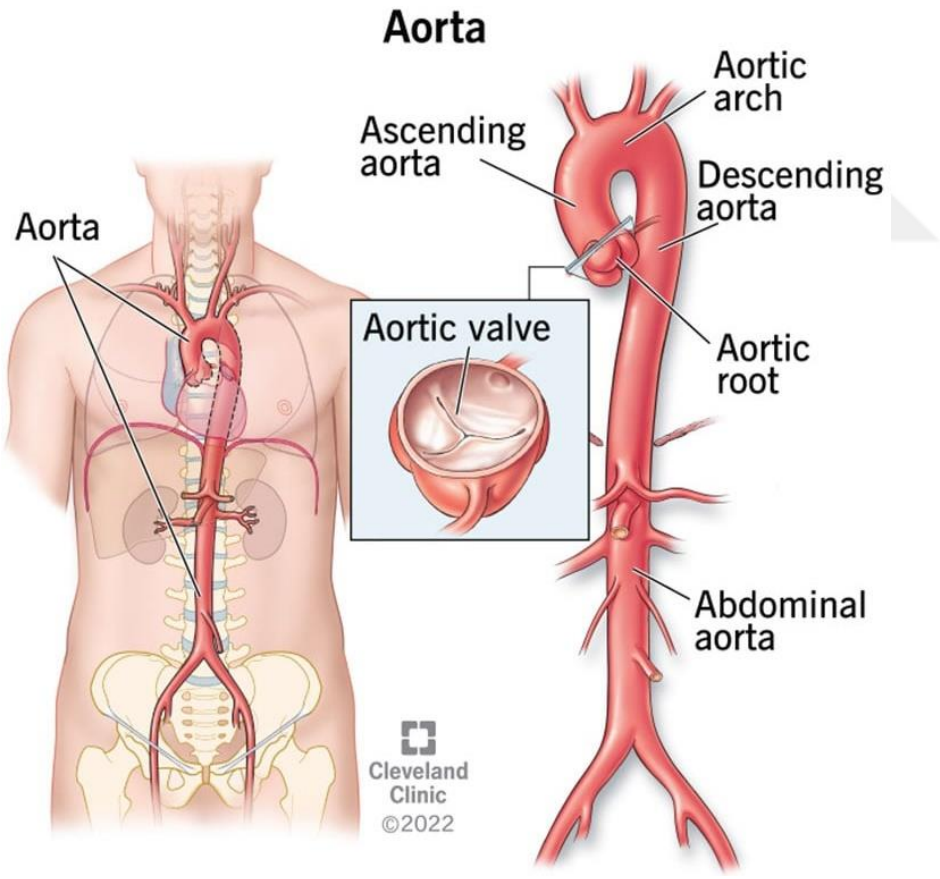

Figure 2.3. The anatomy of the aorta. (Cleveland Clinic, n.d.)

Physical properties of the arteries also change with the distance to the heart. Arteries stiffen with the increasing distance from the heart, and that causes a higher difference between maximum and minimum pressures inside the arteries. Pulse pressure is the difference between an artery's maximum and minimum pressure. While pulse pressure in the aorta is 110 mm Hg, the pulse pressure in the legs is measured as 160 mm Hg. This characteristic can be seen in Figure 2.4.

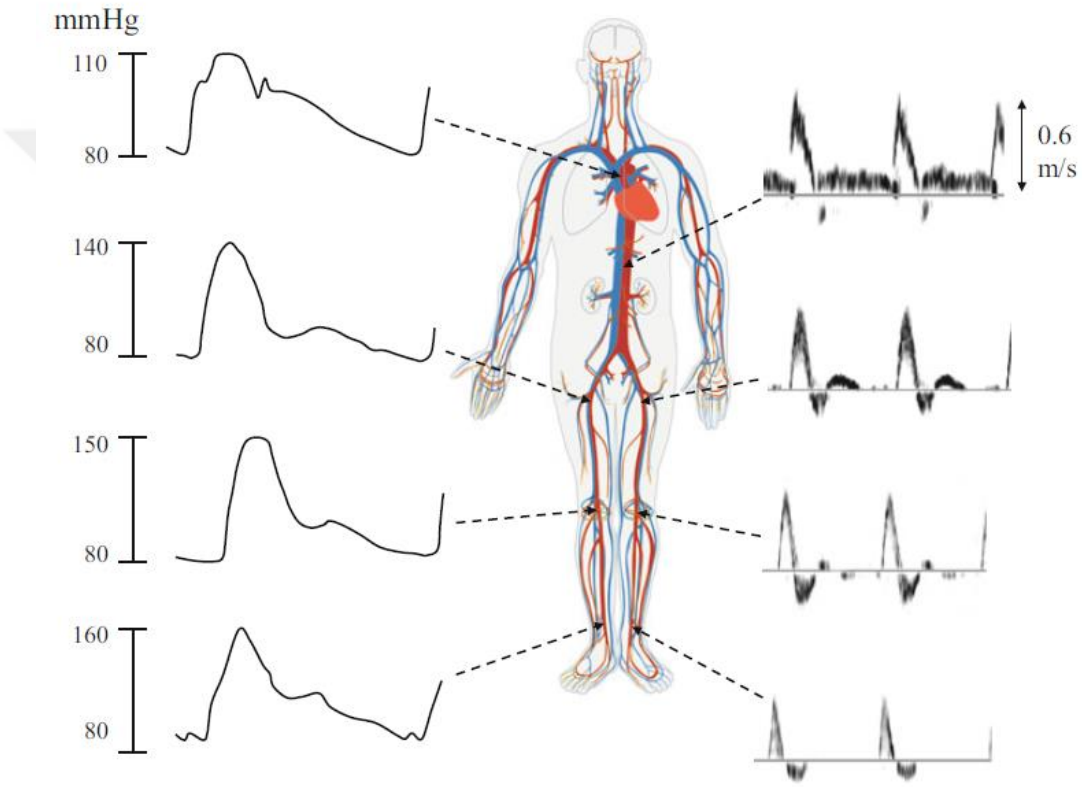

Figure 2.4. Varying pulse pressures in the human body (Hoskins & Hose, 2017).

Besides pressure, the Reynolds number of the blood flood also varies with the distance. Maximum Reynolds numbers of 4000-5000 are obtained in the ascending aorta at the peak systole phase. Apart from the ascending aorta at peak systole, the Reynolds number in the arteries is below 2000, indicating a laminar flow. The mean

Reynolds number in the arterial system decreases with the increasing distance from the heart (Hoskins & Hose, 2017).

Arterial vessels consist of three main layers. These layers are called adventitia, media, and intima. Adventitia is the outmost layer with a structure formed heavily by collagen fibers. The innermost layer of the vessel wall is intima. Intima is in contact with the blood, and a single layer of endothelial cells forms this layer. Between these two layers, there is media which consists of elastin sheets. Adventitia and media layers are critical for the mechanical properties of the vessel. The ratio of elastin and collagen is the main parameter that determines the physical characteristic of an artery. A higher ratio of elastin/collagen means a softer arterial vessel, whereas a lower elastin/collagen ratio means stiffer arterial vessels (Hoskins, 2017). The structure of an arterial wall can be seen in Figure 2.5.

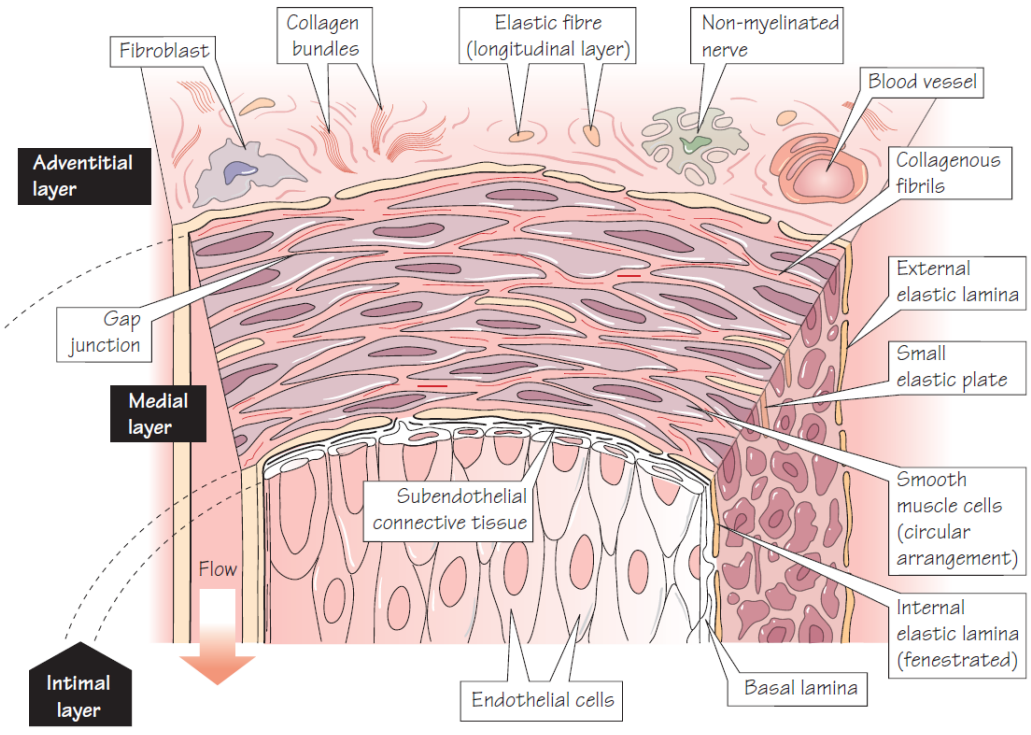

Figure 2.5. Structure of an arterial wall (Aaronson et al., 2013)

While the aorta is the first section of the arterial system after the heart, it also has a high elastin/collagen ratio. This characteristic makes the aorta a soft, elastic artery prone to aneurysms. With the effect of the flow waveform created by the heart, the aorta consecutively expands and contracts to dampen the pressure. This consecutive expansion and contraction results in fatigue stress over the years. With the decrease in elastin and increase in collagen at the arterial wall with aging, the abdominal aorta loses its elastic structure. Average wall motion is measured as 2 mm in the healthy aorta and 1 mm in the aorta with an aneurysm (Wilson et al., 2003). In some cases, loss of elastic characteristics results in failure in damping the pressure. The aortic vessel changes its shape with time to withstand the forces inside the artery (Doyle & Hoskins, 2017). To adapt to new conditions, it enlarges and forms a fusiform shape. This dilatation in diameter and fusiform formation in the abdominal aorta is called as Abdominal Aortic Aneurysm.

2.2 Abdominal Aortic Aneurysm (AAA)

2.2.1 Statistics About the Abdominal Aortic Aneurysms

AAA can lead to rupture without proper screening and surgical interventions at the correct time. In most cases, the rupture of the AAA ends with the patient's death. According to data from the Centers for Disease Control and Prevention (CDC), AAA led to 9.904 deaths in 2019 in the USA. In 2013 this number was 14.000 (Centers for Disease Control [CDC], 2019). These statistics create a necessity for screening programs for people over 65. Sweeden and the United Kingdom started this screening program. The Swedish Nationwide Abdominal Aortic Aneurysm Screening Program began its operations in 2006. 302.957 men over 65 were invited to this study, and 84% attendance was obtained. Abdominal Aorta diameter larger than 3 cm is accepted as an aneurysm, and 1.5% of the participants are diagnosed with AAA (Wanhainen et al. 2016). The United Kingdom carried out another screening program. This study also accepted an aorta diameter larger than 3 cm as

an aneurysm. From 2009 to 2012, 157.730 males over 65 attended this screening program. 1.57 % of the participants are diagnosed with AAA (Davis et al., 2013). While the occurrence of AAA varies with age, gender, and race, these two screening programs concluded that nearly 1.5 % of the elderly population is diagnosed with AAA.

The occurrence possibility of AAA is also strongly dependent on smoking habits. In a study published in 2011, using the data obtained by the Swedish AAA Screening Program, it is seen that nearly 87% of the patients diagnosed with AAA have smoked at some point in their lives. And approximately 33 % of the patients were still smoking (Svensjo et al., 2011). This strong correlation between smoking habits and AAA mortality can be seen in Figure 2.6. Another factor that has a strong connection with AAA formation is hypertension. In the same study, it is observed that nearly 55 % of AAA patients also have hypertension.

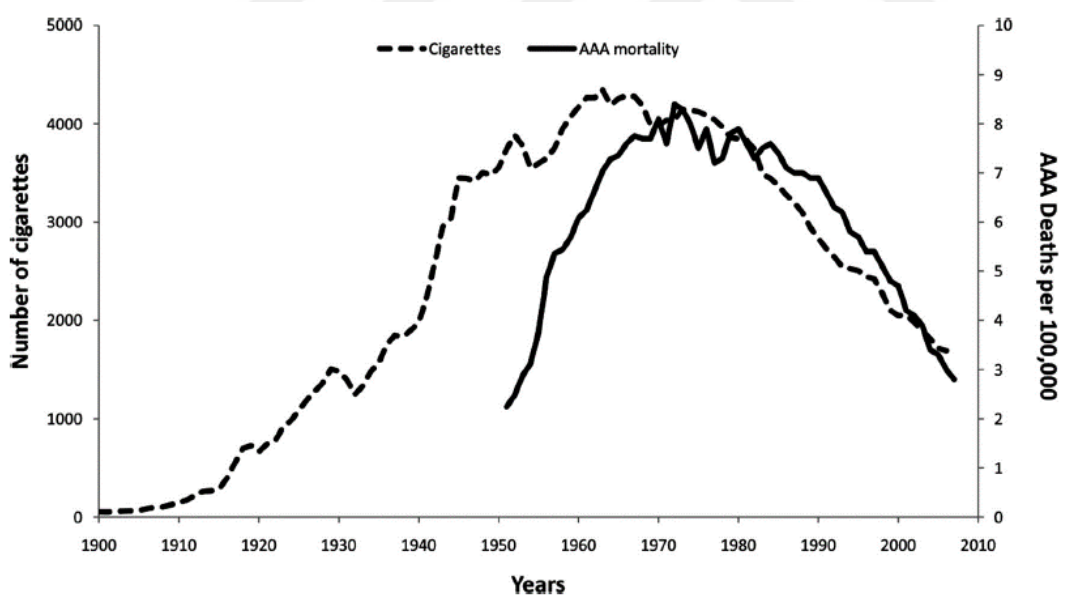

Figure 2.6. Correlation between smoking and AAA mortality (Lederle, 2011).

Mortality rates are another reason that brought the necessity for screening programs. Without the diagnosis and proper screening of the AAA, it can lead to rupture. In the case of rupture, depending on the patient's age, mortality rates can go over 80 % (Karthikesalingam et al., 2014). This can be seen in Figure 2.7. From Figure 2.7, it is also visible that England's mortality rates are higher than in the USA. This trend is explained by more surgical intervention and reparative treatment in the USA (Karthikesalingam et al., 2014). The visible decrease in the mortality rates with surgical intervention and treatment also explains the importance of screening possible AAA patients.

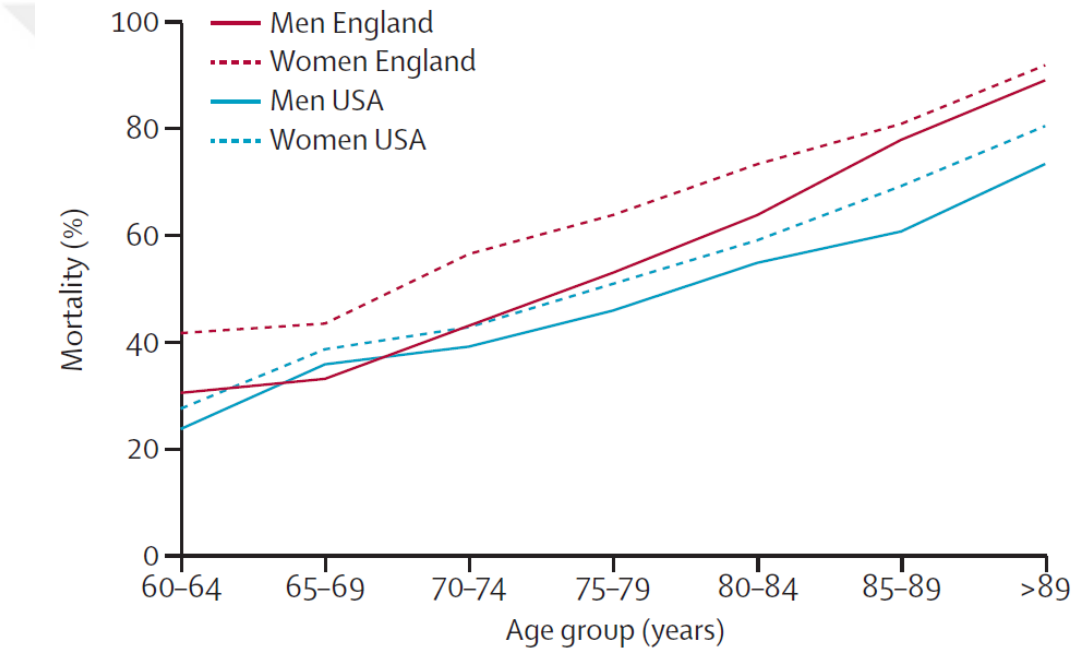

Figure 2.7. Mortality rate vs. patient age. The data is collected for both women and men separately in England and USA (Karthikesalingam et al., 2014).

2.2.2 Symptoms of AAA

It should be noted that most of the AAA cases are asymptomatic and diagnosed after the rupture. This characteristic is another factor that makes it fatal. But in some cases, AAA patients can feel pains and pulsatile mass in the abdominal area. Low blood pressure and loss of consciousness can also indicate the presence of AAA (Doyle & Hoskins, 2017).

2.2.3 Treatment of AAA

Screening potential AAA patients is the first step toward diagnosis and treatment. These screening programs accept abdominal aorta diameters larger than 3 cm as aneurysms and follow the growing rate of the aneurysm with measurements every six months. Patients having an initial abdominal aorta diameter larger than 5.4 cm are evaluated for open surgery (Darwood et al., 2012). This evaluation includes a general health scan of the patient and any possible calcification on the aneurysm wall. Assessment is usually done by the CT scan of the aneurysm (Hoskins et al., 2011). The aortic aneurysm is removed and replaced with a synthetic implant in open surgery. This implant is stitched to the remaining abdominal aorta. Thrombus formation inside the aorta is observed frequently in AAA patients. Existing thrombus is also removed during this operation (Doyle & Hoskins, 2017).

Endovascular aneurysm repair (EVAR) replaces open surgery to reduce postoperative mortality rates. In EVAR, a stent inserted from the femoral arteries is placed inside the AAA. With the introduced stent, aneurysm walls are bypassed, and the stent is exposed to the forces exerted by the blood flow. The main problem of the first-generation EVAR operations was the slippage of the inserted stents. Due to the high forces exerted on the stent, leakage, and tearing of the inserted stents were also possible. Leakage and slippage of the inserted stent are fatal since the blood fills the cavity between the stent and the aneurysm. This leaked blood pressurizes the weak aneurysm wall and causes rupture. New-generation AAA stents are designed to

prevent these fatal failures with improved fixation and strength of the stent. With all these improvements, EVAR is the dominant treatment method for AAA patients (Carbett et al., 2011; Hoskins et al., 2011).

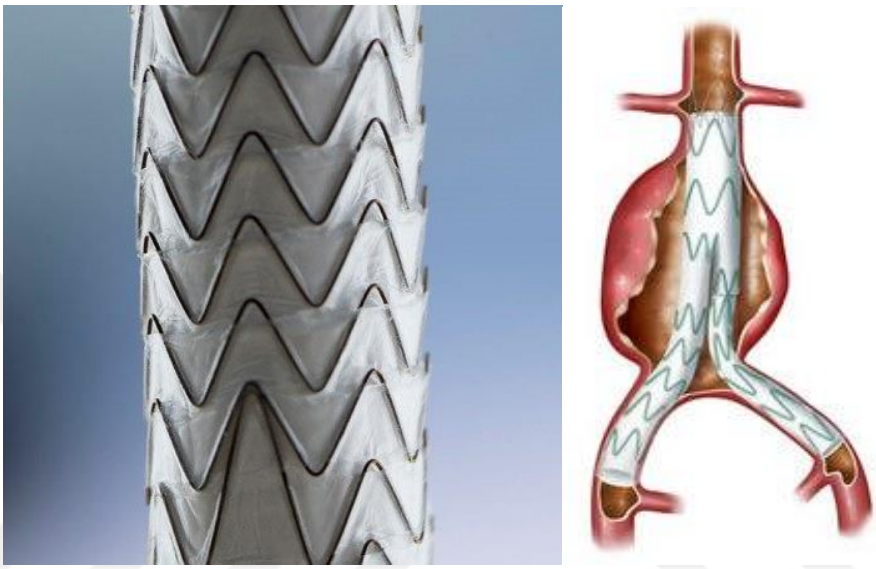

Figure 2.8. Closed-up view of a stent graft (Left) and treatment of AAA with the EVAR method (Right). Retrieved from clevelandclinic.org (Left), circulationfoundation.org.uk (Right)

2.3 Experimental Setup

There are four primary considerations in the experimental setup that investigates abdominal aneurysms. These are the aneurysm phantoms that simulate abdominal aneurysms, blood-mimicking fluids that model the characteristics of blood, the flow pattern provided to the aneurysm, and the flow measurement system used to obtain the velocity field inside the aneurysm. These components can vary according to the objectives of the study.

2.3.1 Aneurysm Phantom

These phantoms can be divided into two groups, rigid and compliant, according to their compliance characteristics. Another criterion used to categorize the phantoms is their shapes. They can be simple geometries, generally elliptic, and used to study basic flow characteristics inside an aneurysm. Patient-specific geometries can also be used in aneurysm studies to provide a more realistic flow field.

The earliest experimental aneurysm studies employed simple geometries as their phantom due to simplicities in production. Asbury et al. (1995) used a rigid symmetric elliptic model as the aneurysm phantom. The material of the aneurysm model is selected as Sylgard 184, and it is cast to form a solid fusiform. Bluestein et al. (1996) also used a simple elliptic model for numerical and experimental investigations. To have a rigid phantom, experimental fusiform is manufactured using glass.

The effect of geometrical parameters on flow characteristics is also investigated using various simple models. Egelhoff et al. (1999) used four symmetric and one asymmetric simple model to investigate this effect. Four rigid, symmetric phantoms with various diameters are produced using acrylic, and the flow physics is compared.

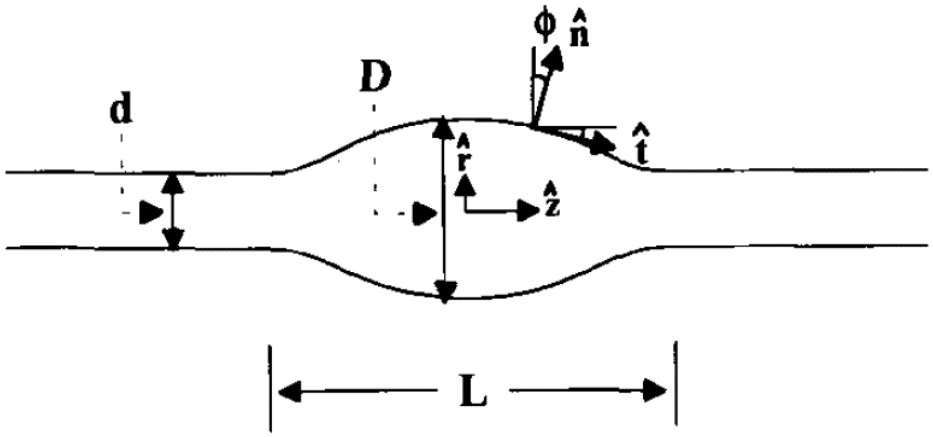

Figure 2.9. Simple elliptic aneurysm geometry used by Asburry et al. (1995)

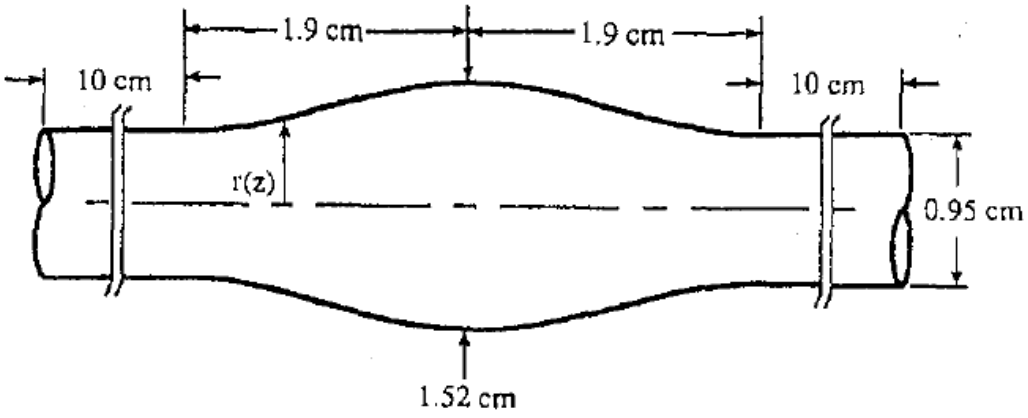

Figure 2.10. Simple elliptic aneurysm geometry used by Blustein et al. (1996)

AAA Model Sizes

Model	$\frac{L}{d}$	$\frac{D}{d}$	$\frac{Area_{bulge}}{Area_{inlet}}$
1	4.0	1.3	1.69
2	4.0	1.5	2.25
3	4.0	1.8	3.24
4	4.0	2.1	4.41
5	4.0	1.8	4.16

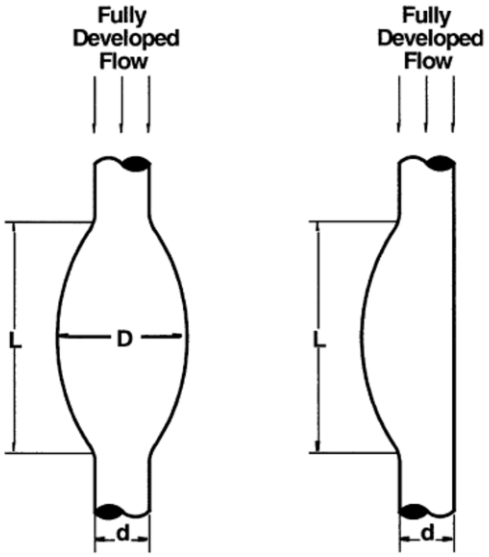

Figure 2.11. Simple aneurysm geometries used by Egelhoff et al. (1999)

With the developments in vascular imaging and being able to export these images as Standard Tessellation Language (STL) files, producing patient-specific aneurysms became much more accessible. Generally, this STL file is sent to a 3D printer, and an aneurysm model is printed using a polymer (Salman et al., 2019). This 3D-printed aneurysm model is used as the male mold, and the patient-specific aneurysm phantom is cast around the 3D-printed mold. Sylgard 184, Sylgard 170, and Sylgard 160 are the most commonly used materials for aneurysm phantoms since they can be easily cast into complicated patient-specific geometries. Sylgard 184, 170, and 160 are examples of Polydimethylsiloxane (PDMS), a type of elastomeric polymer.

PDMS is cured by adding a cross-linking agent and applying heat. Changing the curing method changes the mechanical properties of PDMS. With varying curing methods, the stiffness and elastic modulus of the PDMS can change (Kim et al., 2021). Therefore PDMS can be used for producing both rigid and compliant aneurysm phantoms. This property of the PDMS makes it advantageous over other materials.

Stamatopoulos et al. (2010) used patient-specific aneurysm phantom in their studies. Aneurysm geometry is obtained from a patient via CT scan, and using this scan, a mold is prepared with a 3D printer. This mold is submerged into Sylgard 184, and the rigid aneurysm phantom is obtained.

Deplano et al. (2016) also included aortic compliance effects in their studies. They used a simple model molded from Estane 5714 since this material has similar compliance characteristics with the actual abdominal aortic aneurysm.

To sum up, aneurysm geometries and materials used to produce these phantoms can vary according to the objective of the studies. If the study investigates basic flow characteristics inside an aneurysm, simple elliptic geometry produced from glass can be sufficient. Rigid and stationary phantom walls can be used in wall shear stress studies since the wall location can be determined precisely. Elastomeric polymers

with adequate wall thickness and glass can provide this rigidity. One should consider using elastomers to study the flow field inside a patient-specific aneurysm experimentally. Depending on the curing method and wall thickness, these elastomers can provide rigid or compliant phantoms. Sylgard is the most widely used elastomeric polymer in aneurysm studies and is also used in this study.

2.3.2 Blood Mimicking Fluid

Blood-mimicking fluid (BMF) is another crucial component of the experimental setup. The candidate fluid should meet two primary criteria to be selected as the BMF. The first criterion is to reflect the physical characteristics of the blood accurately. The second criterion is a suitable refractive index that can be used with optical measurement instruments.

As discussed above, blood is a non-Newtonian fluid with shear-thinning properties. Low shear rates cause the interlocking of the red cells and increase the viscosity values (Hoskins & Hardman, 2017). At shear rates higher than 100 s-1, the viscosity of the blood in a healthy human approaches a near-constant value of 3.5 mPa s. This trend can be seen in Figure 2.12.

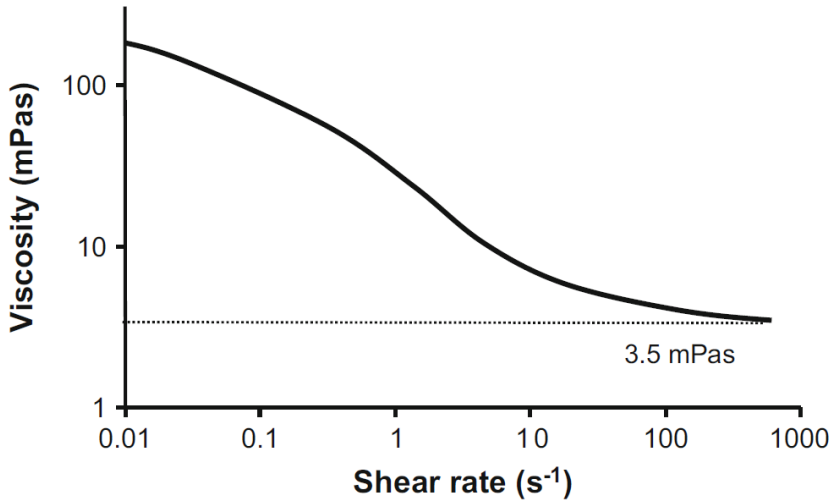

Figure 2.12. Change in blood viscosity with respect to shear rate (Hoskins & Hardman, 2017)

Other than viscosity, density is another physical parameter that determines the flow characteristics of the blood. Since human blood is a heterogeneous fluid, it is difficult to determine its density precisely. But it is stated that modeling blood as an incompressible fluid with a density of 1056 kg/m3 is accurate enough (Hose & Doyle, 2017).

Another criterion that should be considered is the refractive index of the BMF. Since optical measurement systems like PIV are the most widely used methods in experimental aneurysm studies, refractive index match of the BMF with the aneurysm phantom is crucial. Not having a refractive index match between BMF and the aneurysm phantom can cause optical distortions. These optical distortions decrease the accuracy of the flow field measurements significantly. Optical distortions can be effectively seen with the help of grid papers. Yousif et al. (2009) showed this phenomenon in their studies. They developed a fluid with an optimal refractive index match with the Sylgard 184. The effect of even minor deviations between refractive indexes can be seen in Figure 2.13.

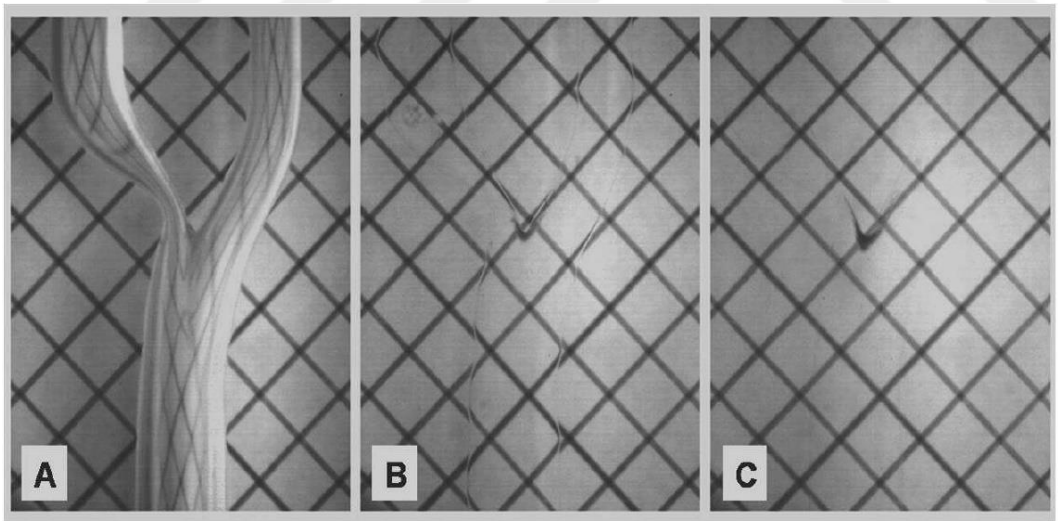

Figure 2.13. Visual distortions resulted from poor RI match (A), near-perfect match (B), and perfect RI match (C), (Yousif et al., 2009).

Yousif et al. (2009) reported the refractive index of Sylgard 184 as 1.414. Image A shows the distortions caused by significant refractive index deviation between the air and Sylgard 184. The effect of a slight variation between the Sylgard 184 and the fluid with a refractive index of 1.4110 is also visible in Image B. The perfect refractive index match between the developed BMF and the aneurysm phantom is visible in Image C.

Researchers generally use a mixture of water and glycerin with varying proportions to ensure similar mechanical behaviors with the blood. To have a near-perfect refractive index match with the aneurysm phantoms manufactured from PDMS, sodium-based salts are added to the mixture as the third component.

In one of the earlier studies, Yu (2000) used a mixture of water and glycerol. A third component was not added to adjust the refractive index since a phantom produced from the glass was used in this study. Yu reported the BMF to have 3.5 mPa·s of viscosity & 1121 kg/m3 of density.

Yousif et al. (2009) proposed a new BMF for the perfect refractive index match with the Sylgard 184. The proposed BMF was prepared with 47.38 % water, 36.94% glycerol, and 15.68 % sodium iodide salt by weight. The viscosity of the fluid was reported as 4.31 ± 0.03 mPa·s. Besides optimum refractive index match and acceptable viscosity value, the fluid shows discoloration due to ionization. This shortens the lifetime of the BMF considerably.

Stamatopoulos et al. (2010) used a mixture of 40 % water and 60 % glycerol by volume as the BMF with the aneurysm phantom produced from Sylgard 184.

In 2018 Brindise et al. proposed urea as the third component of the water-glycerol mixture to adjust the refractive index. With urea as the third component, the refractive index range of the BMF becomes suitable for PDMS phantoms. It is advantageous since urea does not cause discoloration and is less expensive than sodium-based salts. Urea causes small increases in the water-glycerol mixture's density and viscosity. In contrast, sodium-based salts cause a minor change in

viscosity and a significant increase in density. Physical properties of the 44.07% water, 34.52% glycerol, and 21.41% urea mixture (by weight) were reported as 4.18 mPa·s of viscosity and 1114 kg/m3 of density. The refractive index of this mixture was also reported as 1.4124.

As discussed above, blood shows shear thinning behavior at low shear stress. Although these low shear stress values do not exist in large arteries of healthy humans, AAAs can have small areas with low shear stress values. For that reason, some researchers used BMF with non-Newtonian characteristics. To make the BMF non-Newtonian, Xanthan-gum addition is the most widely used method. Deplano et al. (2014) investigated the flow field inside a simple geometry with a non-Newtonian BMF. 350 ppm of Xanthan gum is added to the water-glycerol mixture. The refractive index match is adjusted with the sodium salt. Brindise et al. (2018) reported that Xanthan gum addition could also be used with urea effectively.

2.4 Dimensionless Parameters to Consider for Flow Characteristic

2.4.1 Reynolds Number (Re)

Reynolds number is one of the primary parameters that determine flow characteristics in a pipe flow. It is the ratio of inertial forces to viscous forces in a flow. Mean Reynolds number at the AAA inlet can be calculated using the equation below (Çengel & Cimbala, 2006).

$$Re_m = \frac{\rho u_m D}{\mu} \tag{2.1}$$

Where:

ρ : Density of the fluid [kg/m^3]

u_m: Mean flow velocity at the AAA inlet [m/s]

D: Diameter of the AAA inlet [m]

μ : Dynamic viscosity [Pa.s]

2.4.2 Womersley Number (α)

The Womersley number is another primary parameter used in hemodynamic studies. Womersley number describes the unsteady flow characteristics as a response to the unsteady pressure gradients (Loudon & Tordesillas, 1998). It can be defined as the ratio of unsteady forces to viscous forces. The formulation for the Womersley number can be seen below (Yu, 2000).

$$\alpha = \frac{D}{2}\sqrt{\frac{\rho\omega}{\mu}} \tag{2.2}$$

Where:

D: Diameter of the corresponding cross-section [m]

ρ : Density of the fluid [kg/m^3]

ω : Angular frequency [rad/s]

μ : Dynamic viscosity [Pa.s]

The Womersley number also has a strong effect on the velocity profiles. With increasing Womersley numbers, inertial forces become dominant relative to the viscous forces. This characteristic has a visible impact on the velocity profiles. This can be seen in Figure 2.14.

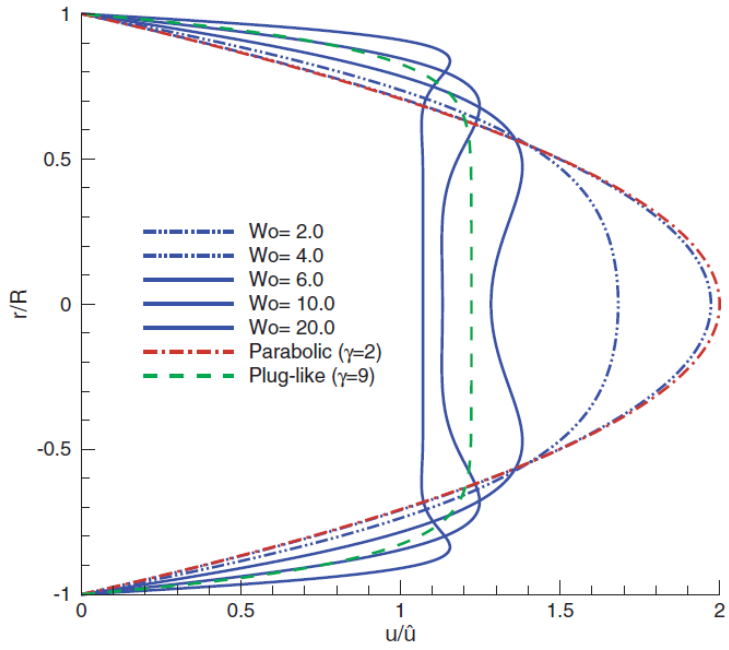

Figure 2.14. Effect of Womersley number on the velocity profile (San & Staples, 2012)

2.4.3 Stokes Number (Stk)

Stokes number is another dimensionless parameter that should be especially considered in the PIV experiments. Stokes number can be defined as the ratio of particle residence time to the characteristic flow time (Israel & Rosner, 1982). It is a measure of how well a particle follows a flow. It is accepted that for Stk >> 1, particles will not follow the flow sufficiently. Stk < 1 provides a sufficient environment for particles to track streamlines sufficiently. Stk < 0.1 decreases the flow tracking errors below %1 (Tropea et al., 2007).

Stokes number can be formulated as the Equation 2.3 (Çengel & Cimbala, 2006).

$$Stk = \frac{\rho_p D_p^2 V}{18\mu L} \tag{2.3}$$

Where:

ρ_p : Particle density [kg/m^3]

D_p : Particle diameter [m]

V : Flow velocity [m/s]

μ : Dynamic viscosity of the fluid [Pa.s]

L : Characteristic length of the flow domain [m]

2.5 Vortex Identification Methods

With the formation of the aneurysms, vortical structures start to be seen in the flow. These vortices reshape the shear stress and flow fields around them. Reshaped flow and shear stress fields inside an aneurysm can modify the forces exerted on the vessel wall. Thus identification of vortices inside an aneurysm is crucial.

First, a vortex description should be made to identify a vortex. Although a standard description everyone agrees on has yet to be made, researchers have made various descriptions of vortices. In 1945 Lamb et al. described the vortex as a tube surrounded by vortex lines. Nitsche et al. (2006) state that a vortex is a fluid rotation around a common centerline. In the book "Vortex Dynamics," Saffman described a vortex as "finite volume of vorticity immersed in irrotational fluid."

Another important subject is to identify a vortex in a flow field. In viscous flows, viscosity makes the boundary between the rotational vortex and the irrotational outer

flow vague (Epps, 2017). Therefore identifying vortices in a viscous flow is more challenging and critical. Jeong and Hussain (1995) reported the requirements for a vortex core. These requirements are:

1. A vortex core should have a net vorticity and, therefore, a net circulation.
2. Identified vortex core's geometry should be independent of the selected inertial reference frame. In other words, it should be Galilean invariant.

To identify a vortex, three intuitive and common methods are suggested. These vortex indicators are:

1. Local Pressure Minimum
2. Pathline and Streamline
3. Vorticity Magnitude

Although these methods can still identify vortices, they can be inadequate in some conditions. This section will discuss the inadequacy of these indicators and alternative methods for vortex identification.

2.5.1 Local Pressure Minimum

Since the pressure in the vortex core tends to reach a local minimum, a local pressure minimum in the pressure field can indicate a vortex core. But a local pressure minimum is not sufficient to identify a vortex core. The existence of sinks or sources can mislead the local pressure minimum indicator. Although these flow structures have a local pressure minimum at the center, these cannot be named vortices since they are irrotational (Jeong & Hussain, 1995).

2.5.2 Pathline and Streamline

It can be thought intuitively that streamlines and pathlines are sufficient to detect any vortices. But there are cases where the pathlines and streamlines can be inadequate

to detect vortices. The first case is where the particles in the flow field fail to complete one full rotation around the vortex core. This may be due to the transition of the vortices resulting from tearing or breakdown (Jeong & Hussain, 1995). In the aneurysm, both tearing and breakdown of the vortices exist; therefore, using streamlines and pathlines to detect vortices in an aneurysm is inaccurate.

Since streamlines and pathlines are not Galilean invariant, they also fail to capture multiple vortices with different core velocities. The problems originating from the streamlines and pathlines not being Galilean invariant can be seen in Figure 2.15.

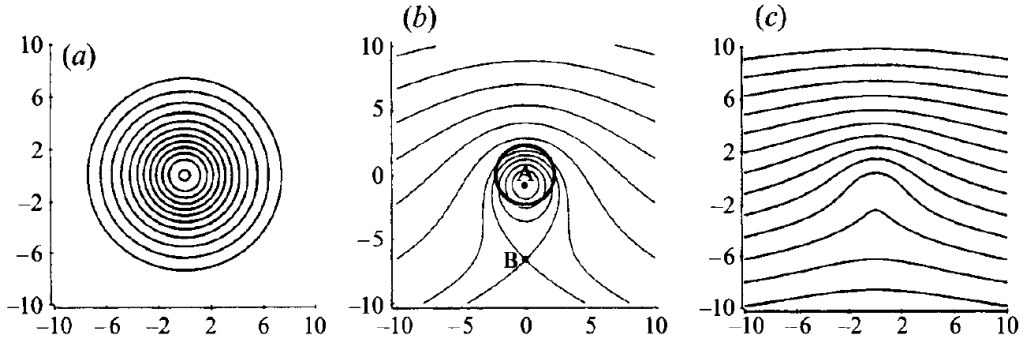

Figure 2.15. Streamlines around a vortex core in three different reference frames moving with (a) the vortex center, (b) a point in the vortex core, and (c) a point faster than any point in the domain (Jeong & Hussain, 1995)

2.5.3 Vorticity Magnitude

The equation for the vorticity vector can be seen in Equation 2.4.

$$\omega = \nabla x \vec{u} \tag{2.4}$$

Where:

ω: Vorticity vector [1/s]

$\vec{u} = (u, v, w)$: Velocity field vector

Vorticity vector in the z direction for a 2D velocity field can also be seen in Equation 2.5.

$$\omega_z = \left(\frac{\partial v}{\partial x} - \frac{\partial u}{\partial y}\right) \tag{2.5}$$

The magnitude of the vector in Equation 2.5 is the vorticity magnitude. Vorticity measures a fluid volume's tendency to rotate around a point. Although all vortex cores should have vorticity, vorticity in a flow field is not a direct indicator of a vortex. The shear layers formed around the walls are examples of this. Velocity gradients in boundary layers can cause vorticity, but this is not related to the rotating motion of the fluid (Jeong and Hussain, 1995). Thus, the usage of vorticity magnitude to identify vortex cores is insufficient.

Due to the inadequacies of these methods, new vortex identification methods are proposed. These methods are:

1. Δ Criterion
2. Swirling Strength (λci) Criterion
3. Q criterion
4. λ_2 Criterion

In this section, details of these methods will be discussed.

2.5.4 Δ Criterion

The derivation for the Δ criterion starts from the first order streamline approximation. A streamline can be approximated in first order as follows;

$$\frac{dx}{dt} = \nabla u \cdot x \tag{2.6}$$

Where X and U are position and velocity vectors in 2D, and the ∇u can be seen in Equation 2.7.

$$\nabla \boldsymbol{u} = \begin{bmatrix} \frac{\partial u}{\partial x} & \frac{\partial u}{\partial y} \\ \frac{\partial v}{\partial x} & \frac{\partial v}{\partial y} \end{bmatrix} \tag{2.7}$$

The characteristic equation of the ∇u can be written as

$$\lambda^2 + P\lambda + R = 0 \tag{2.8}$$

In Equation 2.8, P and R are two invariants of the above ∇u matrix. Where:

$$P = -\frac{\partial u}{\partial x} - \frac{\partial v}{\partial y} \tag{2.9}$$

$$R = \frac{\partial u \partial v}{\partial x \partial y} - \frac{\partial u \partial v}{\partial y \partial x} \tag{2.10}$$

The discriminant of the characteristic equation is

$$\Delta = P^2 - 4R \tag{2.11}$$

If the characteristic equation's discriminant is negative, the velocity gradient matrix has two complex conjugate eigenvalues. These two eigenvalues and eigenvectors are given in Equations 2.12 & 2.13 respectively.

$$\lambda_{cr} \pm \lambda_{ci} i \tag{2.12}$$

$$\nu_{cr} \pm \nu_{ci} i \tag{2.13}$$

Velocity gradient tensor can be decomposed to its eigenvalues and eigenvectors as

$$\nabla \boldsymbol{u} = [\nu_{cr} \ \nu_{ci}] \begin{bmatrix} \lambda_{cr} & \lambda_{ci} \\ -\lambda_{ci} & \lambda_{cr} \end{bmatrix} [\nu_{cr} \ \nu_{ci}]^{-1} \tag{2.14}$$

Substituting this equation to Equation 2.6 and changing global (x,y) variables to the local (ξ,η) variables results in

$$\frac{d\xi}{dt} = \begin{bmatrix} \lambda_{cr} & \lambda_{ci} \\ -\lambda_{ci} & \lambda_{cr} \end{bmatrix} \cdot \xi \tag{2.15}$$

Integrating this equation to solve for ξ, η results in

$$\xi = e^{\lambda_{cr}t}[C_1 \cos(\lambda_{ci}t) + C_2 \sin(\lambda_{ci}t)] \quad (2.16)$$

$$\eta = e^{\lambda_{cr}t}[C_1 \cos(\lambda_{ci}t) - C_2 \sin(\lambda_{ci}t)] \quad (2.17)$$

From Equations 2.16 & 2.17 it can be seen that, if the discriminant of the characteristic equation is negative, streamlines are taking a circular shape around a point which is the indicator of a vortex. The main idea behind the Δ Criterion is, having a negative Δ indicates a swirling motion, therefore, a vortex (Chen et al., 2015).

2.5.5 λ_{ci} Criterion

λ_{ci} criterion is the direct result of the Δ criterion. Having a positive λ_{ci} means having the imaginary part of the eigenvalue. The imaginary part of the eigenvalue results from the negative discriminant, again an indicator of the vortex in a flow field (Chen et al., 2015).

2.5.6 Q Criterion

Q is the second invariant of the velocity gradient tensor in 3D for incompressible flows. Second invariant Q is given in Equation 2.18

$$Q = \frac{1}{2}(\|\Omega\|^2 - \|S\|^2) \quad (2.18)$$

Where Ω is the rate of rotation tensor ,and S is the rate of strain tensor. Ω represents pure rotational motion, and S represents pure irrotational motion. In open form Q can be written in 2D as

$$Q = \frac{du}{dx}\frac{dv}{dy} - \frac{du}{dy}\frac{dv}{dx} - \frac{1}{2}\left(\frac{du}{dx} + \frac{dv}{dy}\right)^2 \qquad (2.19)$$

Positive Q means, excess rotational motion relative to the irrotational strain tensor. Therefore second invariant of the 3D velocity gradient tensor is another vortex indicator.

2.5.7 λ_2 Criterion

Although the pressure minimum is not a direct indicator of a vortex, it can still help detect vortices in a flow field. There are two reasons why a pressure minimum is not always an indicator of a vortex (Jeong and Hussain, 1995).

1) The first reason is unsteady straining in a flow field. Due to unsteady straining, local pressure minimums can be formed inside a flow field, but these pressure minimums do not involve any rotational motion (Jeong and Hussain, 1995).

2) Second reason is the viscous effects in a flow field. Viscous effects can act like a damper to eliminate the pressure minimums created by the vortices (Jeong and Hussain, 1995).

In 1995 Jeong and Hussain proposed a new vortex identification method that utilizes the pressure minimum and neglects the unsteady and viscous effects. Since these effects are ignored, the pressure minimums in the flow field are purely related to vortex cores. They used pressure Hessian to develop the method. Pressure Hessian is strongly dependent on pressure minimums in a flow field since it includes the spatial derivatives of the pressure

Derivation of the λ_2 criterion starts with the gradient of the Navier-Stokes for 2D incompressible flows. Then, the gradient of the Navier-Stokes is decomposed into its symmetric and antisymmetric parts. The antisymmetric part is subtracted from the Navier-Stokes and the below equation is left.

$$\frac{dS}{dt} + \upsilon\nabla^2 S + S^2 + \Omega^2 = -\frac{1}{\rho}\nabla(\nabla p) \tag{2.20}$$

Where υ is the kinematic viscosity. After the unsteady straining and viscous effects are neglected, the simplified equation becomes

$$S^2 + \Omega^2 = -\frac{1}{\rho}\nabla(\nabla p) \tag{2.21}$$

Where the right-hand side of the equation is the pressure Hessian. Since the pressure Hessian is a symmetric matrix, its eigenvalues are real. Jeong et al. defined the vortex core as a "connected region with two negative eigenvalues". Therefore, $S^2 + \Omega^2$ should have two negative eigenvalues. Ordering the two eigenvalues of the $S^2 + \Omega^2$ as $\lambda_1 < \lambda_2$ for the 2D planar flow, λ_2 should be negative to have a vortex core (Chen et al., 2015).

2.6 Comparison of the Vortex Identification Criteria

In this section, all four vortex identification methods (Δ, λ_{ci}, Q, λ_2) will be compared. Theoretically, these four methods should yield the same result for 2D incompressible flows since they substantially satisfy the same equation (Chen et al., 2015). This equation is the following

$$\frac{\partial u}{\partial y}\frac{\partial v}{\partial x} < 0 \tag{2.22}$$

But in the application these methods differ and capture different numbers of vortices. Chen et al. (2015) used a PIV dataset taken from a planar flow to compare the differences between these methods in the application. Captured vortices for each identification method can be seen in Figure 2.16.

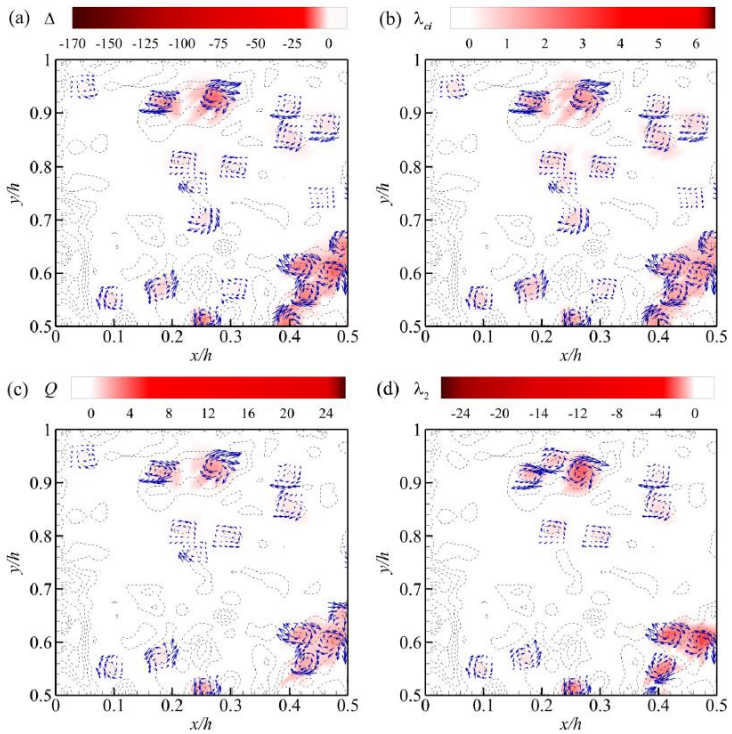

Figure 2.16. Vortices captured by (a) Δ Criterion, (b) λ_{ci} Criterion, (c) Q Criterion, (d) λ_2 Criterion (Chen et al., 2015).

2.7 Wall Shear Stress (WSS)

Due to sudden expansion in the aneurysms, blood flow fails to follow the vessel wall. This causes separation near the proximal end and reattachment of the flow near the distal end of the aneurysm. Flow separation starts to be seen even in the early stages of the aneurysm (Salsac et al., 2006). These changed hemodynamics also modifies the shear stress values on the aneurysm wall. According to Bluestein et al. (1996), wall shear stress values at an aneurysm's reattachment zone is nearly twice that of a healthy aorta. Also, the same study reported that wall shear stress values in the recirculation zone of an aneurysm is one order of magnitude less compared to a healthy aorta. Salsac et al. (2006) also reported that AAAs have regions that have much larger and lower WSS magnitudes relative to a healthy vessel. Additionally, AAAs have large WSS gradients that are not seen in healthy aortas.

These abnormalities in the WSS values on aneurysm walls made the research about it inevitable. Although the role of WSS in the formation and evolution of an aneurysm is still unknown, research on this topic is still ongoing. To better understand WSS's effect on the aneurysm wall, WSS parameters are developed. Three of these parameters are named as

1) Time Averaged Wall Shear Stress (TAWSS)

2) Oscillatory Shear Index (OSI)

3) Endothelial Cell Activation Potential (Diachille et al., 2014)

2.7.1 TAWSS

TAWSS is the measure of average shear stress magnitude applied on an aneurysm wall in a cardiac cycle (Diachille et al., 2014). It is calculated using the Equation 2.23.

$$TAWSS = \frac{1}{T}\int_0^T |\tau_w|\, dt \tag{2.23}$$

Where T is the duration of a cardiac cycle and $|\tau_w|$ is the magnitude of the shear stress exerted on the aneurysm wall.

2.7.2 OSI

OSI is the measure of shear stress oscillation inside an aneurysm. It takes the value of 0.5 for pure oscillatory flows, which change direction constantly. OSI is 0 for a unidirectional flow that does not change direction and is free of oscillations. OSI calculated using the Equation 2.24

$$OSI = \frac{1}{2}\left(1 - \frac{\left|\int_0^T \tau_w dt\right|}{\int_0^T |\tau_w|\, dt}\right) \tag{2.23}$$

2.7.3 ECAP

ECAP is one of the most recent parameters that was proposed by Di Achille et al. (2014). It is a metric representing the vessel wall's susceptibility to the blood cells. It is known that intraluminal thrombus (ILT) formation is commonly seen in AAAs. One theory about ILT is that it is the body's natural response to strengthen the weakened vessel wall (Bluestein et al., 1996). Although the mechanism is unclear, it

is known that ILT formation plays an active role in the formation and evolution of AAAs. Therefore calculating a metric that is related to this phenomenon may be critical. ECAP is calculated using the Equation 2.24

$$ECAP = \frac{OSI}{TAWSS} \tag{2.24}$$

From Equation 2.24, it can be seen that higher oscillatory behavior and low average shear stress magnitude on a vessel wall make it more susceptible to blood cell deposition. In one of the early studies, Levesque et al. (1986) related this phenomenon to the shape of endothelial cells. According to their studies on the animals, endothelial cells are more rounded in the areas with low or oscillatory shear stress, which are generally seen in disturbed flow areas. This causes larger surface areas and more permeability for the endothelial cells that can trigger the ILT formation on the vessel wall (Levesque et al., 1986).

2.8 WSS Measurements in Experimental Studies

Obtaining the WSS field in an aneurysm experimentally may be challenging in various ways. Some of these challenges are related to measurement techniques, blood-mimicking fluid, and accurately determining the wall location.

In 1995 Oshinski et al. conducted a study utilizing the MR phase velocity mapping technique to calculate the WSS inside the abdominal aorta. They assumed a linear velocity profile near the aneurysm wall and calculated the shear stress using this profile. The challenging part of this study was to estimate the wall location accurately. To estimate the wall location, the flow rate which passes through the boundary pixel was assumed to be correct. Using this flow rate and linear velocity profile, they estimated the wall location and calculated the shear stress accordingly

(Oshinski et al., 1995). Figure 2.17 explains the method used to calculate the WSS values.

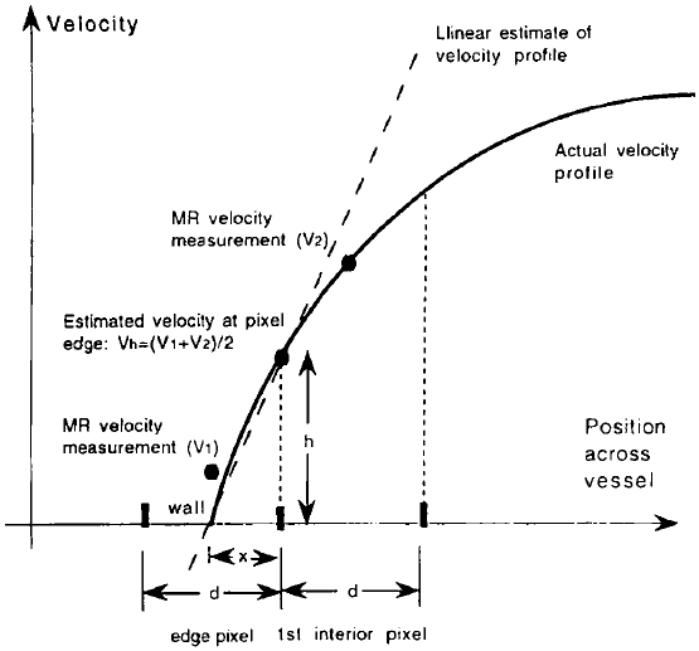

Figure 2.17. Wall location estimation with the MR phase velocity mapping technique (Oshinski et al., 1995)

Another experimental study about determining the WSS experimentally was conducted by Petersson et al. (2012). They used PC-MRI to measure the velocity field. These measurements were then used to calculate the WSS and compared with numerical results to determine the accuracy. Three WSS estimation methods were tested for this study. The first method, Vel-LE, utilizes two measured velocities and linear extrapolation. The slope of the extrapolated line is used to calculate the WSS. The second method was named as Vel-Wall. This method uses one velocity value interpolated from two measured velocities and the wall location. It assumes zero velocity on the wall and calculates the WSS utilizing the slope of the line between the interpolated velocity value and the zero velocity on the wall. The third method, Vel-Parabolic, utilizes three measured velocity values and the wall location. A

parabolic velocity profile is fitted to three measured velocity values, and this profile's slope near the wall is used to calculate WSS (Petersson et al., 2012).

Petersson et al. (2012) reported that all of these three methods underestimated the WSS values. It was observed that only the low WSS values were overestimated when the Vel-Parabolic method was used. Researchers also indicated that the primary factor that decreased the accuracy of these estimates was limited spatial resolution. Additionally, the wall location estimation was another problematic factor that reduced the accuracy since the wall location could not be estimated precisely, leading to additional errors in the WSS calculations (Petersson et al., 2012).

PIV is one of the most common measurement techniques used in aneurysm studies. Therefore WSS calculations using PIV should also be discussed. In 2003, Hachareon studied the WSS field inside a heart chamber using PIV. This study reported the main problems and considerations associated with using PIV to calculate WSS. The first problem is the light reflected by the boundary between the BMF and the model wall. This light reflection can be misinterpreted as the stationary particles in the processing stage and can introduce a bias of zero velocity near the wall. In solving this problem, correct laser energy and achieving a near-perfect refractive index match between the BMF and the model geometry play important roles. Another variable that should be considered is the size of the interrogation area. The spatial resolution can significantly decrease if the interrogation area is too large. Although too large an interrogation area may lower the spatial resolution, reducing the size of the interrogation area too much can also pose problems. Particles in the small interrogation areas can escape and can lead to a bias towards low velocity gradients as high-velocity particles are neglected. Thus using an interrogation area with the right size is essential for accurate WSS calculations. Another factor that should be considered is the interrogation areas with low fluid volume adjacent to the boundaries. The accuracy of the cross-correlation results of these boundary interrogation areas can be problematic (Hochareon, 2003).

2.9 Previous AAA Studies

A summary of the experimental investigations on the AAA will be made in this section.

The first study that will be discussed was performed by Yu et al. (2000). Detailed research about the vortical structures and their mechanisms in two simple aneurysm geometry was conducted. Varying Reynolds and Womersley numbers for steady and pulsatile flows are tested. A baseline model, which is a simple healthy aorta model, was also used to compare flow fields with the aneurysm models. An experimental setup consisting of a submersible pump, a flow straightener, and a small piston-cylinder driven by a DC motor to provide sinusoidal pulsating flow to the setup was used in this study. 2D-PIV was utilized to measure the velocity field inside the aneurysm. Water-glycerin mixture with a viscosity of 3.5 cP and density of 1.121 g/cm3 was used as the blood-mimicking fluid (Yu, 2000).

Yu (2000) described the flow field in an aneurysm as a jet flow surrounded by a weak recirculation region for the steady flow case. Adverse pressure gradient due to the flow field expansion was shown as the reason behind the recirculation region. Another key observation was the location of the vortex cores in these recirculation regions. These vortex cores were not located in the middle, but instead, they were located closer to the distal end of the aneurysm.

In the second experimental case, a sinusoidal pattern was used to simulate the physiological flow seen in the human body. Flow patterns for the two different Womersley numbers can be seen in Figure 2.18. Different sinusoidal waveform phases in the baseline model (healthy aorta) resulted in boundary layer thickness changes. While the acceleration of the flow decreased the boundary layer thickness, deceleration after the peak was accompanied by the thickening of the boundary layer. Flow was attached to the baseline model's walls in every phase of the physiological flow pattern.

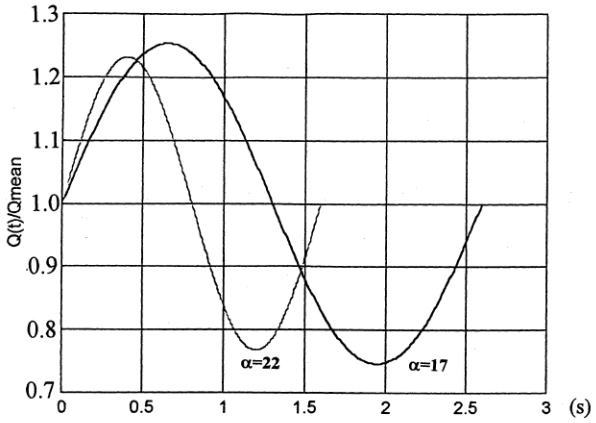

Figure 2.18. Two flow patterns used by Yu (2000)

With the pulsatile flow, interesting vortex mechanisms were observed in aneurysm models. At the acceleration phase for α= 22, while passing through nearly the average flow rate point, a weak vortex was observed at the proximal end of the aneurysm. This trend can be seen in Figure 2.19.

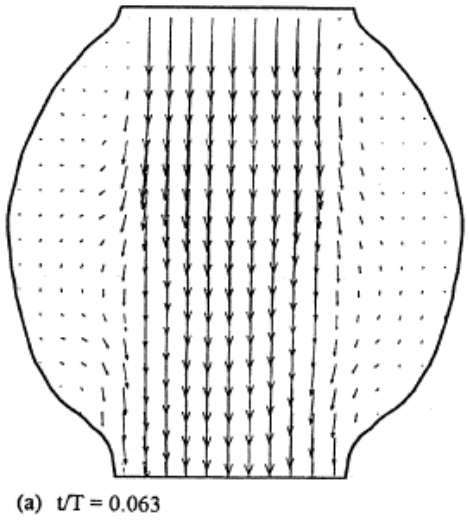

Figure 2.19. Flow field observed in the acceleration phase for α =22 (Yu, 2000)

After the flow rate peaked, the vortex's strength increased significantly at the start of the deceleration phase. Besides getting stronger, the vortex core also migrated toward the center of the aneurysm. (Figure 2.20)

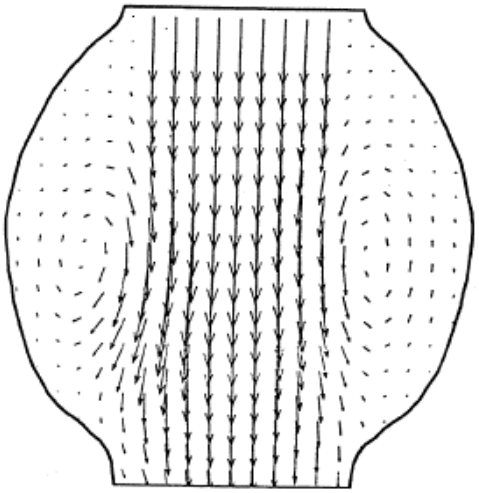

Figure 2.20. Flow field observed in the peak flow rate

As the deceleration phase continued, the vortex kept migrating toward the distal end. The vortex strength peaked at the deceleration phase while passing through the average flow rate. Significant decay in the vortex strength was observed when the flow rate reached its local minimum (Figure 2.21). If the strength of the vortices in each phase were compared, vortex strength in the minimum flow rate state was significantly higher than the peak flow rate condition.

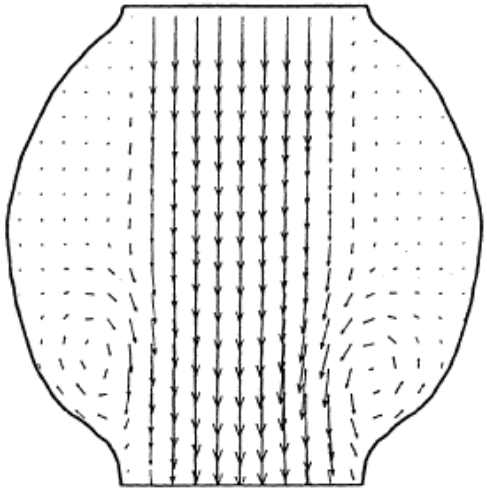

Figure 2.21. Flow field observed at the minimum flow rate

Yu (2000) also investigated the effect of aneurysm sizes on the strength of the vortices. It was reported that the vortices' strength was nearly 20 % weaker for smaller aneurysms. Also, they explained the reason behind the vortical formations as the rapid acceleration and decelerations in the pulsatile flow pattern.

The change in the strength of the vortex core in its travel along the aneurysm was also explained by Yu. They proposed "vortex stretching" to explain this mechanism. As the vortex migrates toward the center of the aneurysm, the cross-sectional area increases, and the vortex tube formed inside the aneurysm stretches. As a result of this stretching, the diameter of the vortex tube decreases, and the vorticity increases to conserve the angular momentum. The opposite of this phenomenon is observed after the vortex passes through the midpoint of the aneurysm. When the cross-sectional area decreases, the vortex tube is compressed, and the vorticity decreases accordingly. This mechanism is explained in Figure 2.22

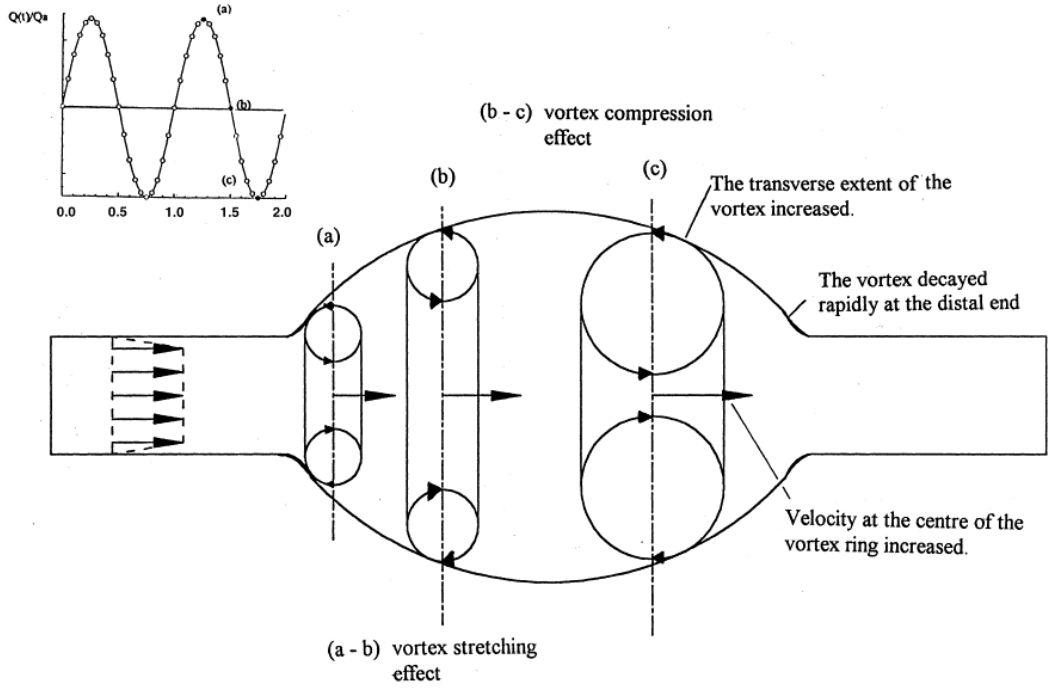

Figure 2.22. Proposed mechanism to explain vortex strength changes in a cardiac cycle (Yu, 2000)

In 2019, Bauer et al. experimentally investigated the WSS field in a simple AAA geometry. They compared the WSS results obtained by magnetic resonance velocimetry (MRV) and laser Doppler velocimetry (LDV) with the numerical results and reported the accuracy of the experimental techniques. A simple elliptic geometry with the water as the working fluid was used in this experimental study. As discussed in the previous chapters, two factors that make the experimental WSS investigation challenging are estimating the wall location and measuring the relatively small velocities near the wall.

To estimate the wall location using LDV, Bauer et al. (2019) used two velocity measurements near the wall and a linear velocity fit. With the no-slip boundary condition assumption, the wall location was estimated to be where the linear velocity profile reached 0.

The results of the steady flow experiments were also compared to a previous study conducted by Budwig et al. (1993). The results of this study can be seen in Figure 2.23.

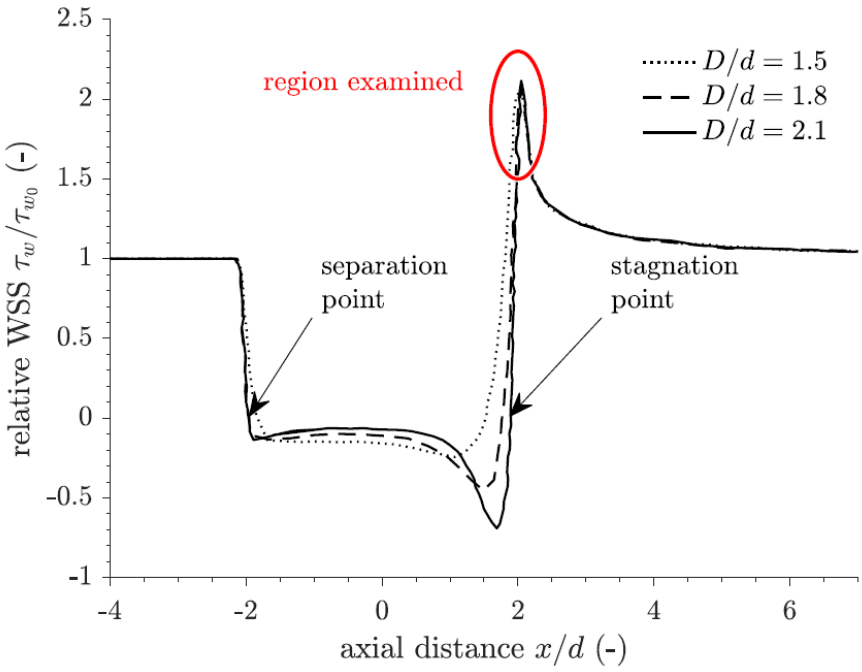

Figure 2.23. Normalized WSS results for a steady flow in a simple aneurysm geometry obtained by Budwig et al. (1993).

The steep decrease in WSS is related to flow separation caused by the expansion of the proximal end of the aneurysm. Near zero WSS values present inside the aneurysm region are sourced by the low velocities and gradients in the recirculation region. The following WSS peak is related to the reattachment of the flow near the distal end.

The velocity profile near the wall was assumed to be linear for the laminar flow case. A linear velocity profile was fitted to the measurement points with intervals of 50 μm in the wall-normal direction. The slope of this linear profile was the velocity gradient and was used to calculate the WSS. This velocity profile fitting process can be seen in Figure 2.24.

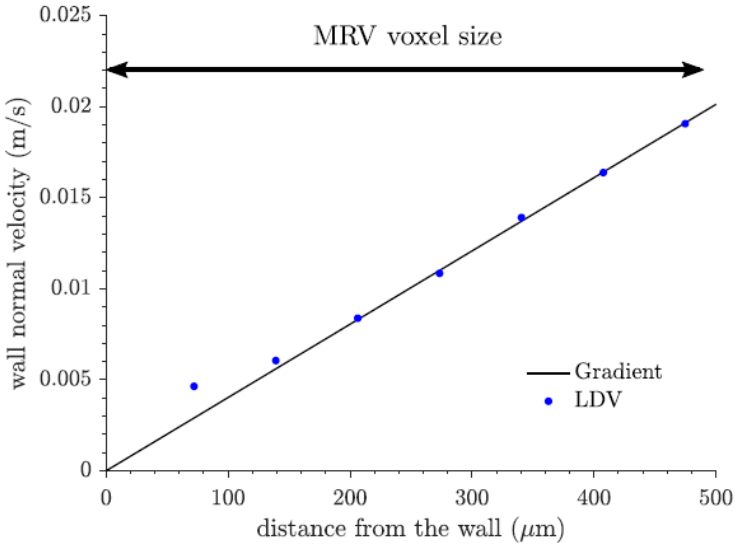

Figure 2.24.Velocity profile fitting process to near-wall discrete LDV data (Bauer et al. 2019).

A comparison of the MRV and LDV to the Budwig et al. (1993) can be seen in Figure 2.25.

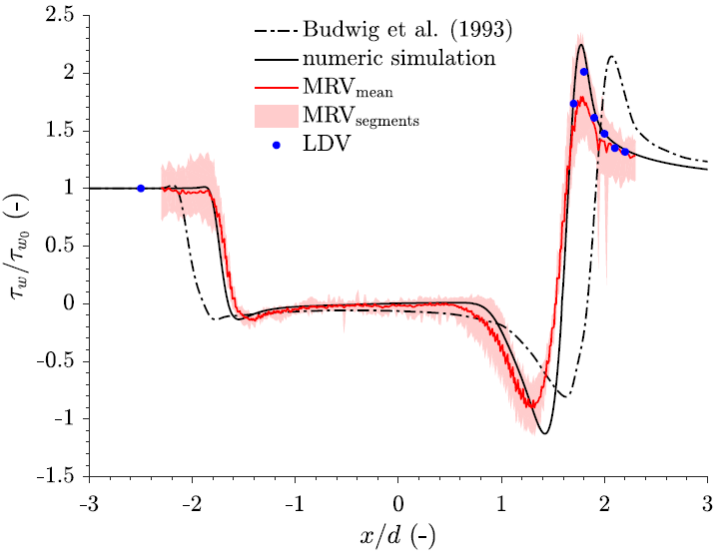

Figure 2.25. Comparison of the WSS results obtained using LDV and MRV with the previous studies (Bauer et al. 2019).

Determining the appropriate velocity profile near the wall was more challenging for the turbulent flow case. Although the grid size for the LDV is halved to 25 μm to capture the high velocity gradients, obtaining WSS with high accuracy was still more complicated than laminar flow. Four methods were proposed to estimate the turbulent case's velocity profile near the wall. The first method was visually inspecting the velocity measurements near the wall and estimating the velocity gradient manually. The second and third methods utilized the non-dimensional parameters u+ and y+ to fit a velocity profile near the wall. The second method feeds the measured velocity data to the velocity profile proposed by Musker et al. (1979). This velocity profile is given in Equation 2.25.

$$\frac{du^+}{dy^+} = \frac{\frac{(y^+)^2}{\kappa} + \frac{1}{s}}{(y^+)^3 + \frac{(y^+)^2}{(y^+)^2} + \frac{1}{s}} \tag{2.25}$$

Where κ = 0.41 and s = 0.001093

A velocity profile developed from a Direct Numerical Simulation (DNS) study conducted by Khoury et al. (2013) was used as the third method. This DNS study was conducted at the pipe flow at Re = 5300.

The fourth and last method was feeding the measurement data to a velocity profile developed by Durst et al. (1996). This velocity profile can be seen in Equation 2.26.

$$u = \frac{u_\tau^2}{v}(y - y_0) + C_2(y - y_0)^2 + C_4(y - y_0)^4 + C_5(y - y_0)^5 \tag{2.26}$$

C_2, C_4, C_5, u_τ and y_0 are the free fitting parameters. Aside from the previous methods, this method is only applicable in the viscous sublayer of $y^+ < 12$.

Although estimating the wall location and using a proper velocity profile pose a significant challenge, Bauer et al. concluded that experimental WSS calculations, especially LDV, can provide accurate WSS results.

Whether using a Newtonian or non-Newtonian BMF in the aneurysm studies is still being discussed in the literature. Despite it is known that blood is a shear-thinning fluid, due to the large diameter of the abdominal aorta, low shear zones are limited to small regions (Hoskins & Hardman, 2017). To examine the differences between the non-Newtonian and Newtonian BMFs, Deplano et al. (2014) conducted a study.

To prepare the non-Newtonian BMF, blood with standard hematocrit (45%) at 37 °C was taken as a reference. 350 ppm of Xanthan Gum and 0.9 g/L of sodium salt were added to an aqueous solution, including 20 % of glycerin by weight. Newtonian BMF was prepared using a 40 % aqueous glycerin solution by volume. 0.9 g/L sodium salt was added to this solution since flow meters in the experimental setup are electromagnetic and require salt to function properly. These BMFs should reflect the human blood's physical characteristics and have a suitable refractive index to work with PIV. The Newtonian BMF had a dynamic viscosity of 4.039 cP and a density of 1099 kg/m3. The dynamic viscosity characteristic of the non-Newtonian BMF can be seen in Figure 2.26.

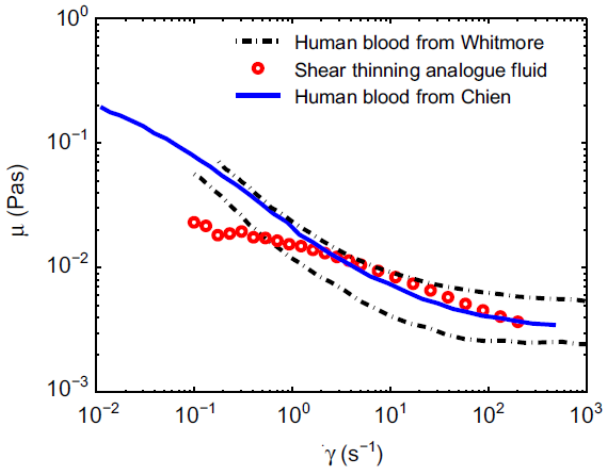

Figure 2.26. Viscosity characteristic comparison of the prepared BMF with the previous studies in the literature (Deplano et al., 2014).

A simple AAA model, which also includes iliac arteries, was examined in this study. Physiological flow pattern was provided for the aneurysm model.

After examining vortical structures inside the aneurysm for both BMFs, there was a significant difference between the vortex propagation velocities. Although the vortices left the proximal neck at a similar instant, it was observed that the vortical structures propagated faster inside the Newtonian BMF. Even if the vortical structures migrated and impacted the distal wall of the aneurysm in the Newtonian BMF, this was not the case for shear-thinning BMF. Vortices decayed before reaching the distal wall in the non-Newtonian BMF. The propagation of vortices in both of the BMFs is presented in Figure 2.27.

Circulation strength was another topic that Deplano et al. (2014) investigated. As a result, it was observed that the vortex circulation strength was much larger for the Newtonian fluid. For the anterior and posterior sides, the circulation strength was 1.89 and 5.44 times higher in the Newtonian BMF.

The study of the Deplano et al. concluded that, although the abdominal aorta is a large artery, the shear thinning characteristic of the blood has notable effects on the flow field.

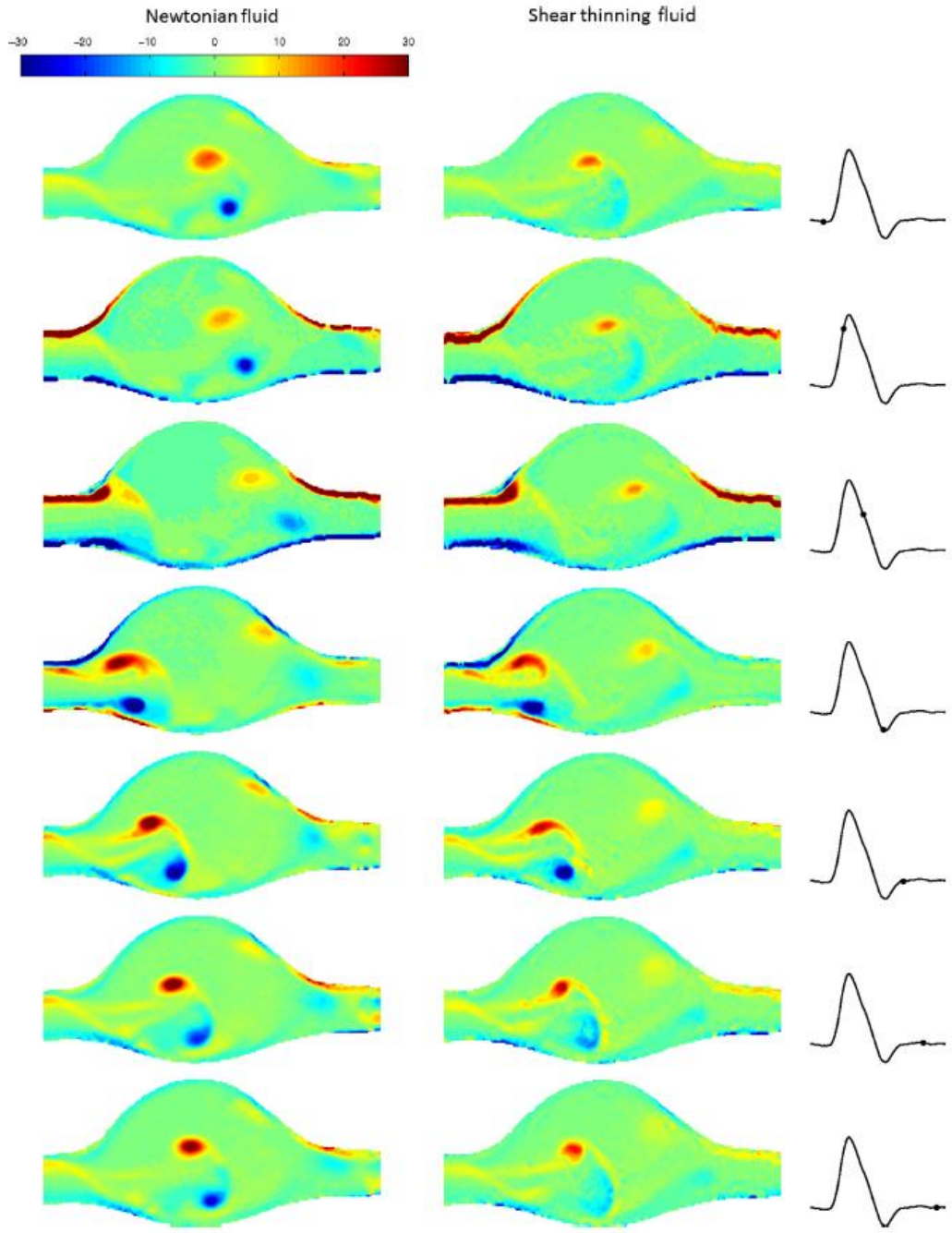

Figure 2.27. Comparison of the vortex propagation characteristics in the Newtonian and shear-thinning fluids (Deplano et al. 2014).

CHAPTER 3

EXPERIMENTAL SETUP

Experiments for this study are carried out in the Fluid Mechanics Laboratory of the Mechanical Engineering Department at Middle East Technical University. This section describes the details of the experimental setup used in this study.

3.1 Flow Circulatory Setup

The flow circulatory setup used in this experiment is a closed-loop system through which the blood mimicking fluid flows. A positive displacement gear pump (Dayton 4KHH8, Grainger, Inc., Lake Forest, IL) driven by a computer-controlled servo motor is placed after the BMF storage tank to supply the necessary flow pattern to the experimental setup. With the computer-controlled servo motor, physiological flow pattern can be provided for the experimental setup. The shaft of the computer-controlled servo motor is connected to the gear pump shaft with a coupling. BMF is stored in an acrylic tank covered with film heaters to keep the fluid at nearly 23°C. BMF is provided from the tank to the aneurysm phantom through stiff and transparent pipes. The stiffness of the pipes is crucial to preserve the flow pressure through the piping. Also, the transparency of the pipes make it possible to see any air bubbles that are present in the system. The experimental setup has three on/off valves and an adjustable valve. With an adjustable valve, it is possible to control the pressure and flow rate inside the setup. In the phase of selecting components, attention was paid to the materials of these components to prevent any possible chemical reactions with the BMF. Image and schematic of the experimental setup can be seen in Figures 3.1 and 3.2 respectively.

Figure 3.1. Image of the experimental setup in Fluid Mechanics Laboratory

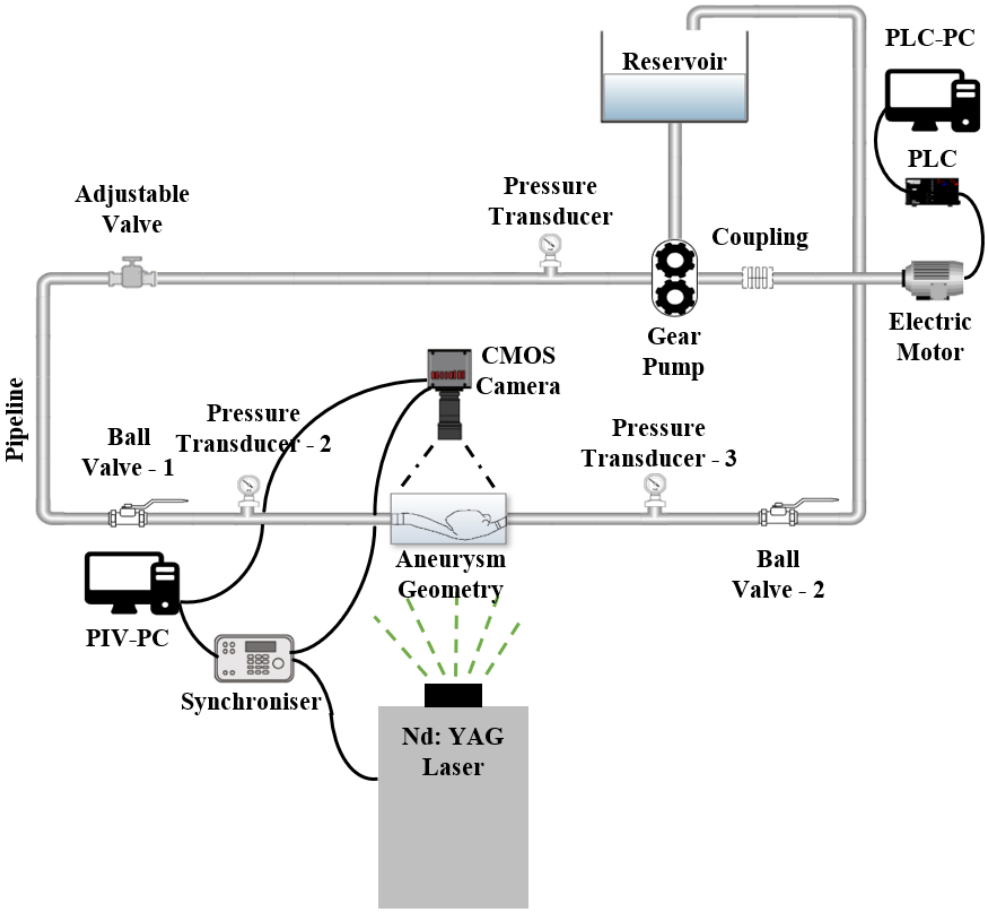

Figure 3.2. Schematic diagram of the experimental setup

3.1.1 Abdominal Aorta Phantoms

Two abdominal aorta phantoms are used in this study. Both phantoms are patient-specific and obtained by the CT scan of two humans. One of these phantoms is a normal aorta taken from a healthy human and the other from an aneurysm patient. These phantoms and dimensions can be seen in Figures 3.3, 3.4, 3.5 & 3.6.

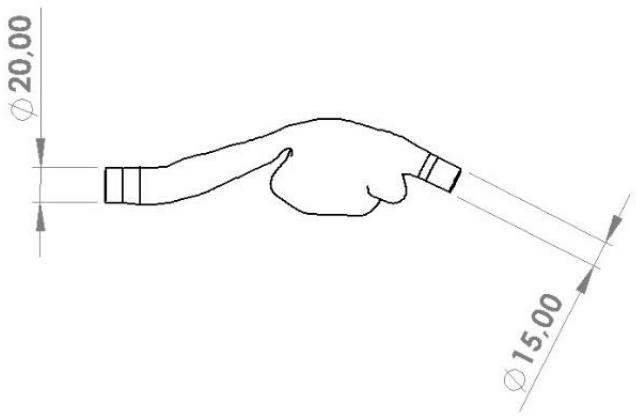

Figure 3.3. Dimensions of the patient specific aneurysm (in mm)

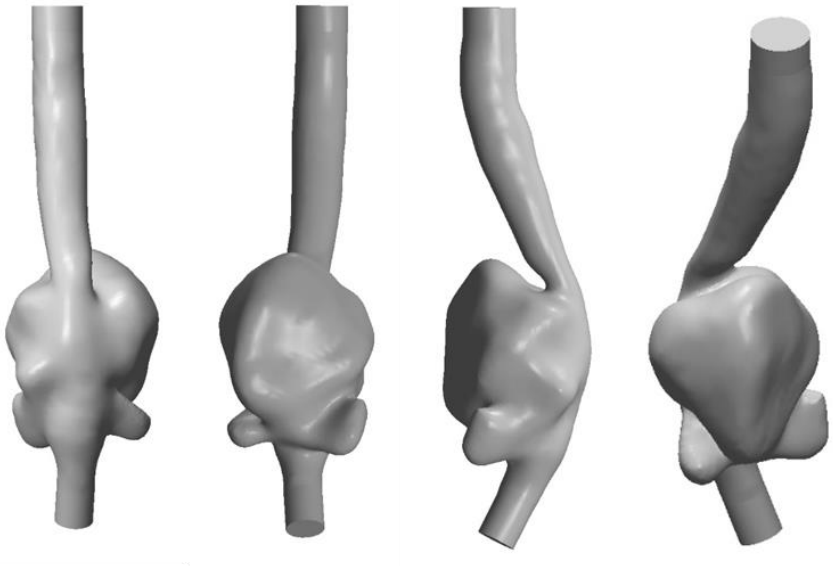

Figure 3.4. Different views of the patient specific aneurysm

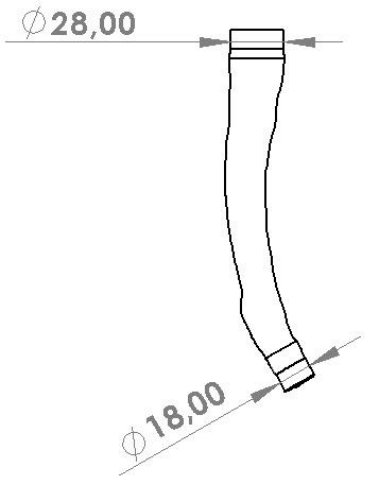

Figure 3.5. Dimensions of the healthy aorta (in mm)

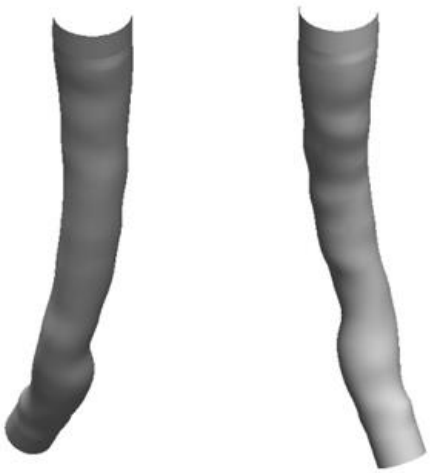

Figure 3.6. Different views of the healthy aorta

Polydimethylsiloxane (PDMS) Sylgard 184 is used to produce these phantoms. Both phantoms are produced with casting. Lost-core technique with a male mold is used for casting. The main advantages of using PDMS are refractive index (RI) match with the BMF and rigidness of the material. The refractive index of the PDMS is 1.4118, and it provides near perfect RI match with the BMF. Since PIV, an optical measurement technique, is used in this study, RI match plays a crucial role in the

accuracy of the obtained velocity field. Also, PDMS shows a rigid character when the wall thickness is minimum of 12 mm (Geoghegan et al. 2012). The rigidness of the PDMS is vital for the WSS calculations with PIV. Determining the wall location of the phantom precisely is necessary for the accuracy of the WSS calculations. Having an expanding phantom and moving walls can cause the underestimation or overestimation of the calculated velocity gradients. Therefore, having a rigid phantom model and stationary phantom walls are another factor that increases the accuracy of the WSS calculation.

3.1.2 Blood Mimicking Fluid

Two main criteria need to be considered when selecting blood mimicking fluid. The first criterion is that it should reflect blood's physical characteristics, like viscosity and density. The second criterion is having a near-perfect reflective index match with PDMS Sylgard 184 since an optical measurement technique, PIV, is used to obtain the velocity field. Another criterion arose during previous studies carried out at the same laboratory. It is having a non-reactive blood mimicking fluid. Salt-based blood mimicking fluids react with the iron flow circulatory components and cause colorization of the fluid. This colorization affects the optical characteristics of the blood mimicking fluid and considerably lowers the PIV measurements' accuracy. Therefore using another mixture that does not contain salt was necessary. For that reason, the mixture that is proposed by Brindise et al. (2018) is used in this study. This is a mixture composed of water, glycerol, and urea that shows Newtonian characteristics. The properties of this mixture and the comparison with the blood and PDMS can be seen from Table 3.1. Also, the perfect refractive index match between the blood mimicking fluid and PDMS can be seen in Figure 3.7.

Table 3.1. Material property comparisons of BMF with the blood and PDMS

Material	*Wt% Water*	*Wt% Glycerol*	*Wt% Urea*	*Refractive Index*	*Viscosity (Pa.s x 10^{-3})*	*Density (kg/m^3)*
BMF	44.07	34.52	21.41	1.4124	4.184	1114
Blood	-	-	-	-	3.8 - 3.5	1060
PDMS	-	-	-	1.4118	-	-

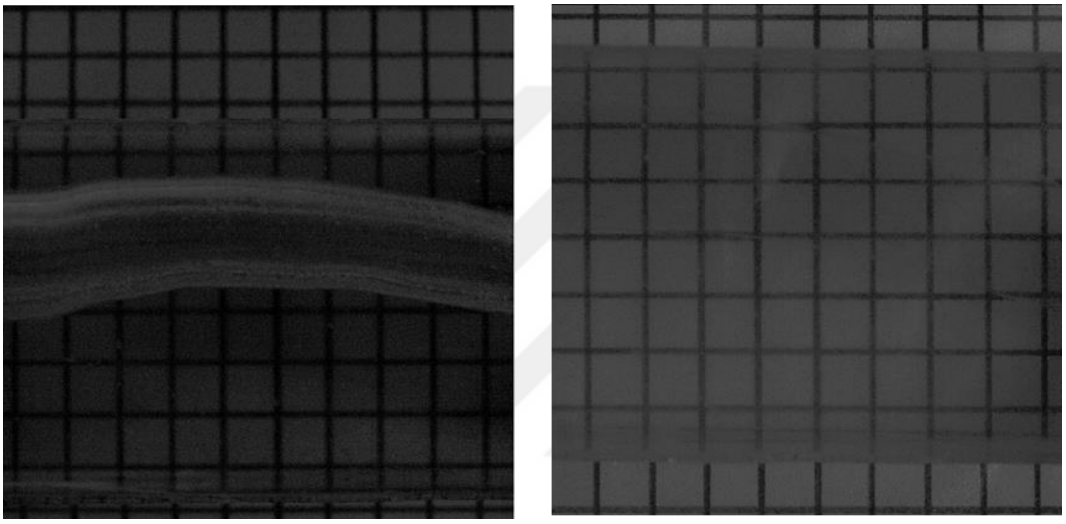

Figure 3.7. Normal aorta model filled with air (Left), normal aorta model filled with blood mimicking fluid (Right)

Distortion of the lines due to poor refractive index between air and PDMS is visible on the left image. Undistorted, straight grid lines indicate a perfect refractive index match between the PDMS and blood mimicking fluid.

From Ferreira et al. (2017), it can be seen that the viscosity of glycerol has a strong temperature dependence. Therefore, to increase the experiments' accuracy and repeatability, the blood-mimicking fluid's temperature is checked frequently and kept at 23±1°C.

3.1.3 Particle Image Velocimetry (PIV)

Particle Image Velocimetry (PIV) is used in this study to obtain the velocity field inside the aneurysm. PIV is a non-intrusive, optical measurement technique that can provide a 2D or 3D velocity field depending on the number of cameras in the PIV setup. In this study, 2D velocity field is obtained using a single camera.

The main principle behind the PIV measurement technique is taking successive images of the flow domain and tracing the seeding particles between these consecutive images. Flow domain is illuminated using a laser sheet to trace these particles, and a high-speed camera captures the light scattered by these seeding particles.

The flow domain is divided into regions called interrogation areas to process the images. Then the software traces seeding particles inside these interrogation areas between two consecutive images. Two consecutive images are called image pairs. Since the seeding particles are identical, identifying them in each image is problematic. To solve this problem, PIV uses an algorithm called cross-correlation. PIV software transforms the images into a function of light intensity. The light intensity function for every possible location of a seeding particle in the second image is cross-correlated with the initial image. Then, cross-correlation results are compared, and the largest cross-correlation result is said to be the most probable location for that particle. The velocity vector is calculated considering the time difference and displacement of particles between the image pairs. Then these vectors in the interrogation area are averaged. PIV assumes all particles in that interrogation area are displaced according to this averaged vector (Hochareon, 2003). Therefore a uniform velocity vector exists in the centroid of each interrogation area.

TSI PIV hardware is employed in this experimental setup. The data obtained by the hardware is processed with Insight 4G, which is another TSI product. To illuminate the flow domain 15 Hz, double pulsed Q-switched Litron Nano L200-15 200 MJ Nd: YAG type laser is used. The wavelength of this laser is 532 nm. A spherical and

cylindrical lens transforms the laser beam into a planar sheet. Focal point of the spherical lens is 1000 mm, and the radius of the cylindrical lens is 5 mm. The camera used to capture images is a 4 MP Nikon CMOS (Complementary Metal Oxide Semiconductor) with a Nikon Nikkor 50 mm f1.8 lens. To synchronize the laser pulse and the camera shutter, Laser Pulse TM 610036 model synchronizer is used. Dantec Dynamics Silver Coated Hollow Glass Spheres are used as the seeding particles. The diameter of these particles is 10 microns, and the density is 1400 kg/m3. These parameters must be selected to ensure the particles are buoyant and completely follow the flow. Stokes number is a dimensionless parameter used to describe a particle's behavior inside a flow. It is accepted that for the tracers that have a Stokes number smaller than 0.1, particles trace the flow with less than 1% error (Tropea et al. 2007).

3.1.3.1 PIV Parameters

In this study, data is taken from 12 points in one physiological cycle for both geometries. These points and the flow patterns for both geometries can be seen in Figure 3.8. To capture images at the desired instances, a voltage output is created at the pump software and sent to the PIV system. This signal triggers the PIV system, and the image is captured from the domain illuminated by the synchronized laser sheet. In this stage, phase-averaging method should also be mentioned. To increase the accuracy of the experimental data, 100 image pairs for each of the 12 phases seen in Figure 3.8 are taken and the resultant vector fields calculated using these 100 image pairs are averaged to have a phase-averaged result. Taking images from the 100 consecutive cycles and averaging them results in enhanced statistical convergence. To capture 100 images at the same instant, the computer controlled pump sends a signal to the laser system at the desired instant for each cycle and the laser is sent to the measurement plane. An above 90% good vector percentage is aimed for each image pair, and mostly, above 95% good vector percentage is achieved. During the experiments, sufficient number of particles is crucial to have

high percentages of good vector. The number of particles inside the interrogation areas can be seen in Figure 3.9. Time delays between image pairs are 500-800 μs for Patient-Specific Aneurysm and 1000-1700 μs for Patient-Specific Healthy Aorta.

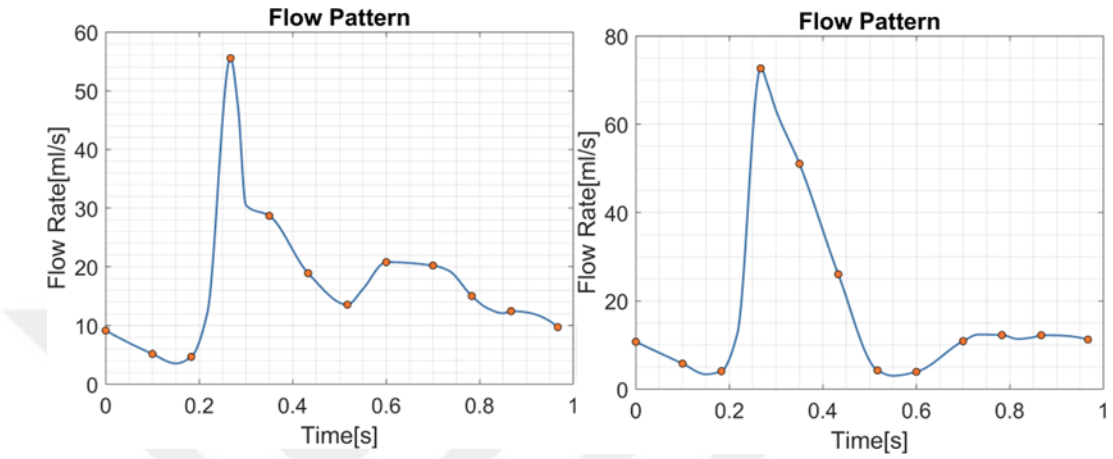

Figure 3.8. Flow patterns and the 12 instances which the PIV data are taken from. Healthy abdominal aorta (Left) & abdominal aortic aneurysm (Right).

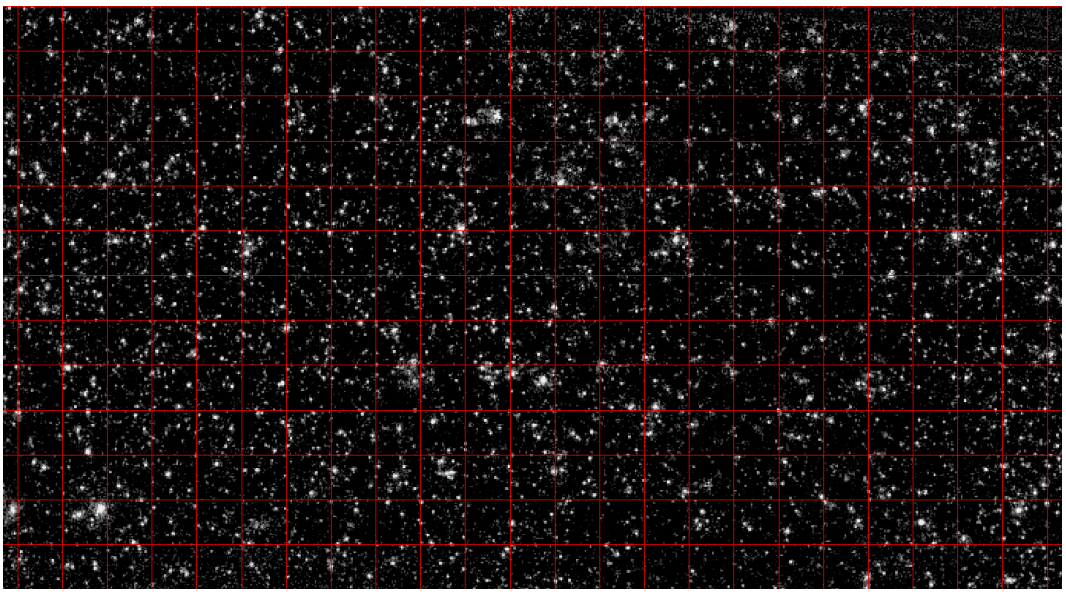

Figure 3.9. Real sized interrogation areas and the seeding particles inside

To process the images, flow domain is divided into interrogation areas of 32 x 32 pixels with 50% overlap for both geometries. 32 x 32 pixels are equal to 1.5 x 1.5 mm. Fast Fourier Transform (FFT) correlator is selected as the cross-correlation algorithm. A technique called zero masking is used to increase the accuracy of the PIV during the WSS calculations (Hochareon, 2003). This technique uses a polygon with many points to fully capture the irregularities in the geometry wall. With that way, processing the areas outside the flow domain and a possible bias to zero velocity in these areas is prevented.

Another processing step in PIV is background subtraction. To reduce the noise in the image, PIV software calculates an average light intensity and subtracts this intensity from the images. That way, it is possible to have an entirely black background and highlight the seeding particles. The difference between the raw image and the background subtraction applied image can be seen in Figure 3.10.

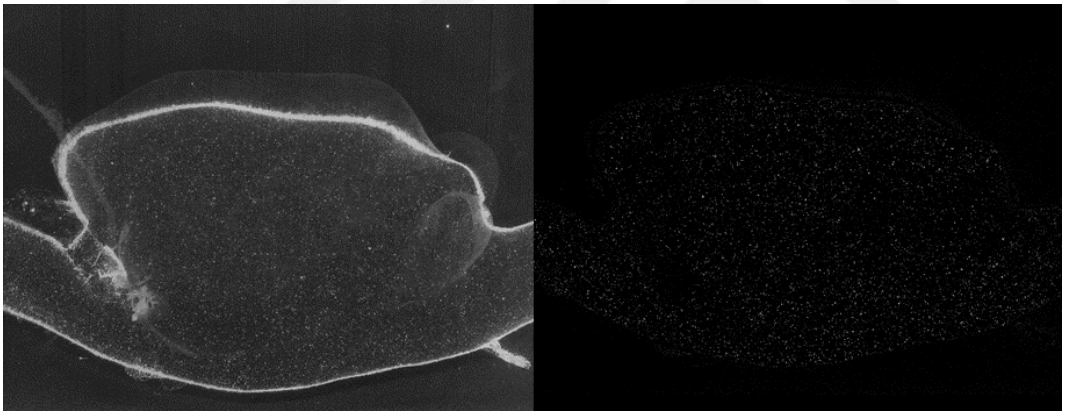

Figure 3.10. Background subtraction process. Raw image (Left), background subtracted image (Right)

After these processing steps, velocity vectors are calculated and validated by comparing them with neighbor vectors. This study uses local mean validation with a 5 x 5 square grid to validate a vector. These validated vectors are called “good vectors.” At every phase in both geometries, it is expected to have above 90 % good

vector. If this condition is satisfied, then the images are reprocessed with smoothing. Smoothing is a low-pass filtering method where every reference vector is replaced by the Gaussian-weighted mean of the neighboring vectors. Velocity field is calculated following the smoothing application, and the final results are obtained. An example of this velocity field can be seen in the Figure 3.11.

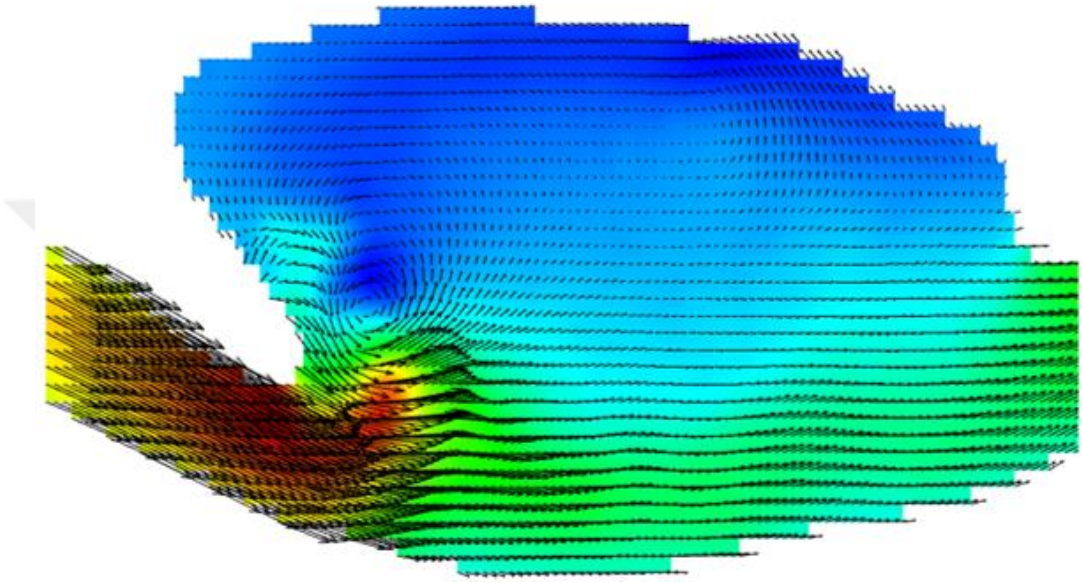

Figure 3.11. Velocity field obtained with PIV

3.2 Experimental Matrices

3.2.1 Measurement Planes

Since PIV with a single camera provides a planar velocity field, selecting appropriate measurement planes that can capture created vortices is crucial. The selected measurement planes and the resultant cross-sections for the healthy abdominal aorta and aneurysm models can be seen in Figures 3.12 & 3.13 respectively. Laser planes are represented with green dashed lines.

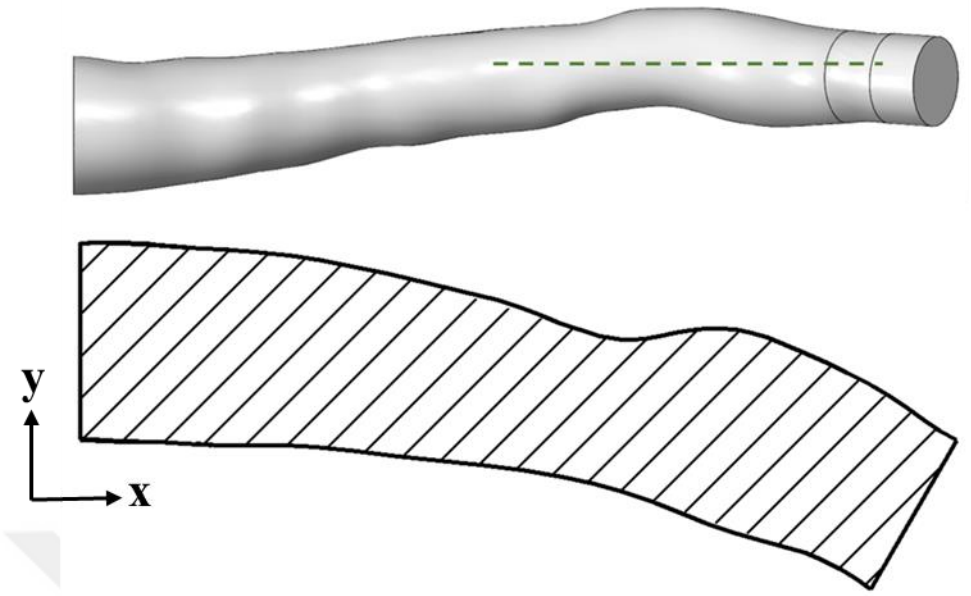

Figure 3.12. Laser plane (Upper) and resultant measurement area (Lower) for the healthy abdominal aorta

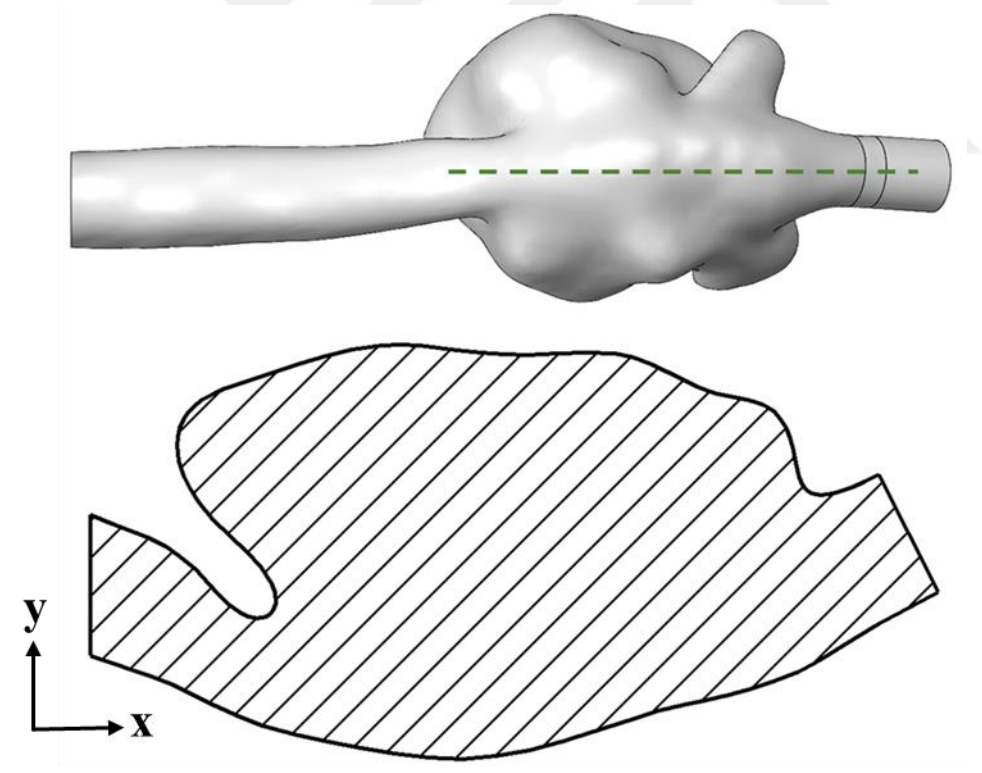

Figure 3.13. Laser plane (Upper) and resultant measurement area (Lower) for the AAA model

3.2.2 Flow Patterns and Characteristics

Realistic physiological flow patterns are provided as the pump outlet for both geometries. Flow patterns measured at the inlet of both geometries was presented in Figure 3.8. Flow parameters for both geometries can be seen in Table 3.2. Also, an additional experiment with the steady flow is performed for the WSS validation purposes. To compare the WSS results for the healthy abdominal aorta with Hagen-Poiseuille flow result a steady flow is suplied.

Table 3.2. Flow characteristics for both phantoms

	Physiological Flow			*Steady Flow*
Aorta Model	*Flow Rate Range (min-max)[ml/s]*	Re_{mean}	α	*Re*
AAA Model	3-72.5	288	12.98	-
Healthy Aorta	4-56	274	12.98	845

The difference between the minimum and maximum flow rate values result in sudden pressure fluctuations in the cardiac cycle. As the consequence of this pressure fluctuation, deformations in experimental phantoms occur. To conserve the measurement accuracy, deformations in the phantoms should be kept minimal. Maximum diameter deformations for both phantoms are recorded and they can be seen in Table 3.3.

Table 3.3 Maximum diameter deformations in a cardiac cycle for both phantoms

Aorta Model	*Maximum Diameter Deformation (%)*
AAA Model	3.5
Healthy Aorta	2.2

Stokes number is another parameter that should be investigated to ensure seeding particles are completely tracking the fluid. Stokes number for the used flow arrangment and seeding particles is found to be much less than 0.01. This ensures the seeding particles completely track the BMF flow.

3.3 Error Control in the Experiments

First step in error control is checking the repeatability of the experimental measurements under physological flow pattern. To increase the repeatability of the setup, BMF temperature is checked constantly and kept at 23 ± 1 ℃. Since the viscosity of the glycerol has a strong dependency on the temperature, keeping the temperature constant is cruical to increase repeatability. To check the repatability of the results, flow rates of the 12 phases are recorded from repeated experiments. Even for the experiments which are realized in separete days, below 5% deviation goal is achieved.

Second and final step of the error control is checking the deviations between the 100 images taken for phase averaging. This is done manually by checking the minimum and maximum velocity values of the images to prevent any measurement abnormalities. Again a below 5% deviation is achived for most of the images. The images with major abnormalities are also excluded from the phase averaging.

3.4 WSS Calculation from the PIV Results

3.4.1 Preliminary Processes for the WSS Calculation

WSS calculation from the experimentally obtained velocity field requires a methodology development. This WSS calculation method involves several steps. These steps must be taken care of with great concern to avoid additional errors in WSS calculation. Please note that this methodology is developed based on a previous study realized in the same laboratory (Türk, 2016).

WSS calculation from the experimental data methodology starts with determining vessel wall location. Determination of the vessel wall location is realized with a technique called zero masking (Hochareon, 2003). Masking is drawn adjacent to the inner area of the vessel boundary to avoid bias toward zero velocity. The zero-masking technique using a polygon can be seen in Figure 3.14. The bright border between the BMF and PDMS is visible in these images. These bright pixels are excluded from the domain to prevent a bias to low velocity gradients.

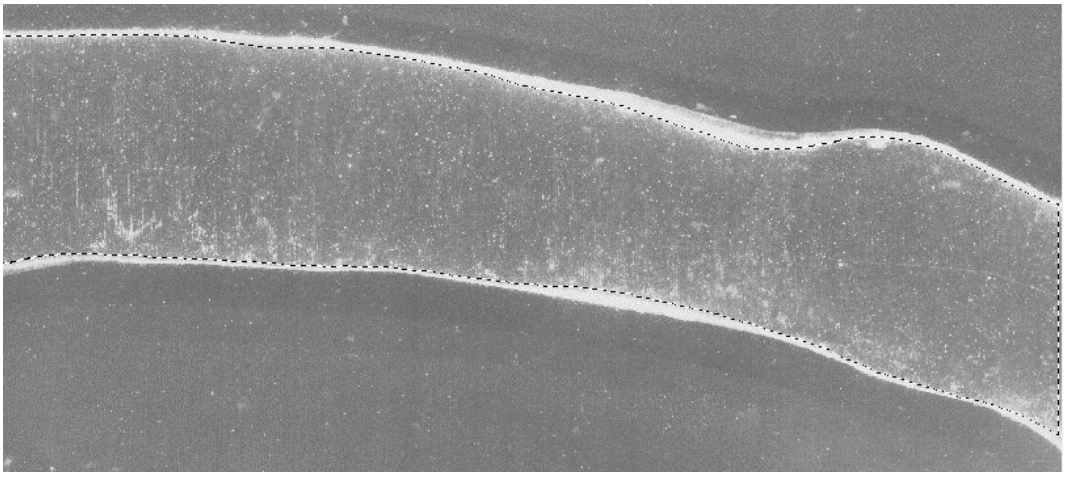

Figure 3.14. Zero masking process. The polygon used to mask the domain is the dashed line adjacent to bright vessel wall.

The location of the vessel wall is extracted from the PIV software in terms of pixel values. Pixel values of the vessel wall location need to be converted into mm to be used in the custom MATLAB code. This is done using the spatial calibration constant of the PIV camera. After importing these discrete polygon points to the custom MATLAB code, a spline is fitted between these points to obtain a continuous vessel wall. The obtained continuous vessel wall can be seen in Figure 3.15.

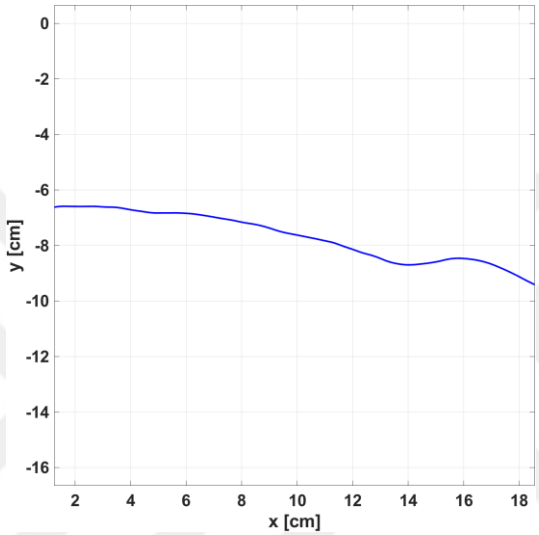

Figure 3.15. Continuous vessel wall obtained with the spline fit

Please note that Figure 3.15 shows the upper half of the healthy aorta wall. The same procedure is applied to obtain the lower wall also. Additionally, the vessel wall with the discrete velocity points obtained from the PIV can be seen in Figure 3.16.

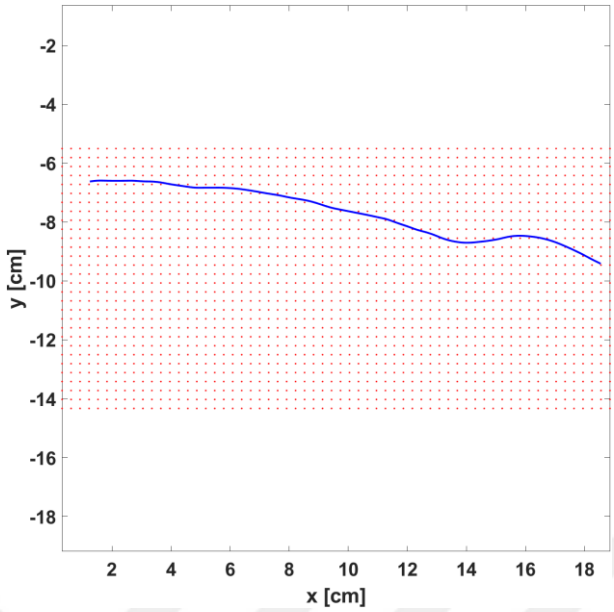

Figure 3.16. Discrete PIV data with the fitted vessel wall

As visible in Figure 3.16, the velocity field obtained with the PIV also includes data points outside the vessel walls. Also, please note that these data points represent the U-velocity values obtained from the PIV experiments. Data points outside the flow domain are due to the larger size of the region of interest compared to the masked region. These data points are incompetent and must be excluded from the WSS calculation procedure. The obtained field after the elimination of the data points outside the aorta vessel is presented in Figure 3.17. It can be observed from the figure that only the data points inside the flow domain remain after the elimination process.

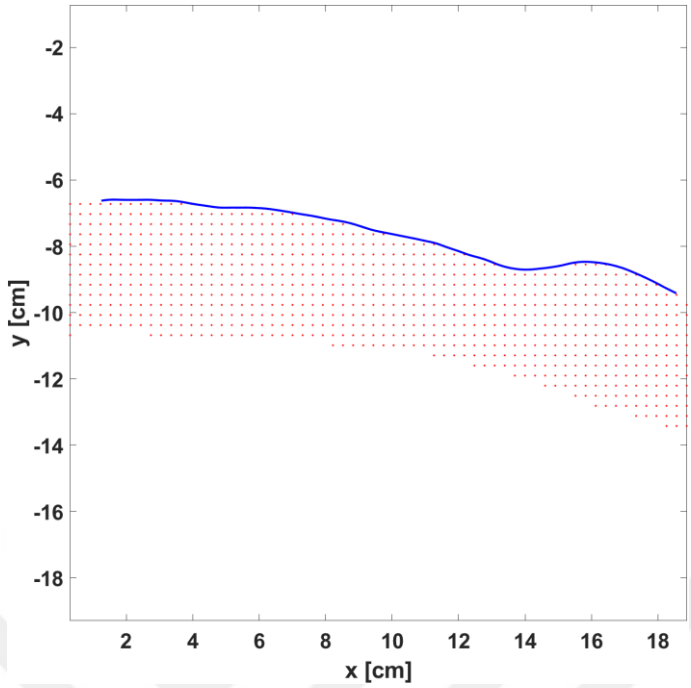

Figure 3.17. Flow domain obtained proceeding the elimination of the data outside the domain

To calculate the WSS in the vessel wall with high resolution, 500 points with equal intervals are selected. Some portion of these discrete data points on the vessel wall can be seen in Figure 3.18.

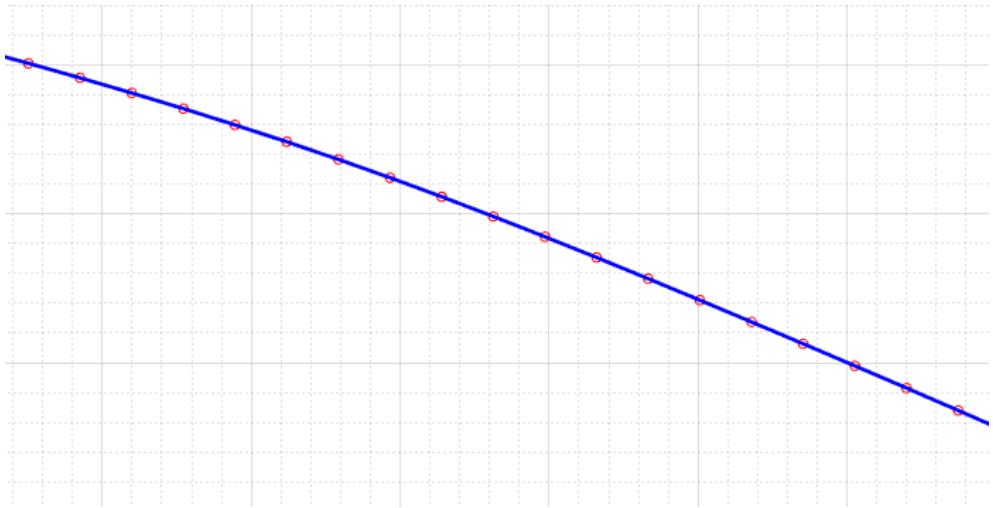

Figure 3.18. Vessel wall (Blue line) with evenly spaced data points (Red dots) on it

Another crucial phase of the WSS calculation is the determination of the wall-normal directions. This is realized with the help of 500 discrete data points on the vessel wall. The vector drawn between the two consecutive data points is assumed to be tangent to the vessel wall. Therefore, the vector normal to the wall tangent should be in the wall-normal direction. Since the wall-normal directions are obtained, the velocity values in that direction can be accessed and used in WSS calculations.

Before WSS calculation, the final step is obtaining a continuous velocity field from the discrete PIV data. PIV calculates the average velocity value inside a grid and assigns this value to a vector at the grid center. Therefore the result of the PIV is a discrete velocity field. A continuous velocity field should be obtained to ensure a velocity value at the wall-normal direction for every data point on the vessel wall. This is realized using “natural neighbor interpolation” (Sibson, 1981). Subsequently, a continuous velocity field inside the aorta is obtained.

3.4.2 WSS Calculation Phase

WSS can now be computed with the determination of wall-normal direction and the continuous velocity field inside the aorta. The first stage of the WSS calculation is obtaining the velocity values in the wall-normal direction. This process can be seen in Figure 3.19.

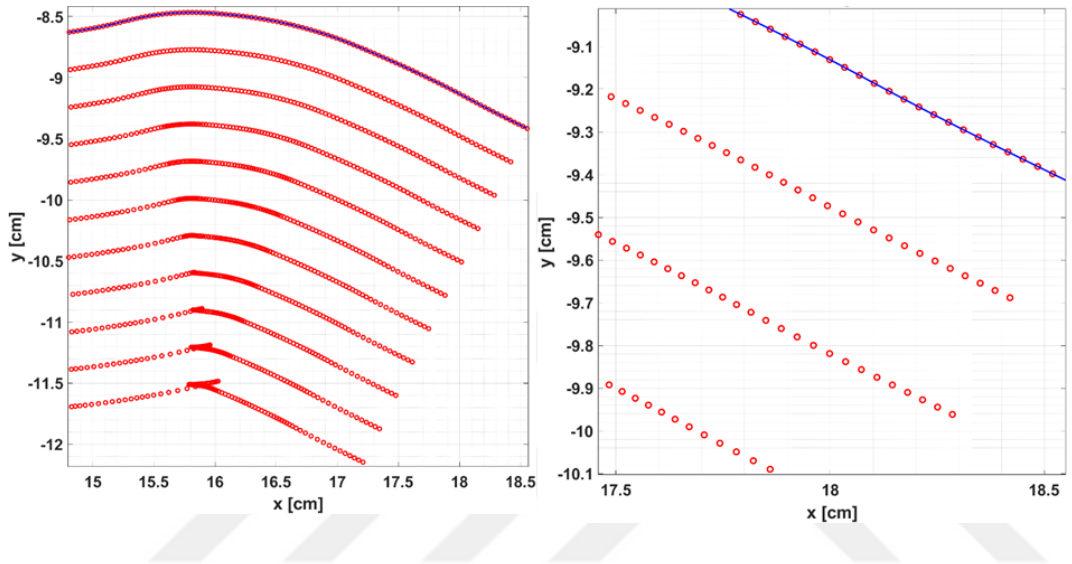

Figure 3.19. Data points in the wall normal direction. Whole 11 data points (Left), zoomed in view (Right)

As presented in Figure 3.19, 11 data points in the wall-normal direction, including one data point on the vessel wall, are captured. The interval between these data points in the wall-normal direction is selected equal to the grid size. The grid size is 0.3043 mm for the healthy aorta. One thing to consider before the WSS calculation is that the selected data points are u-velocities in the x direction. Therefore they can not be used in the WSS calculations directly. To use them in the calculations, the components of these velocities, which are tangent to the wall, should be obtained first. The projection of the particular u-velocity vector on the wall tangent vector is calculated and used in the WSS calculations. Additionally, the wall boundary condition is assumed to be no slip; therefore, the data points on the wall are granted 0 tangent velocity magnitude.

In the next step of the WSS calculation, a continuous velocity profile should be fitted to the discrete data points presented in Figure 3.19. Fit types and initial data point selection are the parameters used for an accurate WSS estimation.

3.4.2.1 Velocity Profile Fit Types

In this study, four different velocity profile fit types are considered. These are:

1) Linear Velocity Profile

2) Second Order Polynomial Velocity Profile

3) Third Order Polynomial Velocity Profile

4) Cubic Spline Velocity Profiles

The velocity profiles obtained near the wall using these four methods can be seen in Figure 3.20. A point approximately halfway through the aorta is used for this plot.

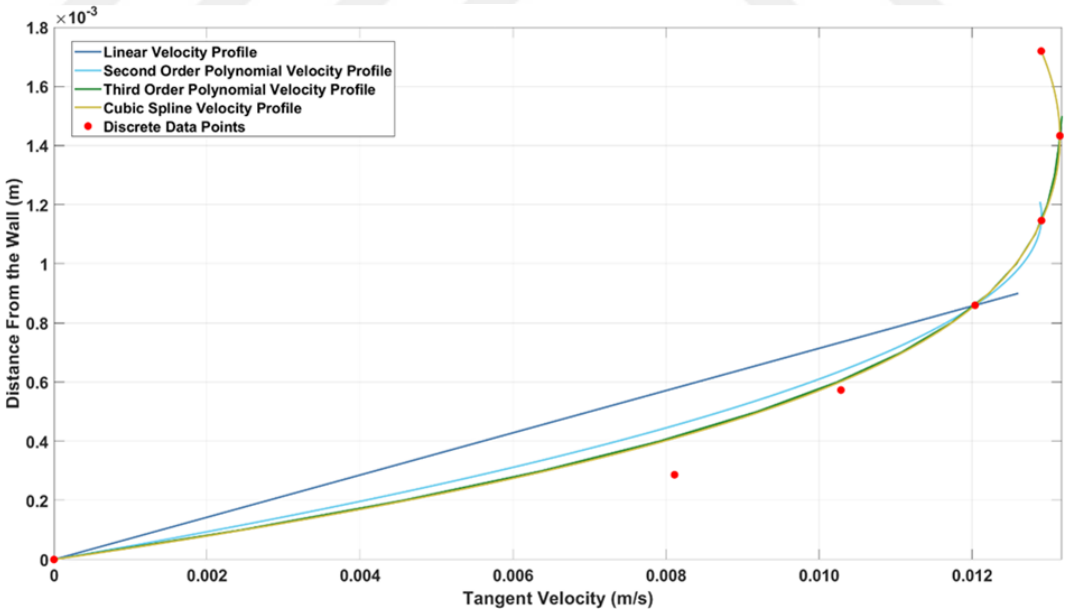

Figure 3.20. Velocity profiles obtained with four different fit types. Third data is used as the initial data for all fit types.

The velocity profiles visible in the Figure are obtained using the third data point as the initial data point. Please note that the data point on the wall is used in every velocity profile type, and therefore the count for the initial data point starts after the data point on the wall. As apparent from the Figure, besides the linear fit, all velocity profiles have approximately the same slope near the wall, which indicates similar wall shear stress values. Another aspect to highlight from this plot is the number of necessary data points for each velocity profile. While the linear velocity profile needs two discrete data points, five data points are required for an effective cubic spline fit. Second and third-order polynomial profiles need three and four data points, respectively. Taking velocity information from five distinct points makes the cubic spline a more robust method for complex flow patterns compared to other profiles (Van Ooij et al., 2013).

3.4.2.2 Initial Data Point

Estimating WSS using PIV has difficulties, as mentioned in the Section 2.8. The primary challenges are wall location estimation and the accuracy of the velocity data near the wall. The wall location estimation problem is overcome with the zero masking method. The accuracy problems of the PIV data near the wall were also mentioned in Section 2.8. To overcome this problem, the first PIV data that will be used should be selected carefully. The initial data being too close to the wall can reduce the measurement accuracy due to light reflection from the boundary and the high signal noise caused by this reflection. Being too far from the wall also causes problems. Selecting an initial data point that is too far from the wall makes capturing high velocity gradients in the viscous boundary layer impossible. Therefore an optimum initial data point should be found to calculate WSS accordingly. The effect of initial data point selection on the velocity profiles can be seen in Figure 3.21. Note that these velocity profiles are obtained from the same location as Figure 3.20.

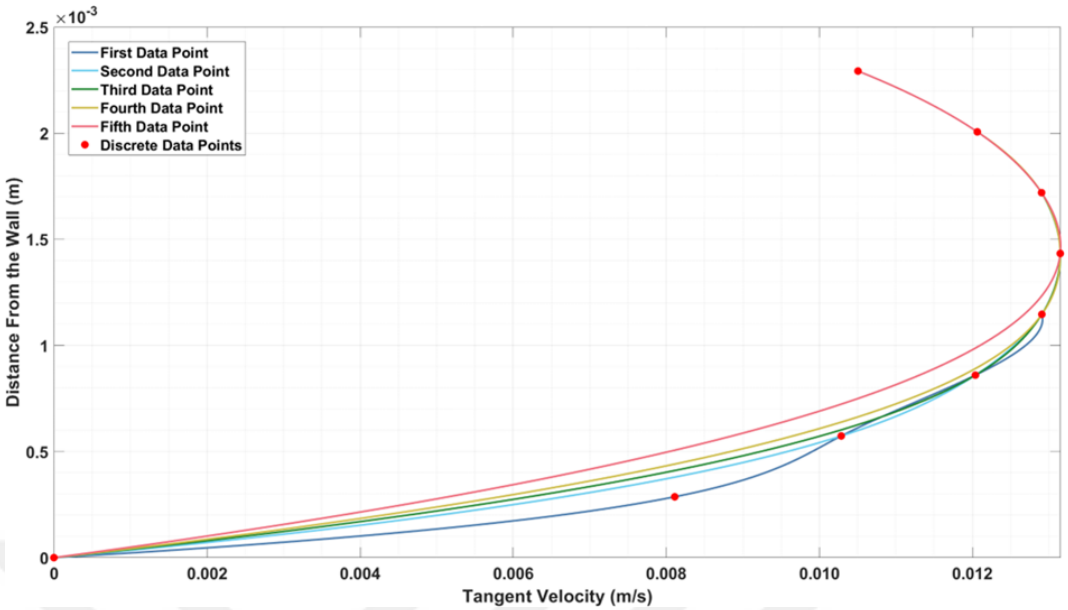

Figure 3.21. Effect of the initial data point selection to the velocity profile. Cubic spline velocity profile is used for all five velocity profiles.

From Figure 3.21, the discrepancy between the five velocity profiles can be observed. Although all profiles are obtained from the cubic spline interpolation, initial data point selection affects these profiles significantly. These discrepancies are parallel with the considerations mentioned previously. Selecting an initial data point that is too close to the wall causes high velocity gradients. As observed from Figure 3.21, using the first data point as the initial, which is 0.286 mm away from the wall, results in the highest velocity gradient. However, using the fifth data point as the initial, which is 1.4 mm away from the wall, generates the lowest velocity gradient. Complex flow structures inside the aneurysm also need to be considered during the initial data point selection. Selecting the initial data point too distant from the wall can lead to inadequacy in capturing the boundary layer seperations occuring near the wall. So an initial data point which is distant enough to avoid overestimation of the WSS and close enough to be able to capture possible boundary layer seperations is cruical in this stage.

These figures show that both velocity profile fit selection and initial data point selection significantly affect the WSS calculation. These parameters need to be appropriately selected to have an accurate WSS estimation.

CHAPTER 4

RESULTS AND DISCUSSION

This chapter presents the streamline and contour plots for both healthy aorta and AAA. These contour plots include U-velocity, ω_z and λ_{ci} (Swirling Strength). Additionally, comparison of the WSS results for the healthy aorta with a previously studied aneurysm model can also be seen in this chapter.

4.1 U Velocity

In this section, the contour plots for the x direction velocity can be observed. Please note that, different ranged legends are used for the contour plots of healthy aorta and AAA. The reason behind this can be seen in Figure 4.1. Using the same legend for both geometries makes the flow patterns of the healthy aorta invisible.

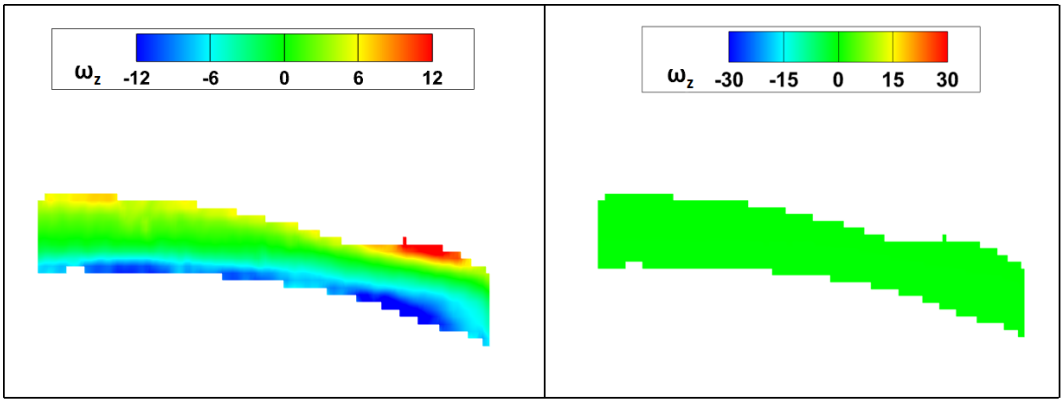

Figure 4.1. ω_z contours for the healthy abdominal aorta. Narrower legend range (Left), wider legend range (Right)

Additionally, this section will compare the axial velocity contours for the patient-specific aneurysm and the healthy aorta model. Velocity in the x direction is a parameter that can explain the general flow characteristics in the aneurysm. Figure 4.2 shows the axial velocities at the earlier stages of a cardiac cycle for both geometries. The explanation by Yu (2000) is also valid in the patient-specific aneurysm model. Yu described the flow in an aneurysm as a jet flow and a recirculation region that surrounds the jet flow with relatively low velocity magnitudes. Negative velocity values can also be observed in the recirculation region of the aneurysm.

The main difference between the aneurysm and the healthy aorta is the absence of the recirculation region in the healthy aorta. Low negative axial velocity values in the healthy aorta are errors arising from the PIV measurements. These low-velocity values do not represent a recirculation region. Instead, it represents the viscous boundary layer sourced from the vessel wall.

The recirculation region in the aneurysm sac is apparent in the earlier stages of the cardiac cycle. Negative velocity values near the aneurysm sac wall indicate a possible vortical structure. Also, in Figures 4.2.4a & 4b, a high-velocity region at the inlet of the vessels due to the peak at the cardiac cycle can be observed.

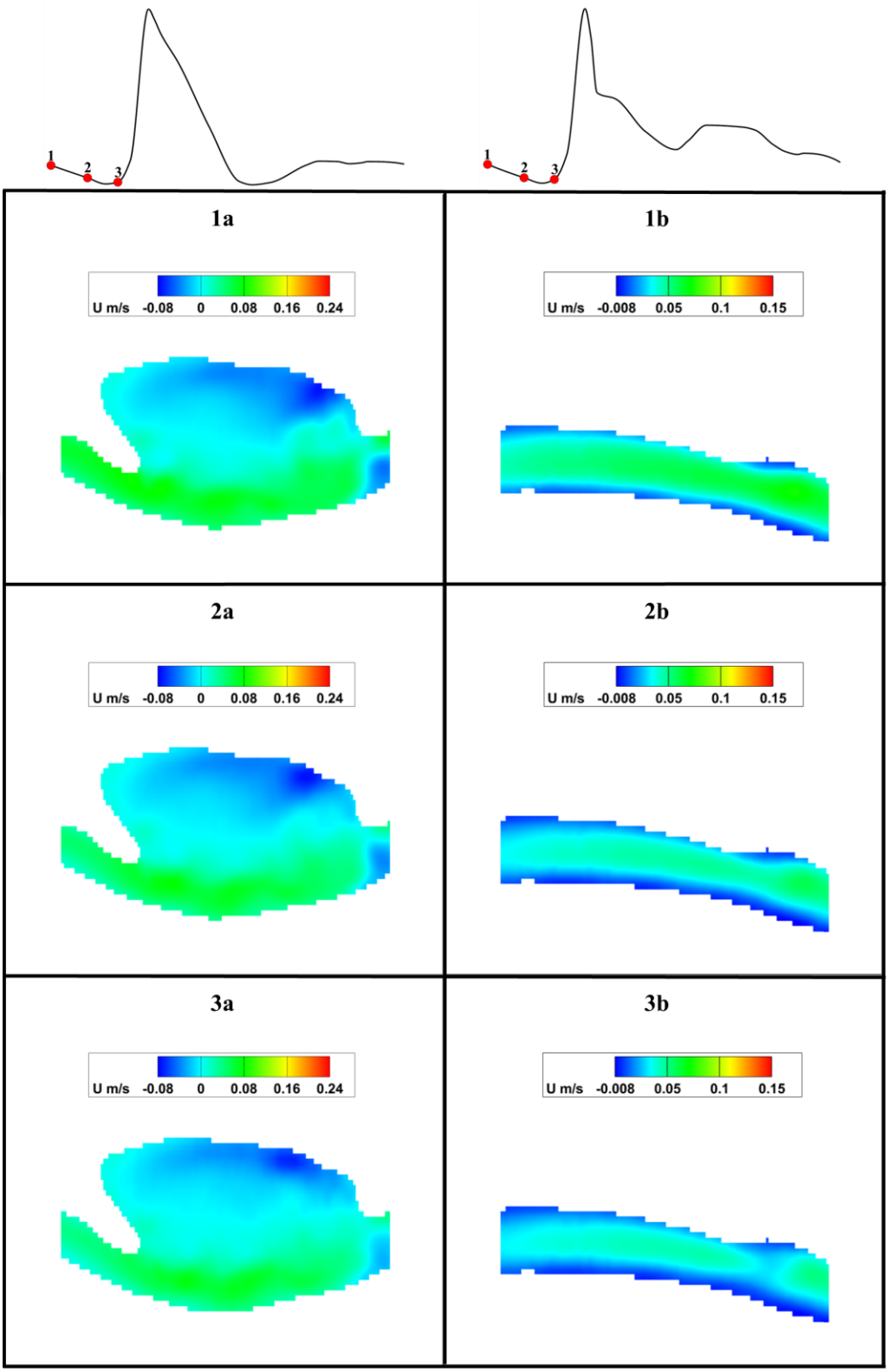

Figure 4.2. U-velocity contours for the first three phases of the cardiac cycle. AAA (Left) and healthy aorta (Right).

The same trend for both geometries can still be observed in the latter stages of the cardiac cycle. Low-velocity recirculation region is still visible in the aneurysm model. When all phases of the aneurysm are investigated, rotation of the negative velocity region in the counter clockwise direction is visible. This is also a possible indicator of a moving vortical structure in the aneurysm sac. Additionally, the high-velocity jet flow migrates toward the outlet. During this migration, the velocity of the jet flow decreases due to steep deceleration in the cardiac cycle. Viscous friction between the jet flow and both the aneurysm wall and the fluid volume at the recirculation region can also be a factor in the velocity decrease.

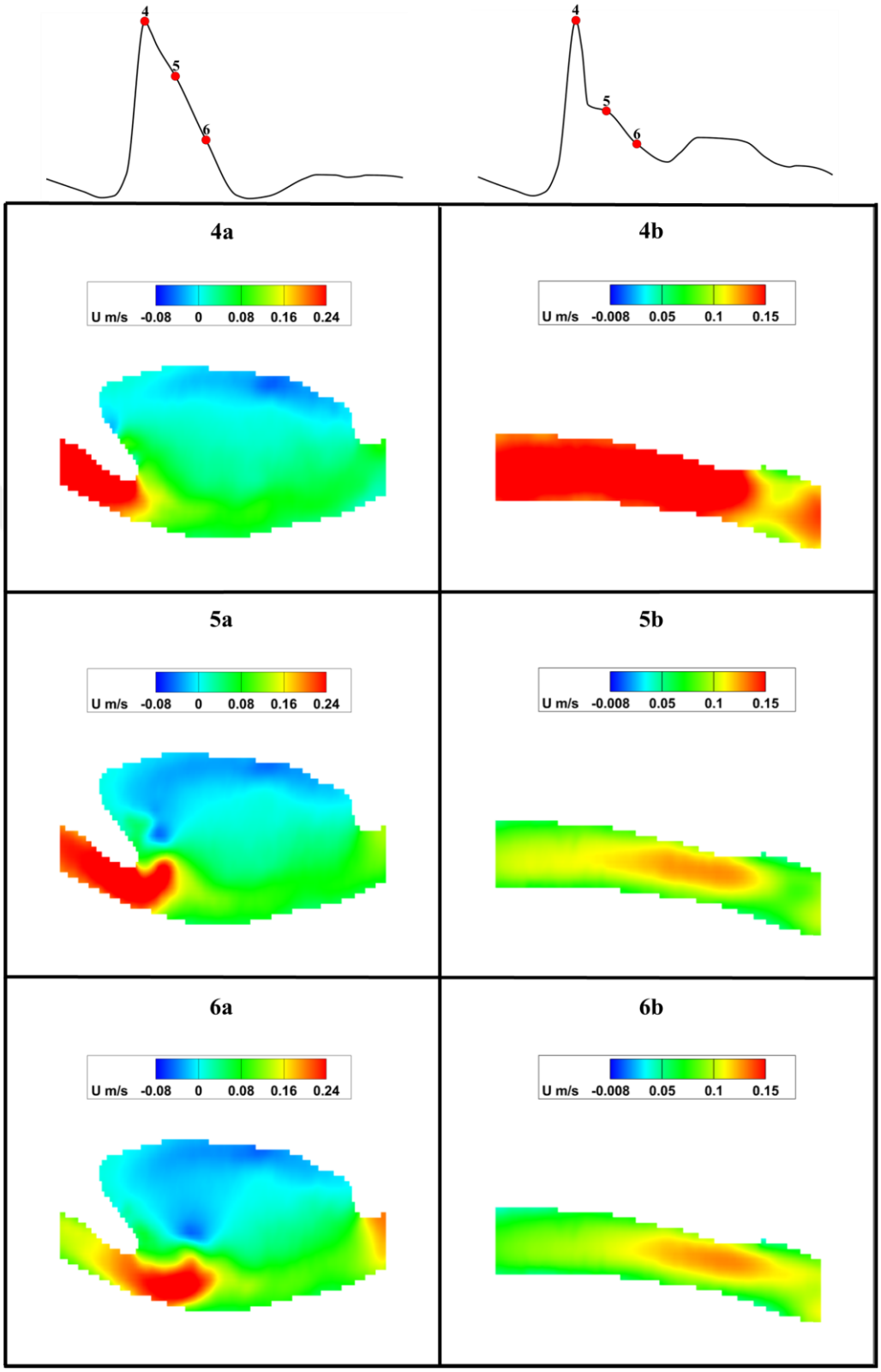

Figure 4.3. U-velocity contours for the deceleration phase of the cardiac cycle. AAA (Left), healthy aorta (Right)

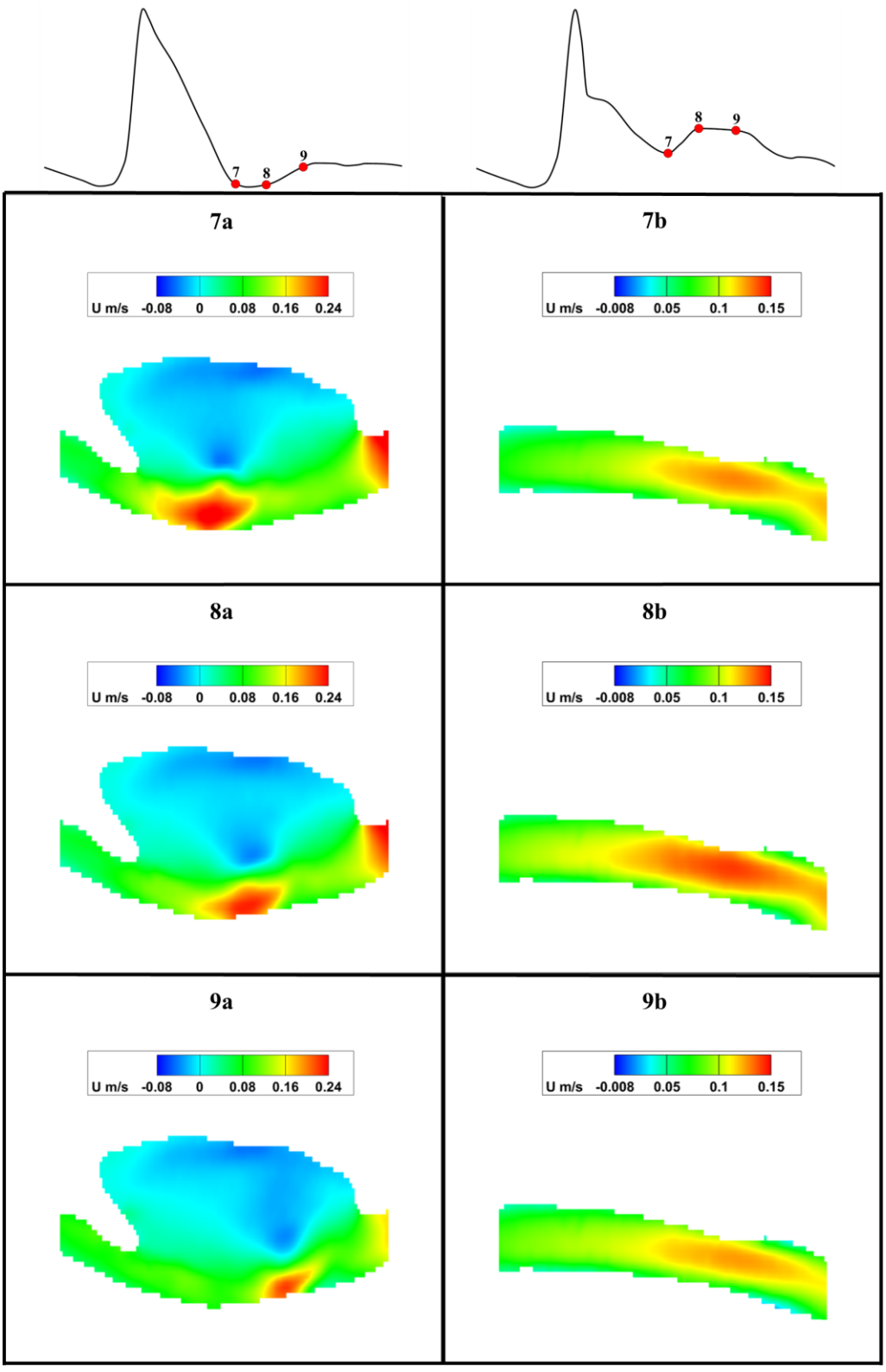

Figure 4.4. U-velocity contours for the post deceleration phases. AAA (Left), healthy aorta (Right).

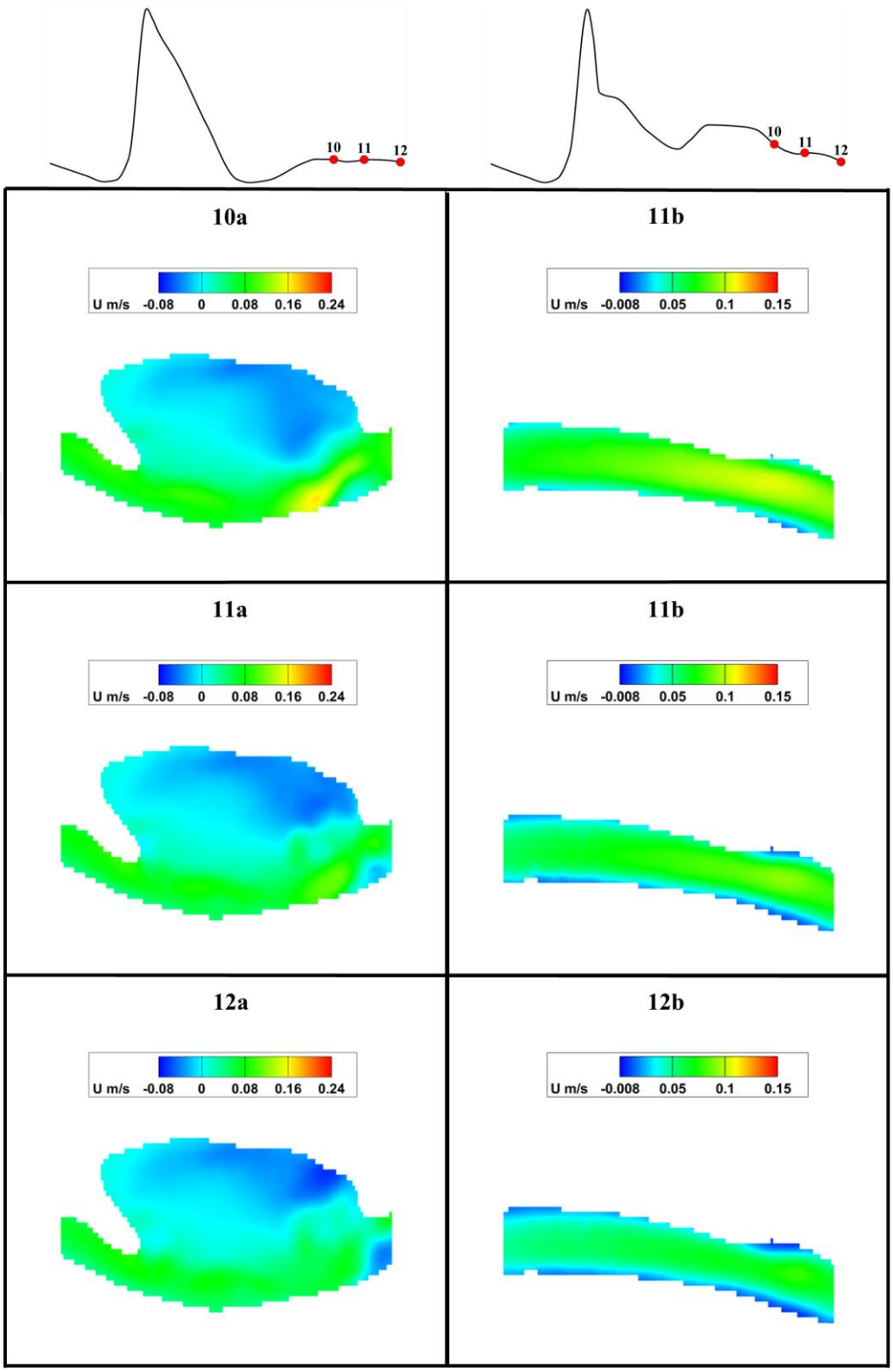

Figure 4.5. U-velocity contours for the last three phases of the cardiac cycle. AAA (Left), healthy aorta (Right)

4.2 Streamline Patterns

This section will discuss the streamline patterns obtained from the velocity fields of the aneurysm and healthy aorta model. Figure 4.6 presents the first four stages of a cardiac cycle. Although the streamline patterns inside the healthy aorta look simple, the aneurysm model involves more complicated patterns inside. In the first three stages of the cycle, the recirculation region inside the aneurysm sac is more apparent with the streamlines compared to axial velocity contours. Additionally, a possible vortex core region can be observed in the aneurysm model. Due to the migration of this possible core inside the aneurysm sac, particles can not complete a full rotation, making it impossible to conclude this region as a vortex core from a streamline pattern. Another interesting observation in the aneurysm model is a rotating streamline pattern near the outlet. This possible vortex core is produced at the previous cardiac cycle and migrated toward the outlet. Streamlines inside the healthy aorta model mostly follow the vessel walls. This characteristic shows a resemblance to a pipe flow. The only exception for this characteristic is observed near the outlet. Due to a minor expansion in the vessel diameter, flow separation occurs, resulting in a whirling streamline pattern in these regions. The flow patterns at the peak flow rate (see Figure 4.6.4a & 4b) differ significantly from the previous phases for both geometries. With the flow rate reaching its maximum, the adverse pressure gradient is overcome, and the recirculation region disappears from the aneurysm sac with the whirling streamline patterns it involves. This effect is also apparent in the healthy aorta model. Even minor areas with flow separation and whirl-like streamline patterns disappeared from the healthy aorta with the impact of peak flow rate.

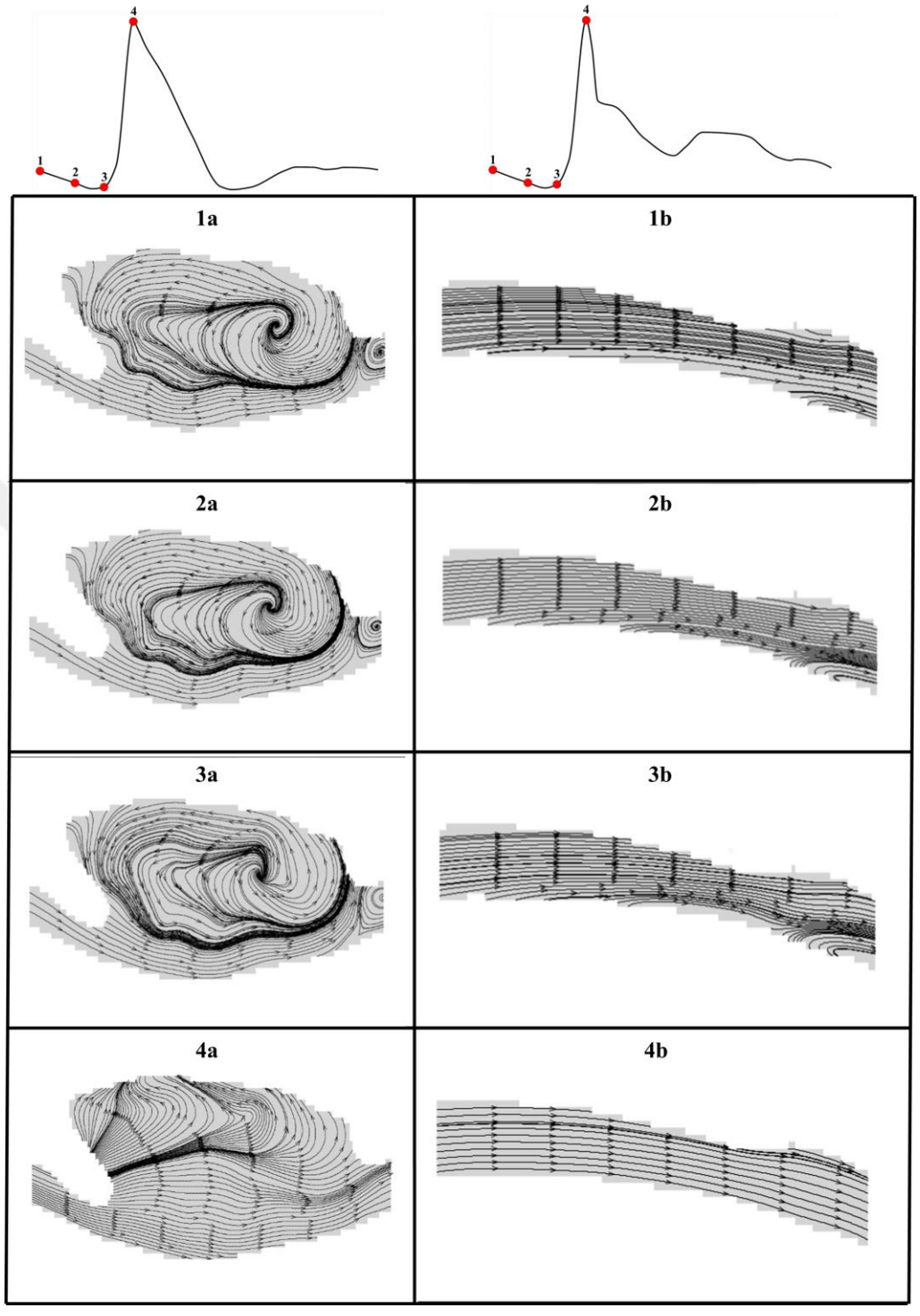

Figure 4.6. Streamline patterns for the first four phases of the cardiac cycle. AAA (Left), healthy aorta (Right)

Figure 4.7 presents the three streamline patterns obtained from the steep deceleration phase and a last phase just after this steep deceleration. For also these four phases, the aneurysm model involves a more complicated flow pattern relative to the healthy aorta. While the healthy aorta just involves streamlines along the main flow direction and follows the vessel wall perfectly, convolute flow patterns are evident in the aneurysm model. At the start of the deceleration phase, a rotating flow pattern is visible near the aneurysm inlet. This rotating flow pattern indicates a possible vortex core. Another interesting observation is the migration of this rotating flow pattern. With the start of the deceleration phase, a possible vortex core becomes visible and keeps translating toward the outlet for the rest of the cycle. This rotating streamline pattern also has a visible impact on the main jet flow. It decreases the area that the jet flows through. That causes the acceleration of the jet flow, which can also be seen in Figures 4.3.6a,7a & 8a. Local flow accelerations can be seen from these figures. For the healthy aorta case, the trend formed by the peak flow rate also continues to be observed. Minor regions in the acceleration phase where the separation and whirled streamlines can be observed are also absent in the deceleration stage.

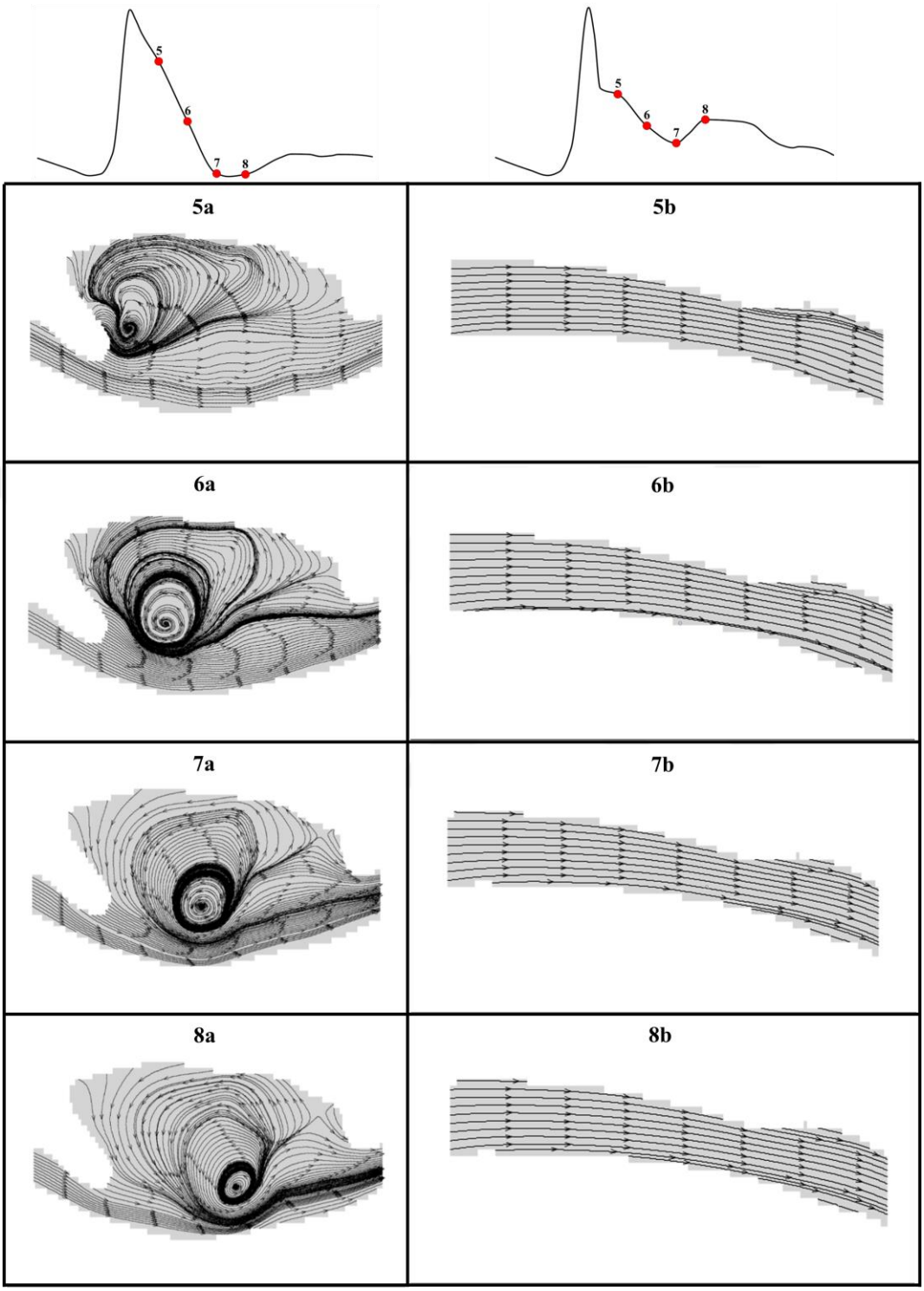

Figure 4.7. Streamline patterns for the deceleration phases of the cardiac cycle. AAA (Left), healthy aorta (Right)

Streamline patterns for the last four phases of a cardiac cycle are presented in Figure 4.8. Similar to the rest of the cardiac cycle, the aneurysm model involves more complicated streamline patterns in the last four phases. The primary trend evident in the aneurysm model is again the translation of the whirling streamline pattern. As a result of this migration, in Figure 4.8.9a, the collision of the whirling streamline pattern with the anterior wall of the aneurysm can be observed. Due to this collision, the shape of the whirling streamline pattern is modified, and another smaller-scale whirling pattern becomes visible at the outlet. This small-scale rotational pattern is the same pattern that is also noticeable in the first three stages of the cardiac cycle. Also, there are minor disturbances near the outlet in the last three phases of the healthy aorta. These disturbances lead to rotating patterns in the first three phases. Although axial velocity contours and streamline patterns give the first hints about vortical structures in the aneurysm, additional analyses are necessary to produce more solid results. To identify the vortical structures more definitively, vorticity magnitude and λ_{ci} results obtained from the velocity field are presented in the following Sections 4.3 & 4.4.

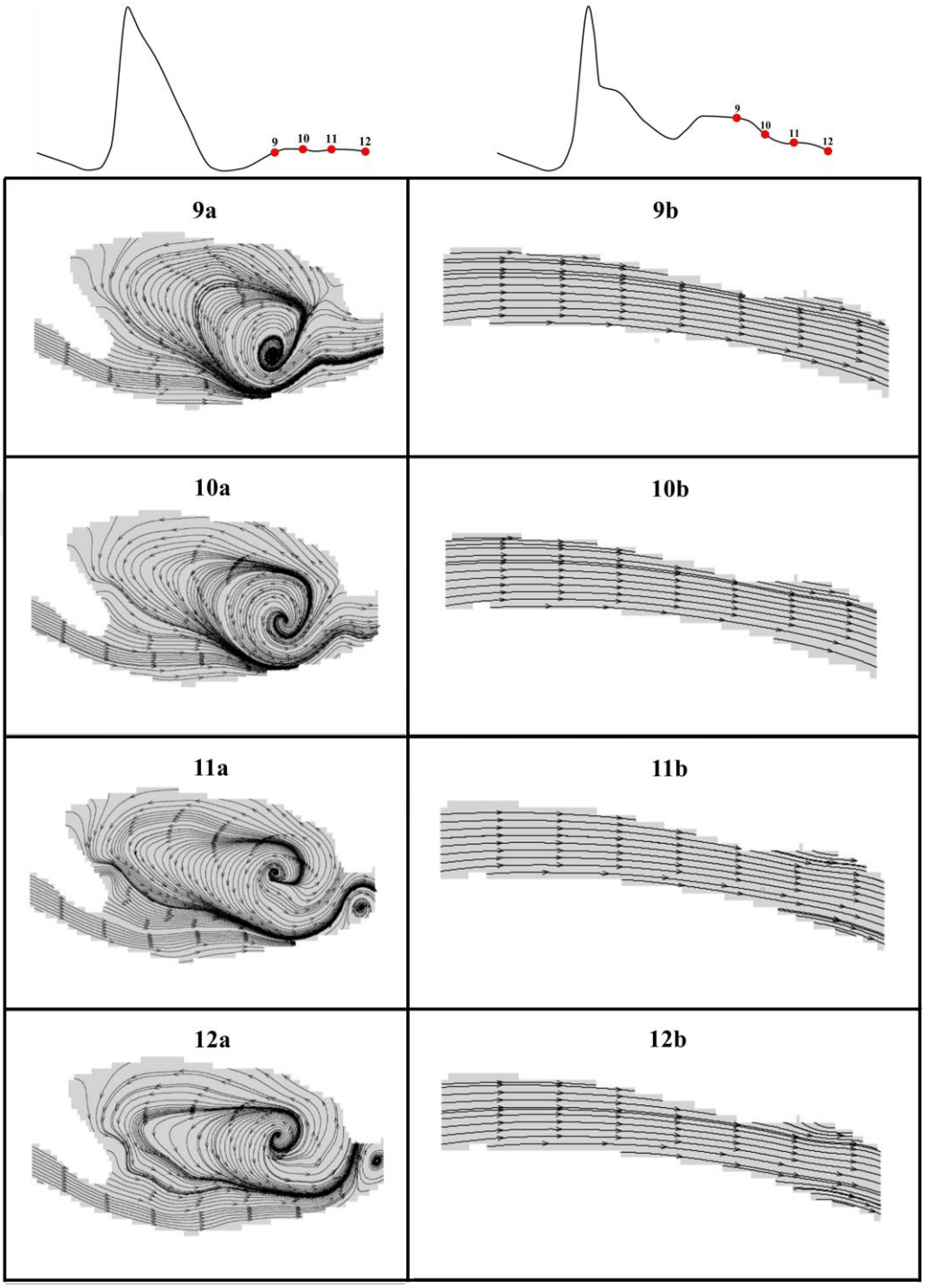

Figure 4.8. Streamline patterns for the last four phases of the cardiac cycle. AAA (Left), healthy aorta (Right)

4.3 Vorticity in the Z Direction

Vorticity value can be used to identify vortices in a flow field. One thing to consider is to differentiate shear layers formed due to vessel walls from the vortex cores. The vorticity magnitude criterion can not make this differentiation; therefore, it should be done manually.

The vorticity contours for the first three phases of a cardiac cycle are presented in Figure 4.9. In the first three phases of the aneurysm model, several weak vorticity magnitude regions are apparent in the aneurysm sac. The weak vortex regions near the inlet are the result of separation. The shear layer formed at the aneurysm inlet can not stay attached to the walls of the suddenly expanded aneurysm. Due to the adverse pressure gradient caused by the sudden area expansion, the shear layer rolls into a weak vorticity.

Weak vorticity regions near the outlet are mainly formed with the tearing of a strong vortex present in the aneurysm in the previous cycle. Tearing of this strong vortex can also be observed in Figure 4.8.11a. The vortex regions are getting weaker with the advancing phases. The vortices weaken due to the viscous friction with the low-velocity, non-rotational fluid volume inside the aneurysm sac.

Strong vorticity region at the aneurysm outlet is another compelling finding. The vorticity region at the outlet is a separate part of the torn secondary vortex. A portion of the torn vortex is then sucked into the outlet, resulting in the vorticity region observed in the first three phases. The vorticity region at the outlet also weakens with the advancing phases. This result is also parallel with the findings of the streamline analysis.

The high vorticity regions in the normal aorta primarily represent the shear layer formed near the vessel wall. A continuous region of non-zero vorticity is evident in the vicinity of the lower and upper vessel walls. In the first phase, a strong vorticity region exists at the upper wall, near the outlet. This is due to flow separation caused by the minor expansion. Although there is a minor flow separation, the largest vorticity magnitude in the healthy aorta is equivalent to those of the secondary vortices in the aneurysm. This relatively small vorticity magnitude also keeps decaying with the decreasing flow rate.

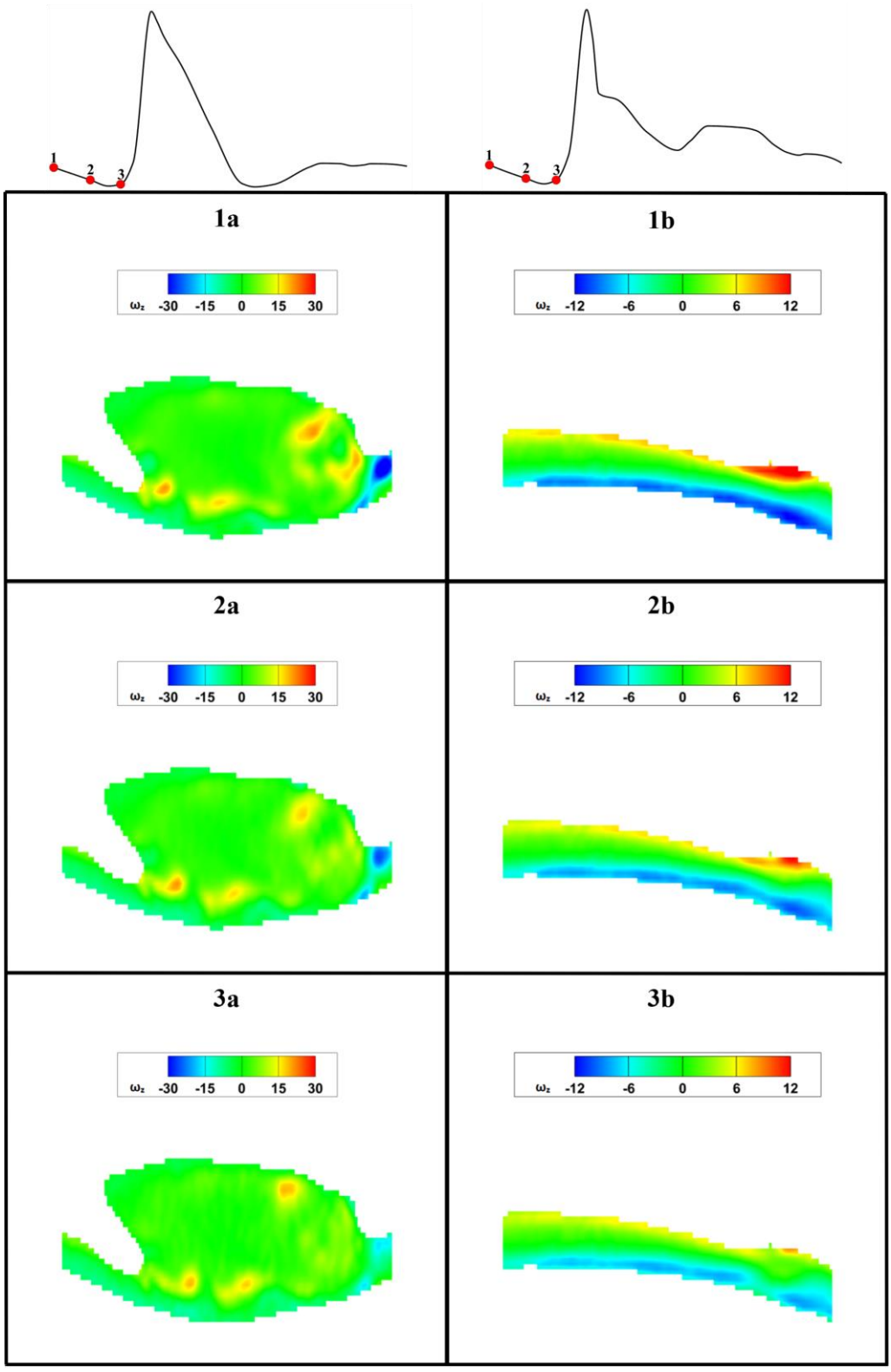

Figure 4.9. Vorticity contours for the first three phases of the cardiac cycle. AAA (Left), healthy aorta (Right)

Figure 4.10 presents the vorticity contour results for the following three phases. These phases involve the peak and deceleration portion of the cardiac cycle.

A segment of a strong vorticity region is evident near the expanding part of the aneurysm inlet. This strong vorticity region at the peak flow rate can be seen in Figure 4.10.4a. The primary vortex formed in the aneurysm is first seen at the peak flow rate, which is the end of the acceleration and start of the deceleration phases. With the steep deceleration and adverse pressure gradient in the aneurysm sac, some portion of this shear layer with strong vorticity rolls to form a vortex. This vortex starts to be detached from the aneurysm wall in the middle of deceleration. Detachment of the vortex from the aneurysm wall can be observed in Figure 4.10.5a. Another interesting phenomenon is observed in Figure 4.10.6a. Primary vortex formed in the previous phase produces another vorticity region with the same magnitude and opposite direction near the posterior wall. Kelvin's circulation theorem can explain this phenomenon (Kundu & Cohen, 2010). The primary vortex forms a counter-rotating secondary vortex from the existing shear layer near the posterior wall to preserve the total circulation in the aneurysm.

The vorticity magnitude analysis captures primarily the boundary layers near the vessel walls in the normal aorta. The boundary layers' and the minor separation zone's vorticity magnitude gets stronger in the deceleration. This trend can be observed in Figure 4.10.4b, 5b & 6b.

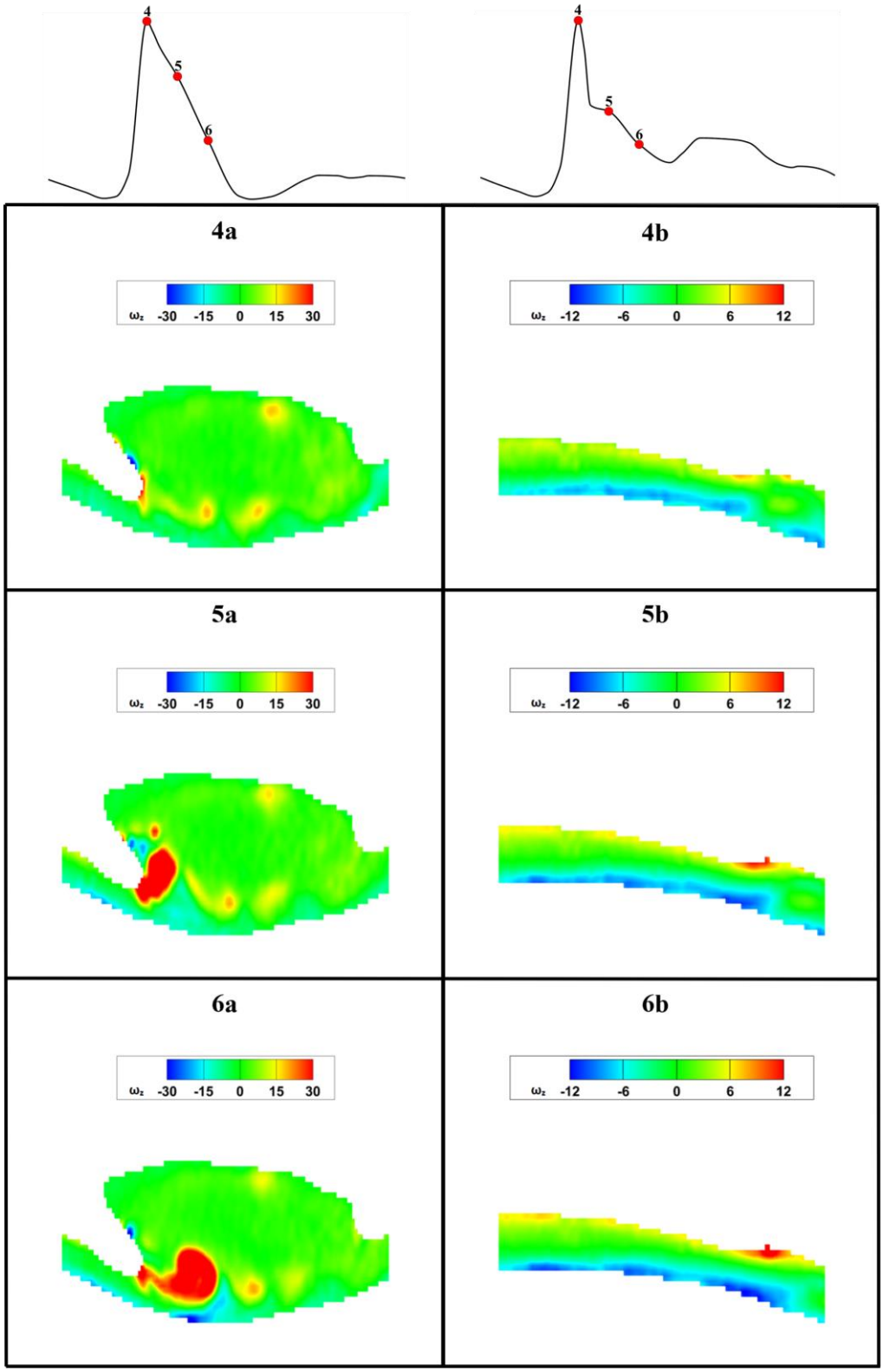

Figure 4.10. Vorticity contours for the deceleration phase of the cardiac cycle. AAA (Left), healthy aorta (Right)

The vorticity contours for the 7th, 8th, and 9th phases are presented in Figure 4.11. The principal trend observed in these contours for the aneurysm model is the migration of the primary vortex. In these phases, the primary vortex detaches entirely from the diverging part of the inlet and advances through the aneurysm. During the primary vortex's advancement, it reaches the posterior wall. In Figure 4.11.9a, the coupling of two counter-rotating vortices near the posterior wall is also noteworthy.

Vorticity magnitudes near the wall get stronger with the continuing phases in the healthy aorta. The strong vorticity region at the upper wall, apparent in the 1st phase, also starts to be visible again in the 8th and 9th phases.

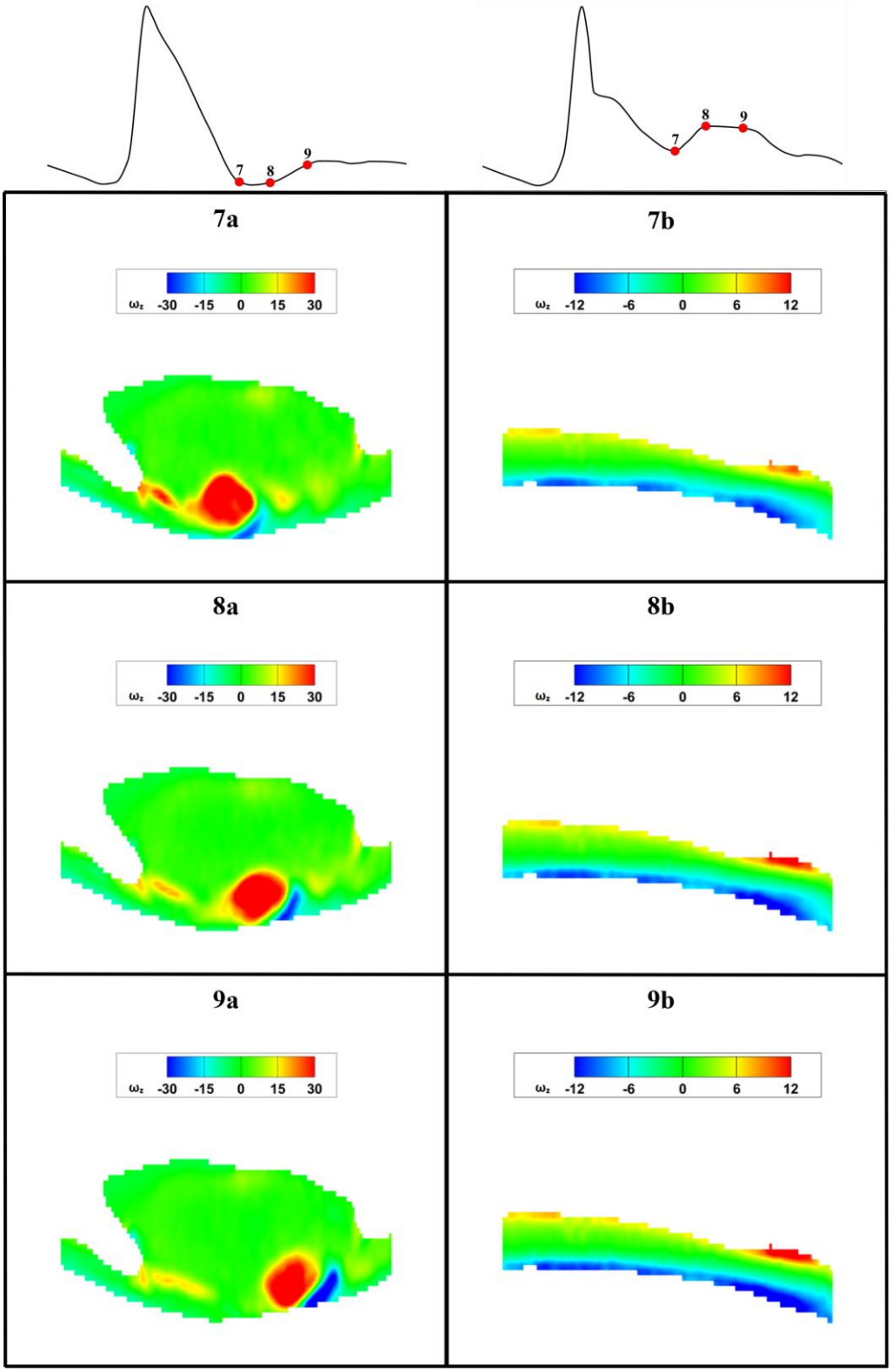

Figure 4.11. Vorticity contours for the post-deceleration phases of the cardiac cycle. AAA (Left), healthy aorta (Right)

The vorticity contours for the last three phases of a cardiac cycle are shown in Figure 4.12. In Figure 4.12.10a, it is observed that the advancing primary vortex collides with the posterior wall. Subsequently, the primary vortex is torn and divided into two main vortices. These two vortices then diffuse and enlarge. To conserve the angular momentum, vorticity magnitude decreases with increasing size. After the collision with the posterior wall, the counter-rotating secondary vortex is sucked into the outlet. Although a portion of the primary vortex is also sucked into the outlet, the remaining vorticity region travels to the low velocity recirculation region. Viscous friction with the irrotational fluid volume and losing some portion of the vortex to the outlet are the reasons behind the decay in vorticity. Additionally, relatively weak vortical structures continue to be produced at the inlet. These structures detach from the wall and weaken due to viscous friction and diffusion during their migration.

In Figures 4.12.10b & 11b, the viscous boundary layer around healthy aorta walls becomes very clear. In Figure 11b, the strength of the boundary layer peaks and starts to weaken with the following phases. The strong vorticity region near the vessel outlet also enlarges until the last phase of the cardiac cycle.

Although there are vortical structures in both geometries, the strength of these vortices differs significantly. While the peak vorticity value encountered in the aneurysm geometry is approximately 30 s^{-1}, the peak value of vorticity in the healthy aorta is nearly 12 s^{-1}. Another critical point is the residence time of the vortices with maximum vorticity inside the vessels. The vorticity contours show that the maximum vorticity is present in five phases for both geometries. This means the vortices with peak vorticity reside in the vessel for half of the total cardiac cycle duration. Therefore, the value of the maximum vorticity might significantly impact the velocity field inside an arterial vessel.

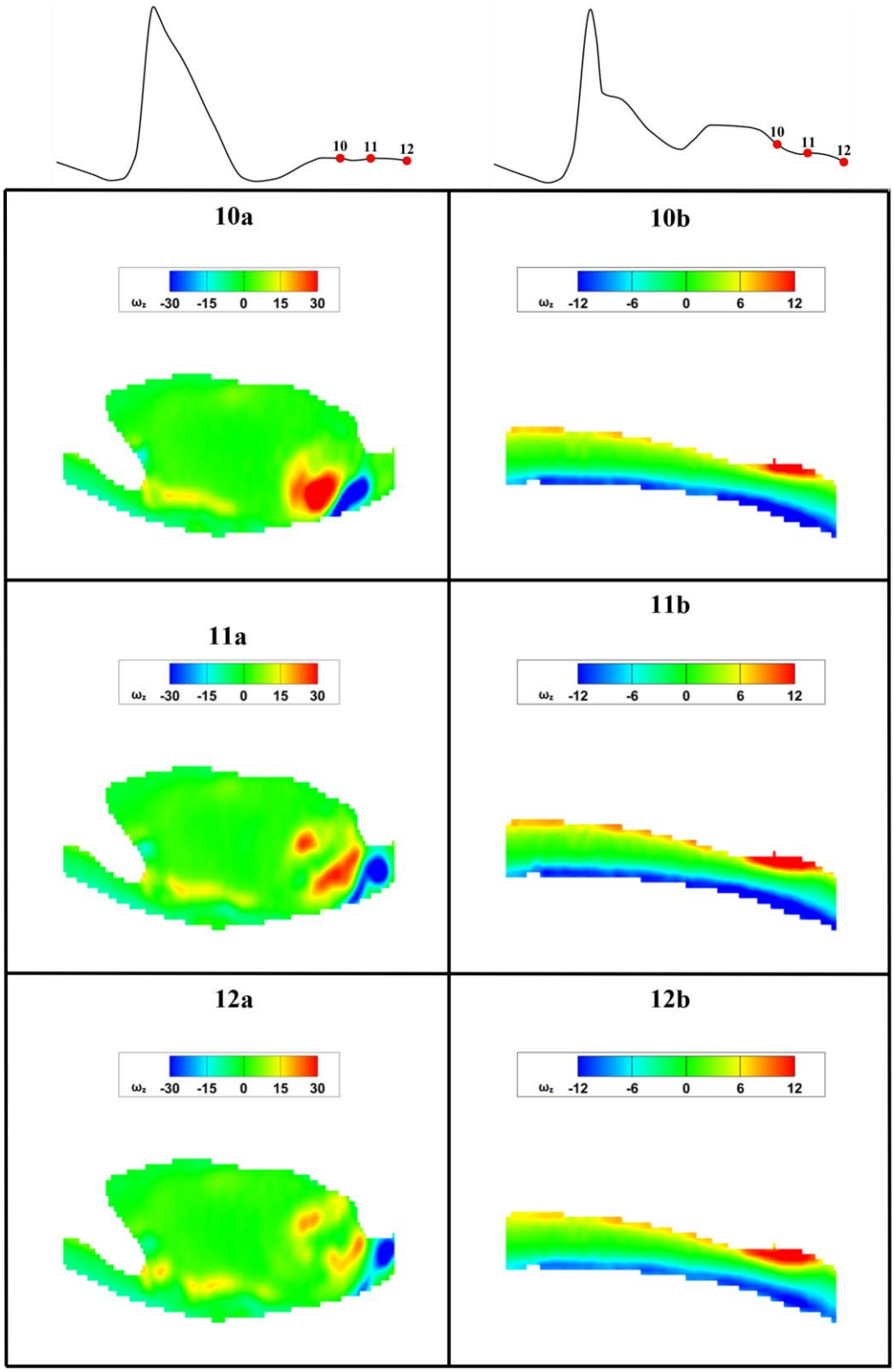

Figure 4.12. Vorticity contours for the last three phases of the cardiac cycle. AAA (Left), healthy aorta (Right).

4.4 Swirling Strength (λ_{ci})

Swirling strength is one of the discussed vortex identification methods in Section 2.5 Vortex Identification Methods. An above-zero value for the swirling strength indicates a vortex core inside the flow domain. This study selected the threshold as zero to capture all the vortical structures in the arterial vessels. A desired threshold other than zero can also be applied to eliminate the weak vortices. Another aspect to consider is the value of swirling strength. Larger values of swirling strength represent relatively stronger vortex cores. This section will discuss the swirling strength contours for the aneurysm and healthy aorta model and compare results with the vorticity contours.

Swirling strength contours for the first three phases of the cardiac cycle for both geometries are shown in Figure 4.13. Figure 4.13.1a highlights the secondary vortical structure and the torn primary vortex near the aneurysm outlet. These structures are formed by the collision of the primary vortex with the posterior wall. The swirling strength indicator also reveals a weak vorticity region inside the aneurysm sac. This region is near the expanding part of the anterior wall and is formed by the diffusion of torn vortices inside the aneurysm sac. In Figure 4.13.1a, small-scaled vortices detached from the inlet and the vortex core inside the aneurysm outlet are also noteworthy. These structures are also visible in the vorticity contours.

In the following phases, secondary vortices rotate inside the recirculation region following a counter-clockwise direction. This trend can be seen in Figures 4.13.2a & 3a. The counter-clockwise rotation is related to the velocity field inside the recirculation region. The counter-clockwise rotating streamline structures are visible in Figure 4.6.1a. During their rotation, secondary vortices weaken due to friction with the irrotational fluid around them and diffusion of the vortex core.

In Figure 4.13.1b, the first detail to notice is the vortex core adjacent to the upper wall near the vessel outlet. Another relatively weaker vortex core is apparent at the vessel outlet. The strong vortex core at the upper wall decays with the decreasing flow rate in the following phases. The weaker vortex at the outlet keeps its strength throughout phases 1, 2, and 3. The swirling strength criterion also captures the weak boundary layer adjacent to the lower wall.

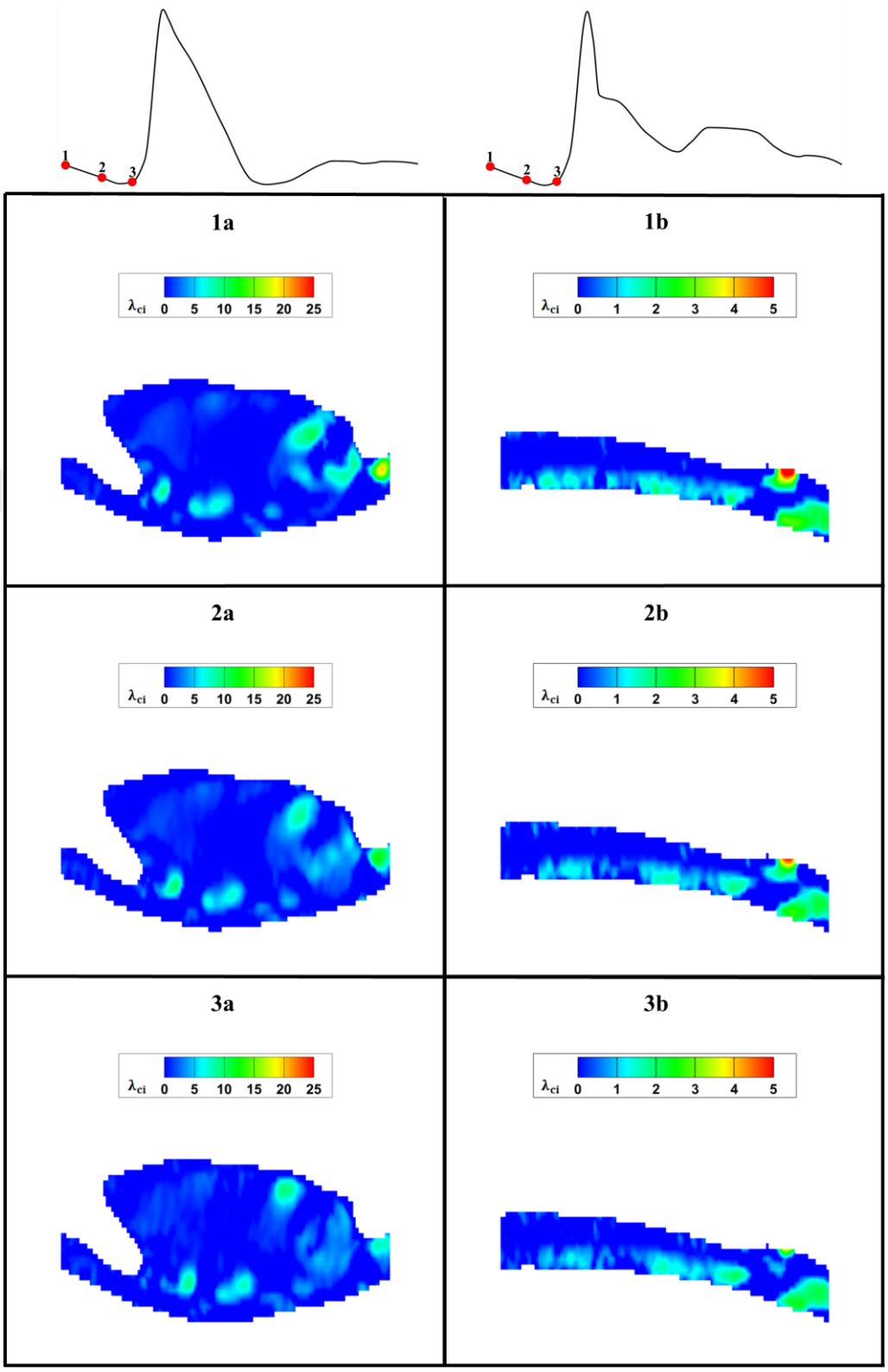

Figure 4.13. Swirling strength contours for the first three phases of the cardiac cycle. AAA (Left), healthy aorta (Right)

Figure 4.14 shows the swirling strength contours for phases 4,5 and 6. In Figures 4.14.4a, 5a & 6a, the complete decay and diffusion of one portion of the torn primary vortices is apparent. The remaining vortex keeps rotating counter-clockwise inside the recirculation region. It gets closer to a collision with the anterior wall. The migration of the previously produced small scaled vortices from the inlet is also apparent. They follow the jet flow and translate toward the outlet. The significance of these phases is the production of the primary vortex. Figure 4.14.5a shows the first instance that the primary vortex is fully visible and about to detach from the aneurysm wall. Swirling strength and vorticity strength methods capture the primary vortex at the same phase, indicating parallelism between these two methods. In Figure 4.14.6a, the detachment and translation of the primary vortex can also be seen. Another aspect of this phase is the complete decay of diffused, weak vortical region present in the previous phases near the outlet. The weak vortical region near the aneurysm outlet in Figure 4.14.4a is not evident in Figure 4.14.6a. The outlet sucks this region and creates a large irrotational region near the outlet.

Figures 4.14.4b,5b & 6b show the vortical structures captured in the healthy aorta. These figures also highlight a vortex core at the outlet of the healthy aorta. This vortex core leaves the aorta vessel in 6th phase. The boundary layer captured in the previous phases also gets stronger and gets into a more continuous shape in the 4th, 5th, and 6th phases.

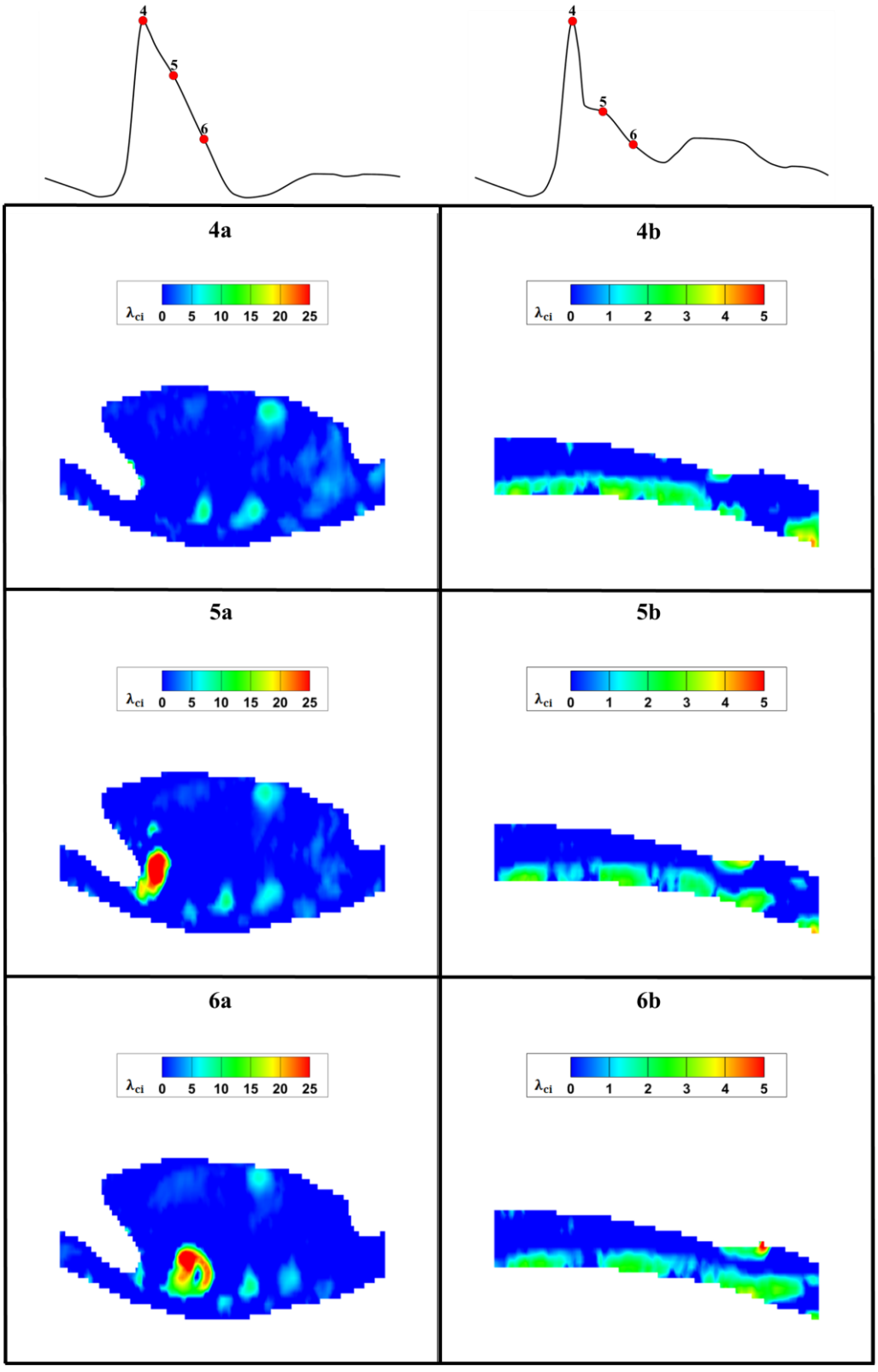

Figure 4.14. Swirling strength contours for the deceleration phase of the cardiac cycle. AAA (Left), healthy aorta (Right)

Figures 4.15.7a,8a & 9a present the translation of the strong primary vortex in the aneurysm. It gets closer to the posterior wall and produces an additional secondary vortex in the 9th phase. The vorticity contour (Figure 4.11.9a) also captures this vortex. Additionally, from the vorticity contour, it can be seen that it is a counter-rotating vortex relative to the primary vortex. Besides migration of the primary vortex, Figures 7a, 8a, and 9a also show the collision between the torn primary vortex in the aneurysm sac and the anterior wall. As a result of this collision, the torn vortex reflects and loses most of its strength. The remaining vortex core diffuses the rest of its vorticity to the irrotational flow around it and decays completely.

The swirling strength contours in the 7th, 8th, and 9th phases for the healthy aorta can be observed in Figures 4.15.7b,8b & 9b. The general trend evident in these phases is the thickening of the shear layer adjacent to the lower wall of the aorta. Furthermore, a large vortex covers most of the vessel outlet. This detected vortex is formed with the shear layer detachment from the lower wall in the previous phases. The curvature of the healthy aorta near the outlet causes this flow separation. Although flow separates and forms a vortical structure, the strength of this vorticity is minor compared to the swirling strength values seen in the aneurysm.

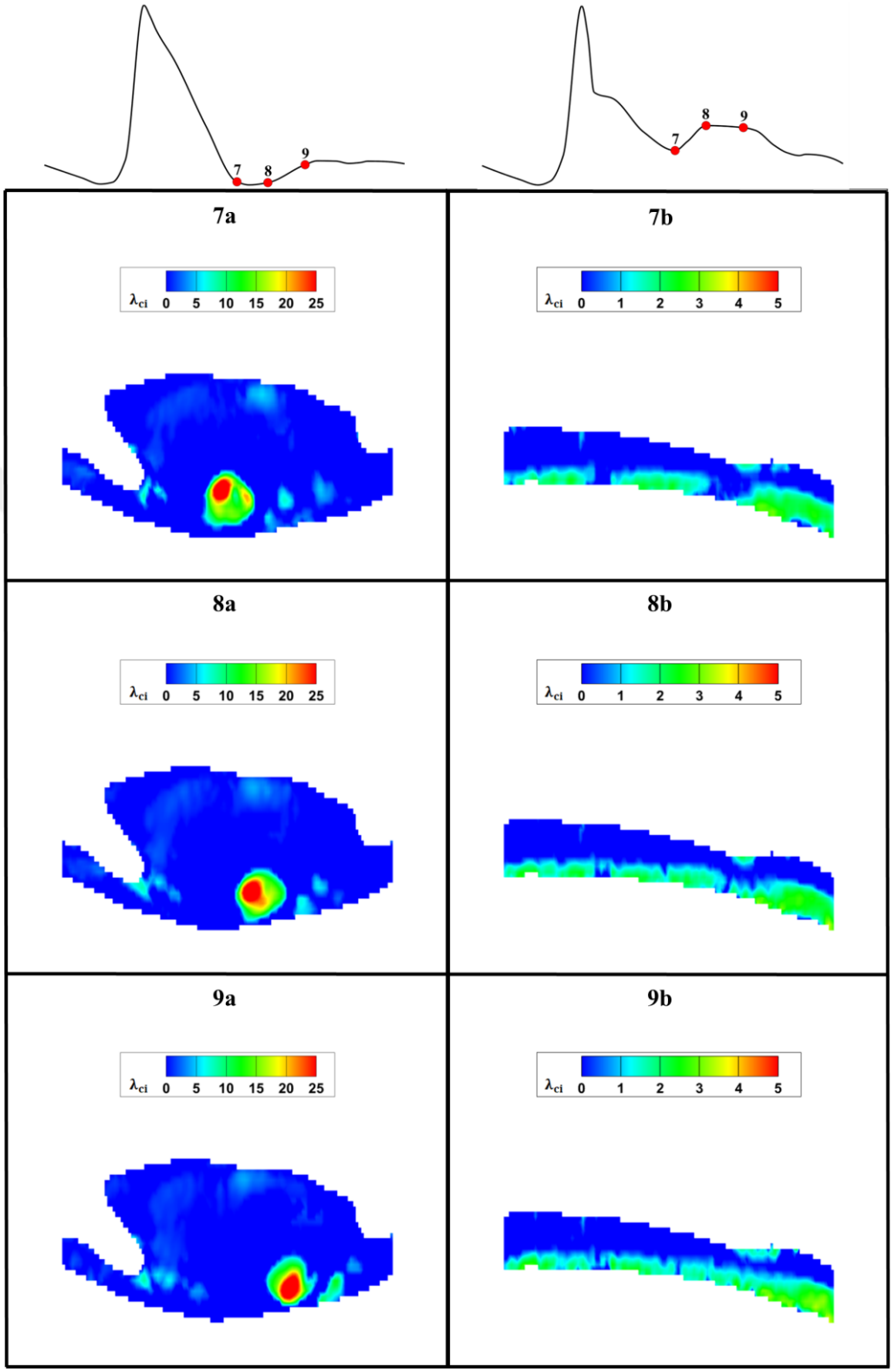

Figure 4.15. Swirling strength contours for the post deceleration phases of the cardiac cycle. AAA (Left), healthy aorta (Right)

The swirling strength contours for the last four phases of the cardiac cycle are shown in Figure 4.16. Figures 4.16.10a, 11a & 12a present the swirling strength contours for the aneurysm model. According to Figure 4.16.10a, the primary vortex converges to the posterior wall with its counter-rotating partner. Moreover, relatively weak vortices continue to be produced from the inlet. Figures 4.16.11a & 12a show the collision and reflection of the primary and secondary vortex pair. After the collision, the primary vortex is divided into two. Subsequently, these two vortices enlarge and weaken. Besides the divided primary vortex, the counter-rotating pair is sucked into the outlet. These findings are also parallel with the vorticity magnitude contours.

The 10th phase is the first instance that the strongest vortex present in the healthy aorta is produced. The produced vortex can be seen in Figure 4.16.10b. In the healthy aorta, the vortex core adjacent to the upper wall gets stronger until the end of the cardiac cycle. Some portion of the continuous shear layer near the lower wall detaches and forms a standalone vortex core at the lower wall. This phenomenon can be seen in Figures 4.16.11b & 12b. Please note that this standalone vortex is identical to the vortical structure, which left the aorta vessel in the 4th phase.

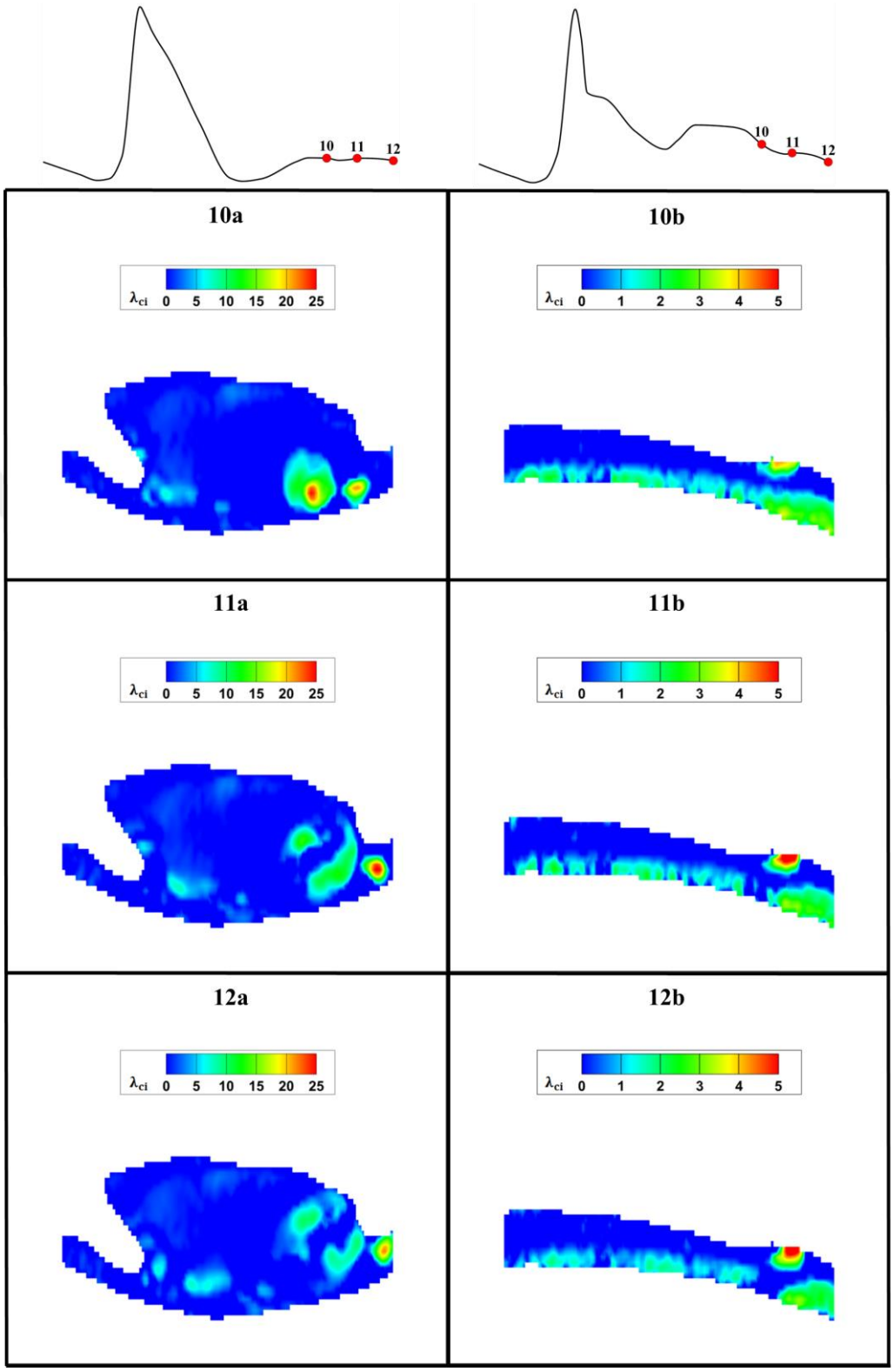

Figure 4.16. Swirling strength contours for the last three phases of the cardiac cycle. AAA (Left), healthy aorta (Right)

In conclusion, swirling strength contours show the vortices' diffusion and decay characteristics better than vorticity contours. Moreover, the swirling strength makes the weak vorticity regions in the recirculation area significantly more visible. An additional comment should be made about the strengths of vortices in the healthy aorta and the aorta with an aneurysm. The results show that the strongest vortex core formed in the healthy aorta is equivalent to the vortices in the aneurysm, which lost most of their vorticity by tearing and reflecting from the walls. The same comment is also valid for the maximum swirling strengths for both geometries. While 25 is the maximum swirling strength for the aneurysm model, this value is just 5 for the healthy aorta. This proves that the flow separations and irregularities in the aneurysm are significantly more severe compared to the healthy aorta model.

Another aspect to mention is visible vortical structures adjacent to the healthy aorta wall. To understand if these structures are vortex cores or just shear layers, Q criterion can be used. In Figure 4.17, Q criterion for selected two phases of the healthy aorta can be seen. When compared with the Figures 4.9.2b & 4.12.11b, it is apparent that, Q criterion contours highlight significantly less area adjacent to the wall. This comparison also concludes that the vorticity and swirling strength contours can not distinguish the vortex cores from the boundary layers. Instead, Q criterion can be utilized to exclude the boundary layers. Q criterion used with a proper threshold can eliminate the boundary layers. After this elimination, vortex cores are the only structures that are higlighted in the contour.

Final remark should be made about the strengths of the vortex cores in the healthy aorta. Strengths of the formed vortex cores are comparable with the shear layers. For the aneurysm case, formed vortex cores make the strength of the shear layers negligible. Boundary layers in the contours of the aneurysm are invisible resulting from this deviation between the strengths of the vortex cores and shear layers.

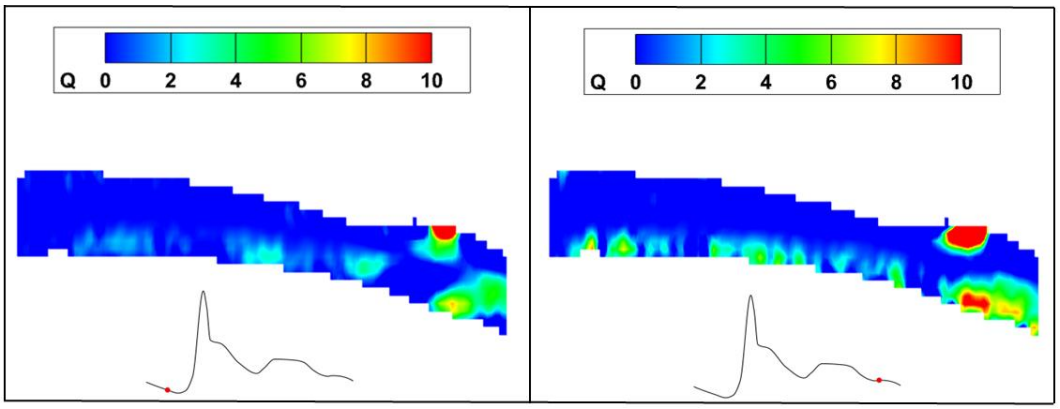

Figure 4.17. Q criterion contours for the selected two phases of the healthy aorta

4.5 WSS Results

Two parameters have a significant effect on the experimental WSS estimations. These parameters are velocity profile fit and initial data point as mentioned in the Section 3.4.2.1 & 3.4.2.2. Two validation methods are used to decide which velocity profile and initial data point pair should be used for an accurate WSS estimation. The first method compares experimental WSS results with the analytical solution. Since there is not any analytical WSS solution for an irregular geometry like a patient-specific abdominal aorta, the analytical solution for the Hagen-Poiseuille flow is used for validation purposes. Hagen-Poiseuille flow is the exact analytical solution to Navier-Stokes equations for a laminar flow inside a straight, circular tube. However, the patient-specific abdominal aorta can not be recognized as a circular tube. Therefore the circular inlet portion of the geometry is used for this validation. Furthermore, steady and laminar flow arrangements are used to provide the conditions of the Hagen-Poiseuille flow.

As a result of the Navier-Stokes equation for the laminar flows in the circular tubes, the below velocity profile is obtained (Gerhart et al., 2017). Note that the velocity profile is a function of the r, radial position within the tube.

$$u(r) = u_{max}\left[1 - \left(\frac{r}{R}\right)^2\right] \quad (4.1)$$

Where:

u_{max} is the maximum velocity value inside the center of the circular tube

r is the radial position inside the tube

R is radius of the circular tube

The derivative of this velocity profile with respect to the radial direction, r, should be taken to calculate the WSS in the cylindrical tube wall. The derivative of this velocity profile should be taken with respect to r, since it is the wall normal direction. Taking the derivative

$$\frac{du(r)}{dr} = -\frac{2\,u_{max}r}{R^2} \quad (4.2)$$

Using Equation 4.2, WSS becomes

$$\tau_w|_{r=R} = \frac{-2\,\mu\,u_{max}}{R} \quad (4.3)$$

To compare the experimental results with the analytical solution, Equation 4.3 is used. The deviation of the experimental WSS results from the analytical solution is tabulated in Table 4.1.

Table 4.1. Deviation of the experimental data from the analytic solution.

Velocity Profile Fit \ Initial Data Point	1st	2nd	3rd	4th	5th
Linear	213%	**-3.07%**	-30.3%	-36.6%	-40.1%
Second Order Polynomial	308%	36.1%	-15.0%	-24.9%	-25.8%
Third Order Polynomial	368%	72.9%	**-2.94%**	-23.5%	-30.7%
Cubic Spline Piecewise Polynomial	388%	82.8%	**0.27%**	-22.3%	-32.1%

As can be observed from Table 4.1 , the use of the first data for the experimental WSS estimation overshoots the analytical solution extremely. This conclusion is prevailing for all velocity profile fit types. This result was also apparent in Figure 3.21. Using the first PIV data as the initial point caused high velocity gradients also within the healthy aorta. The experimental WSS estimation decreases as the initial data point moves away from the aorta wall. Moreover, the fourth and fifth initial data points undershoot the WSS for all velocity profile fits. This also shows parallelism with Figure 3.21.

From Table 4.1, it is evident that three pairs of velocity profile fits and initial data point selections are in an acceptable error range. These are 2nd data point for the linear velocity profile and 3rd data points for the third-order and cubic spline polynomial velocity profiles. The remaining velocity profile and initial data point pairs that show extreme deviation from the analytical solution are eliminated from the analysis. The WSS results for the whole aorta wall are analyzed to decide which pair to use. As discussed in the Section 2.8, PIV has a tendency to underestimate the WSS values. It may lose track of the high velocity particles inside the grid, and that causes a bias to low velocity gradients. From Figure 4.18, the comparison between the selected three velocity profile and initial data point pairs for the healthy aorta can

be seen. Please note that the data on the figure are taken from the last phase of the cardiac cycle, but the same trend is observed for the whole cardiac cycle

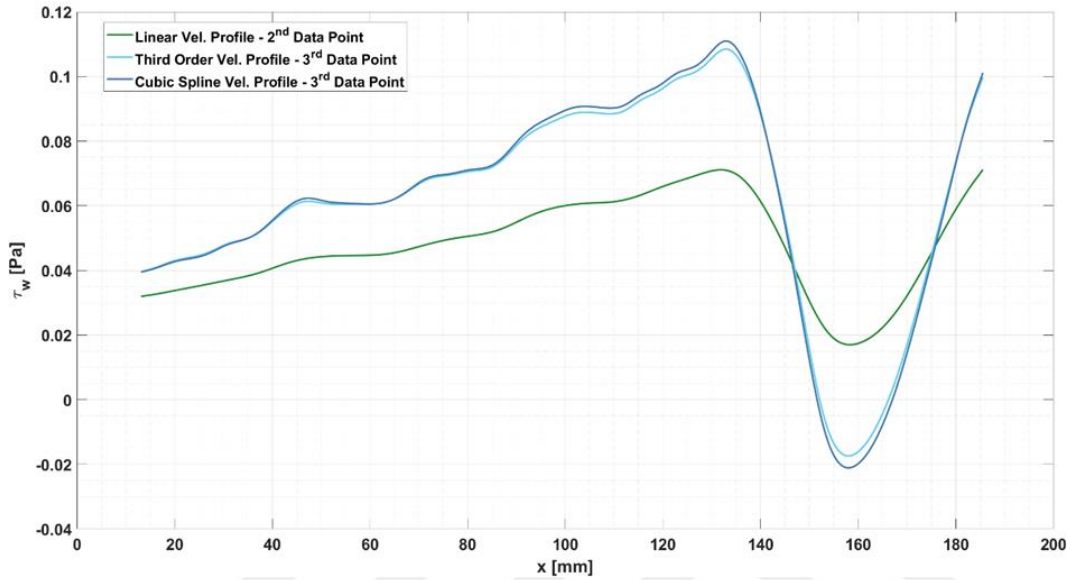

Figure 4.18. WSS value comparison for the three pairs of velocity profile - initial data point selection.

Figure 4.18 compares the whole field WSS results for the specified velocity profile and initial data point pairs. From the figure, it is evident that the WSS results of the third-order polynomial and cubic spline velocity profiles are significantly close. Although these two velocity profiles result in larger magnitudes of WSS, the linear velocity profile is not able to capture the peaks of WSS as successful as the remaining two profiles. Due to PIV's tendency to underestimate velocity gradients, larger magnitudes of the measured WSSs are assumed to be correct. For that reason cubic spline velocity profile with 3rd data as the initial point is selected for further WSS analysis.

4.5.1 Whole Field WSS Results for the Healthy Aorta

This section presents the whole field WSS results for the healthy aorta. These whole field results are obtained using the cubic spline velocity profile with the 3rd data as the initial data point. Note that the entire 12 phases are not presented in this section, but instead, particular phases with significant WSS patterns are included.

Please note that since 2D PIV is used to measure the velocity field, there are two wall portions as upper and lower walls. These wall portions encircle to form the abdominal aorta. Additionally, the swirling strength contour is added to the figures to explain WSS distribution better with the help of flow dynamics inside the healthy abdominal aorta.

Figure 4.19 shows the WSS distribution for the upper and lower walls of the healthy aorta. Please note that the letters used in the images represent “Top (T)” and “Bottom (B)” wall portions. This distribution is obtained from an earlier phase of the cardiac cycle, with the flow rate approximately at the lowest value of a cardiac cycle. In this phase, the most significant aspect is the low magnitudes of WSS. This is due to low velocity magnitudes in the current phase. Another aspect of Figure 4.19.T is the decrease in the WSS near the outlet. The vortical structure that caused this phenomenon is also apparent in the outlet portion of the swirling strength contour. The flow separation due to minor expansion in the upper wall leads to near zero WSS magnitude. The increasing trend of the WSS values until nearly 130 mm can be explained by the geometrical structure of the aorta. The decrease in the cross-sectional area enhances flow attachment to the aorta wall. The reduction in the cross-sectional area and the enhanced flow attachment cause an increase in the WSS values. The WSS values of the lower wall are rather monotonous compared to the upper wall. The WSS values are near zero in most of the lower wall. This is also the result of the near-zero velocities in the analyzed phase.

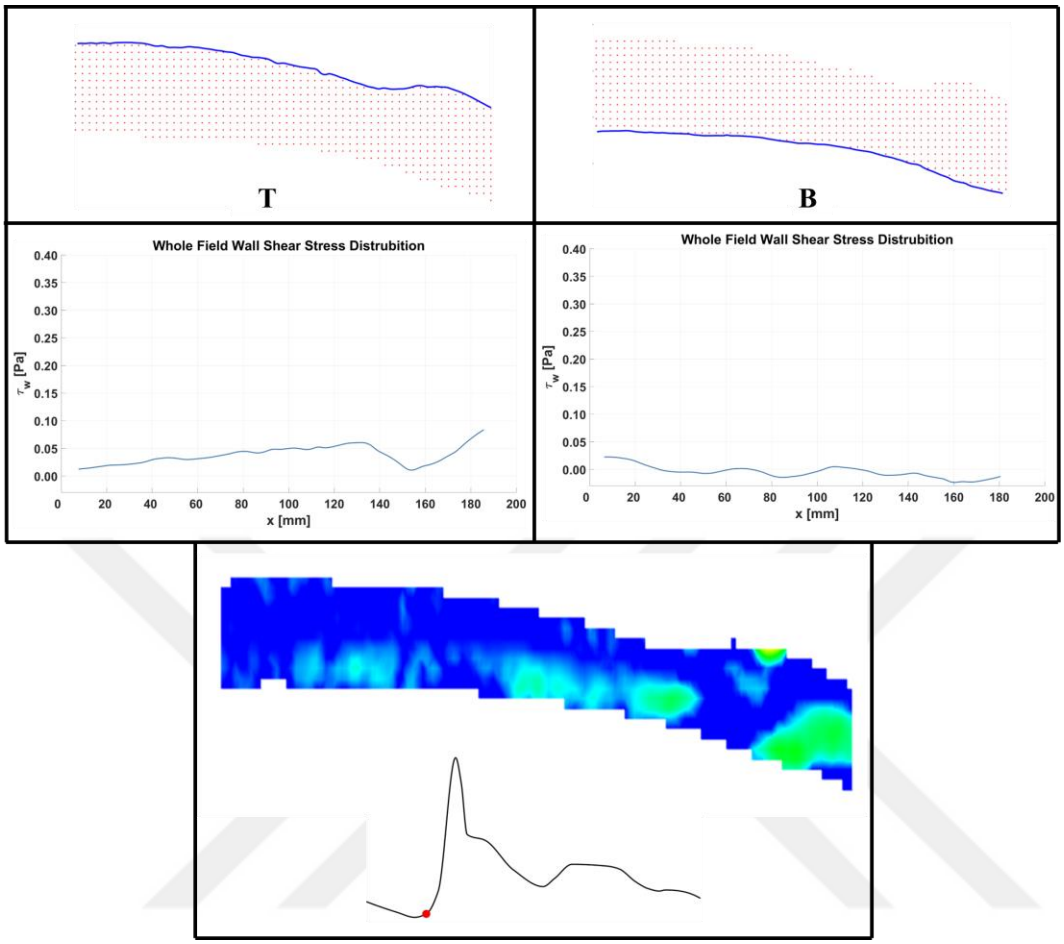

Figure 4.19. WSS distribution in the healthy aorta for one of the earlier phases in the cardiac cycle.

Figure 4.20 presents the WSS distribution in the peak flow rate. With the peak flow rate, WSS values also increased for both lower and upper walls. Figure 4.20.T shows the WSS distribution in the upper wall. Compared to Figure 4.19, it is observed that the WSS values increased significantly. Additionally, the V shape near the outlet becomes more apparent in this phase. This again results from the separation at the expansion portion. It is observed that the peak WSS value is near 0.35 Pa for the upper wall.

Figure 4.20.B, shows the WSS distribution in the lower wall. WSS values for the lower wall are around 0.30 Pa until the outlet portion. At the outlet, WSS values show a decreasing trend. The reason behind the decreasing trend can be observed in the swirling strength contour. The contour plot shows a vortical structure at the outlet portion. This structure induces a decrease in the WSS values near the aorta outlet.

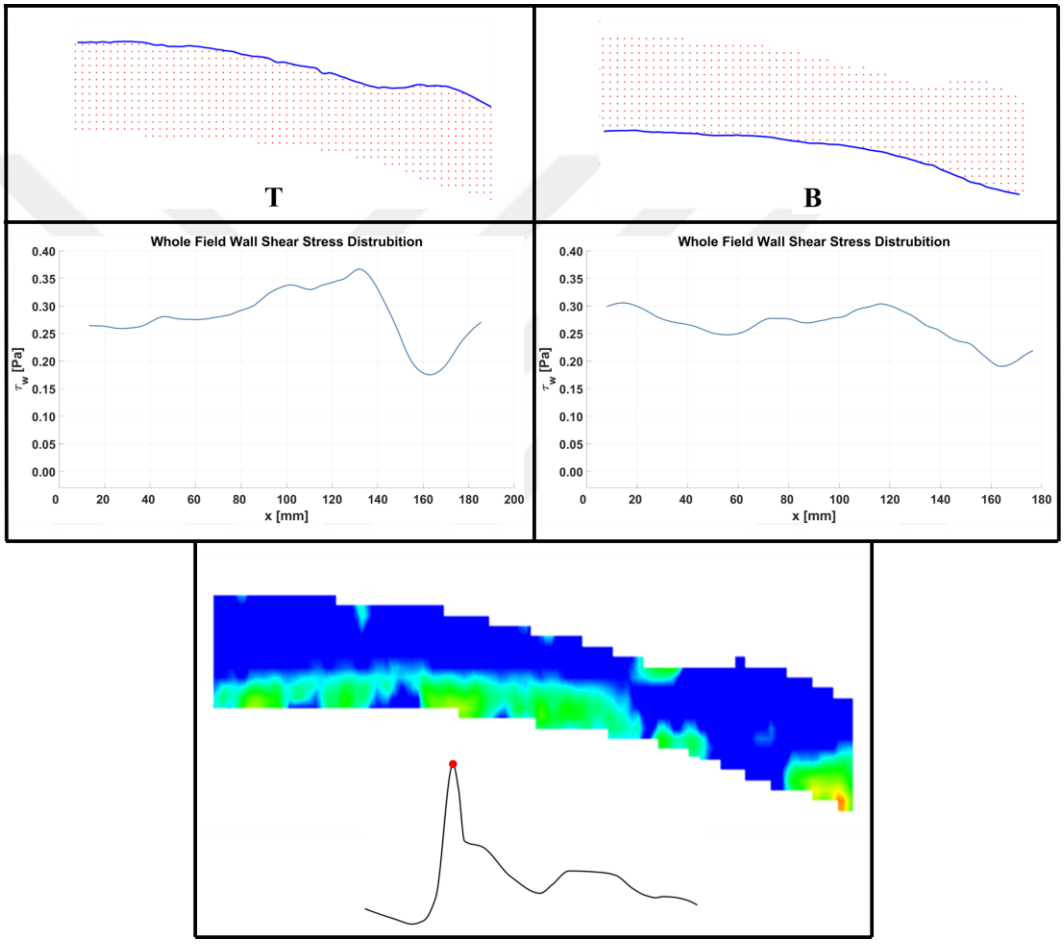

Figure 4.20. WSS distribution in the healthy aorta for the peak flow rate in the cardiac cycle.

Figure 4.21 displays the WSS distribution in the healthy aorta after the steep deceleration. In the upper wall, the effect of the vortical structure apparent in the swling strength contour can be seen in the WSS plot. The weak vortical structure formed with deceleration causes a minor decrease in the WSS values. The diminish in the overall WSS values compared to the phase with the peak flow rate should also be highlighted. WSS magnitudes are directly affected from the instant of the cardiac cycle.

Figure 4.21.B, again, follows a similar trend to Figure 4.20.B. Although the trend throughout the lower wall is similar, the decrease in the WSS values between these two phases should also be emphasized. The separation region near the outlet causes low velocity values adjacent to the lower wall and causes a visible decrease in the WSS magnitudes.

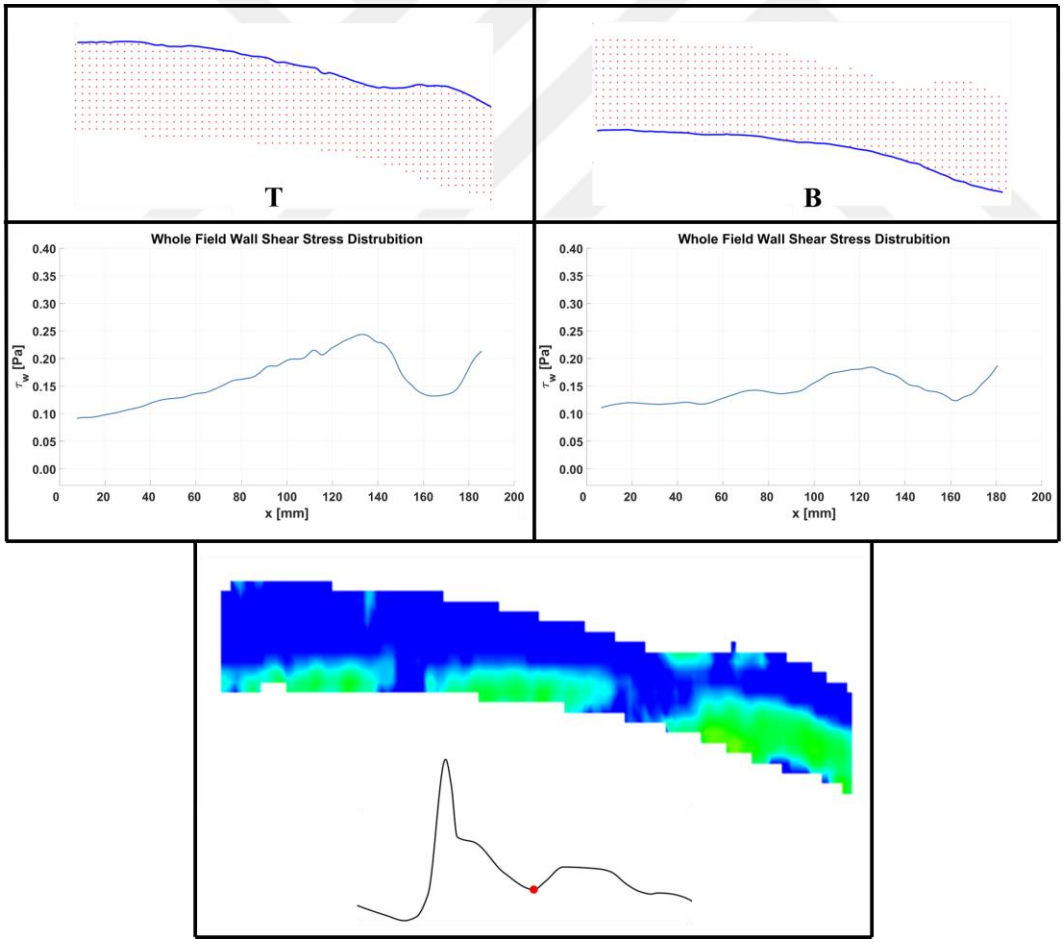

Figure 4.21. WSS distribution in the healthy aorta for the post deceleration phase in the cardiac cycle

The WSS value distribution for the upper wall near the end of the cardiac cycle can be seen in Figure 4.22.T. The swirling strength contour indicates a relatively strong vortical structure adjacent to the upper wall. As a result of this stronger structure, the V shape at the WSS plot near the outlet deepens and gets close to zero. Zero WSS near the wall implies a flow separation. Near the end of the cardiac cycle, a flow separation is observed with the effect of the natural geometrical structure of the abdominal aorta.

Figure 4.22.B is similar to the WSS results of the previous phase, both magnitudes, and trend-wise. The phase presented in Figure 4.22.B differs from Figure 4.21.B with the stronger vortical region near the outlet. The stronger vortical region causes more decrease in the WSS values compared to the previously presented phase. The stronger diminishing in the WSS, results in near-zero WSS values near the outlet.

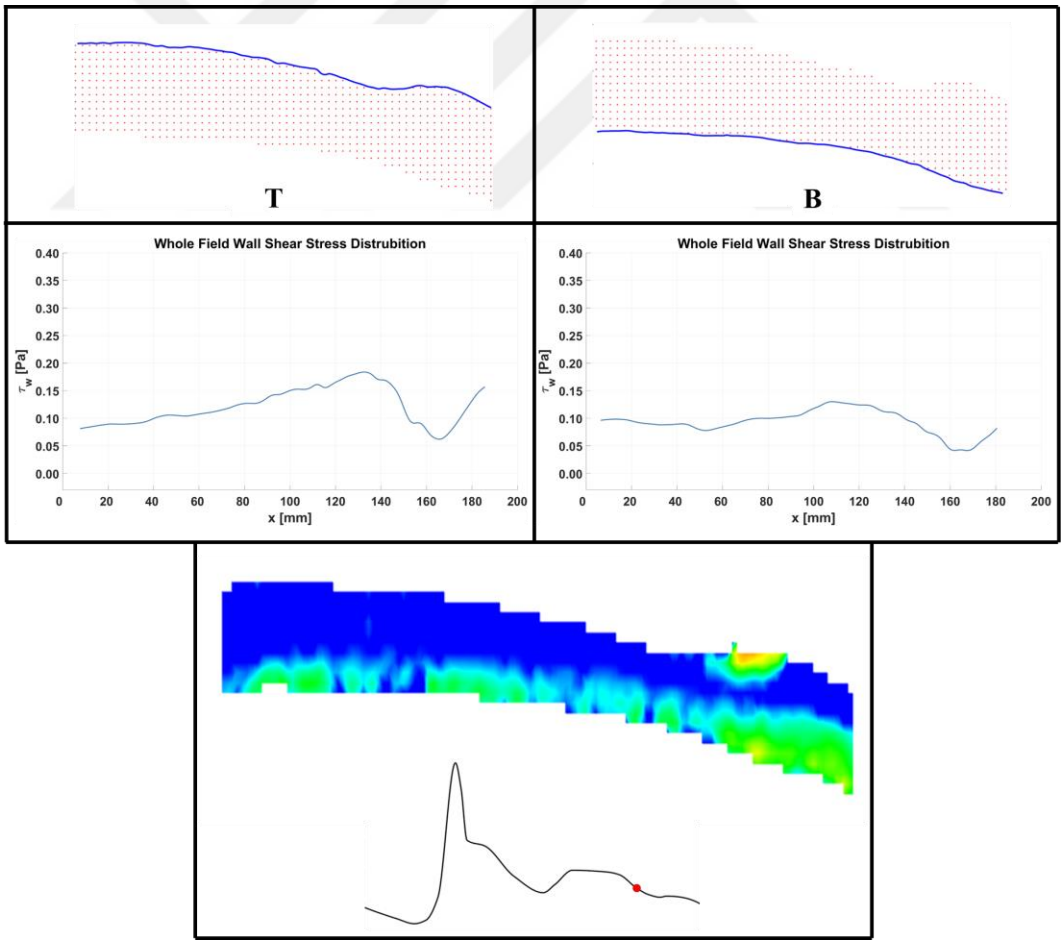

Figure 4.22. WSS distribution in the healthy aorta for one of the near-end phases of the cardiac cycle.

WSS results for the last cardiac cycle phase are presented in Figures 4.23.T & B. The first aspect of this phase to consider is the strong swirling strength area adjacent to the upper wall. With the last phase, the swirling strength is maximized. The peak in the swirling strength also has consequences in the WSS field of the aorta. Besides the overall WSS values at the upper wall, the minimum WSS value also goes below zero. The V shape near the outlet becomes more visible with the strengthening of the vortex near the outlet. The strength of the vortex creates a steep decline in the WSS field.

The separation and concentration of the previously continuous vortical region can be seen in the swirling strength contour. When the WSS plots are investigated, it is observed that due to low flow rates in the last phase, WSS magnitudes at the lower wall get closer to zero. Additionally, the concentrated vortical region near the outlet decreases the WSS values and gets these values below zero.

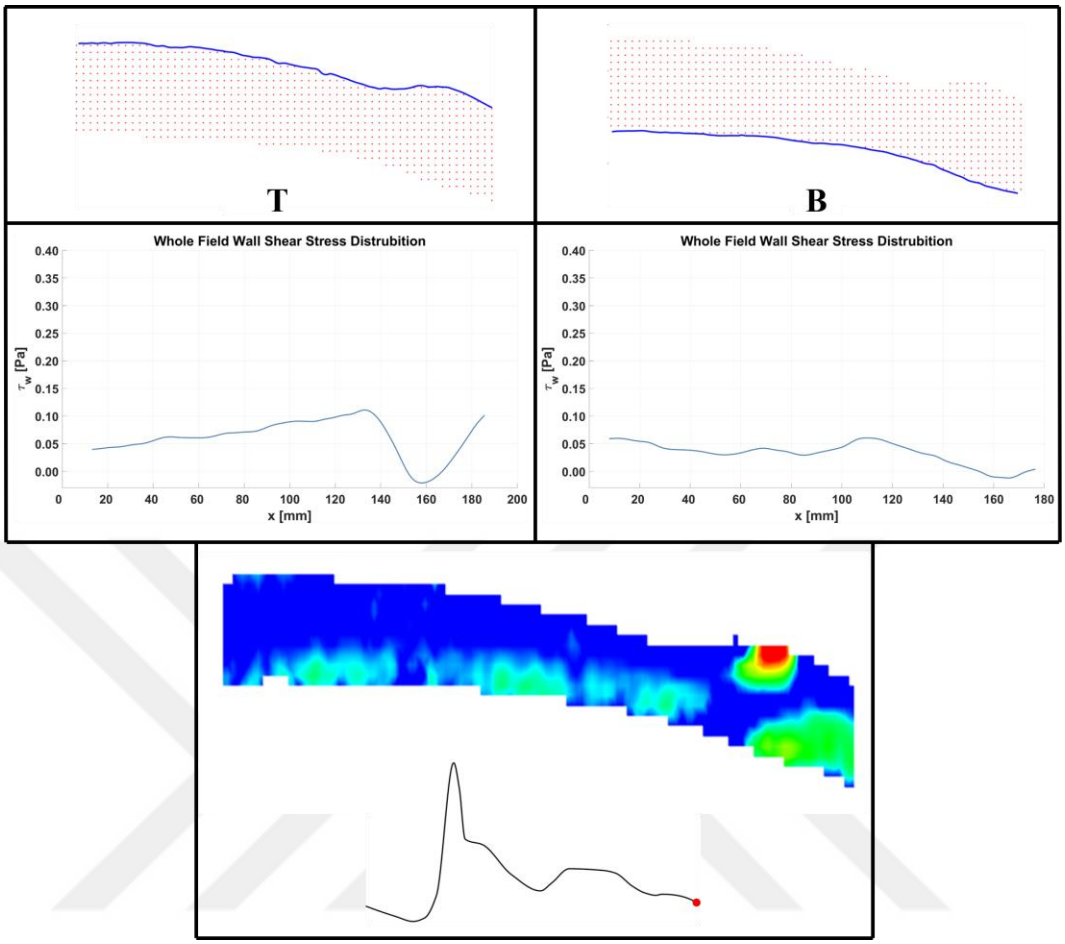

Figure 4.23. WSS distribution in the healthy aorta for the last phase of the cardiac cycle

4.5.2 WSS Parameters

WSS parameters can be more helpful in understanding aneurysm development and flow mechanics occurring in the abdominal aorta instead of WSS distribution in the aorta wall. The WSS parameters calculated for both a healthy abdominal aorta and an abdominal aortic aneurysm will be compared in this section. The WSS parameters that will be compared in this section are the Time Averaged Wall Shear Stress (TAWSS), Oscillatory Shear Index (OSI), and Endothelial Cell Activation Potential (ECAP). The aneurysm model examined in one of the previous studies in the Fluid Mechanics Laboratuary is used for WSS parameter comparison purposes (Fathipour, 2022). To better understand the WSS parameter distribution in the vessel walls, the aneurysm model used in the parameter comparisons is presented in Figure 4.24. Only the lower wall is used for the parameter analysis since it is the portion of the expanded region of the aneurysm.

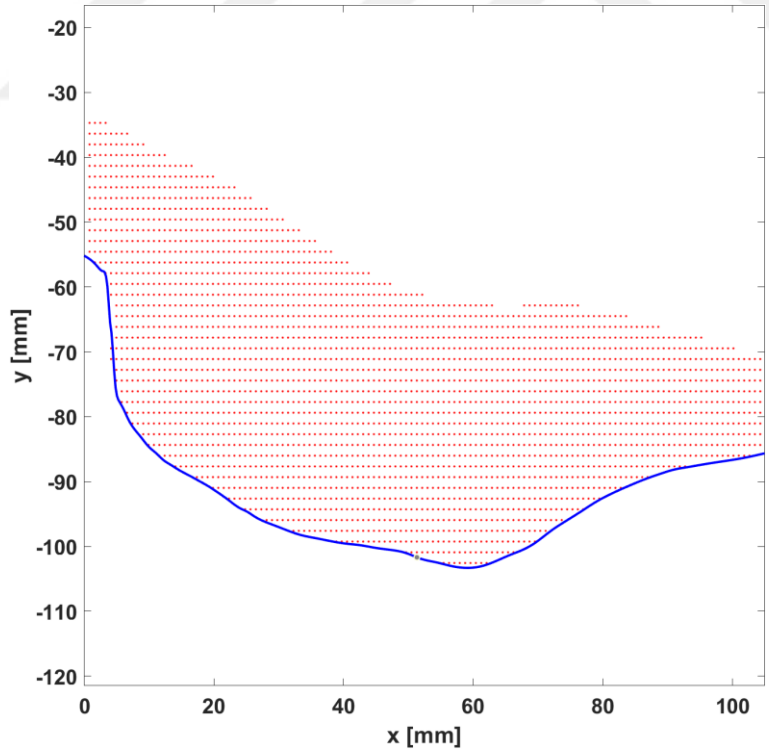

Figure 4.24. Aneurysm model used for WSS parameter comparisons with the healthy aorta

4.5.2.1 TAWSS

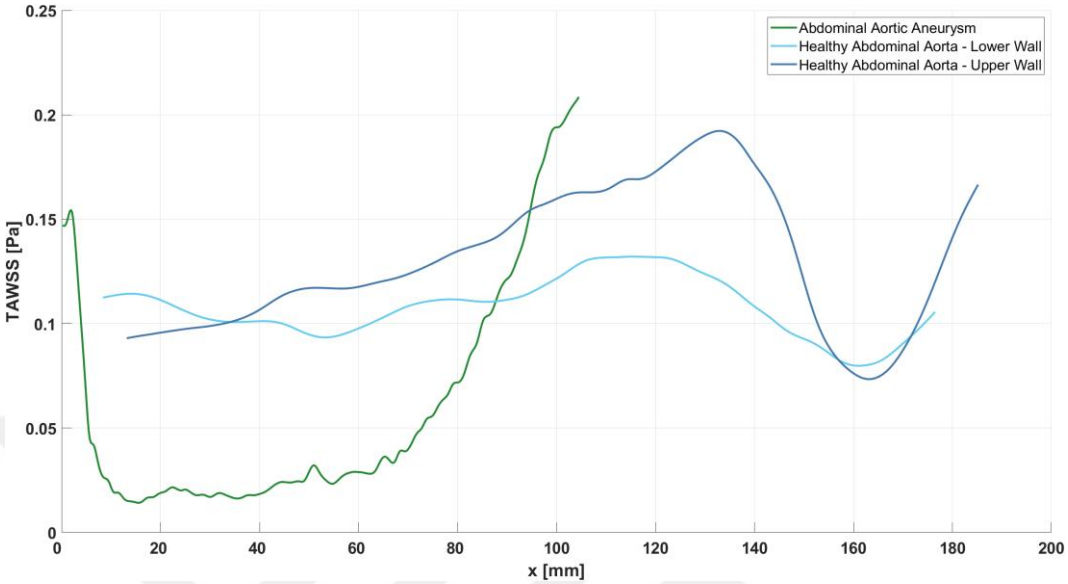

Figure 4.25. Comparison of TAWSS values for the healthy aorta and AAA

The TAWSS results for both walls of the healthy aorta and the expanded wall of the aneurysm can be observed in Figure 4.25. As mentioned in Section 2.7.1, TAWSS is the average WSS value exerted on the aneurysm wall during a complete cardiac cycle. Please note that the line plot's extent for the healthy abdominal aorta is larger than the aortic aneurysm. This results from the dimensions of both vessels. While the length of the healthy aorta is nearly 18 cm, the analyzed portion of the aneurysm is almost 10 cm. Although the size of the observed areas differs, the WSS parameters calculated in the flow domains still indicate clear deviations.

The first point to highlight is the magnitude-wise TAWSS deviation between the healthy aorta and the aneurysm. When Figure 4.25 is examined, an abrupt decrease after the inlet portion and near-zero TAWSS values between 10 and 70 mm can be observed for the aneurysm. With the inspection of the Figure 4.24, it is seen that the aneurysm sac lies between this interval. Near-zero TAWSS values imply the presence of a large separation region in the aneurysm sac. A significant increase in

the TAWSS is apparent at the end of the near-zero values. This region is where the aneurysm sac starts to narrow. The steep increase in the TAWSS values also indicates a flow reattachment zone. With the impingement of the flow to the aneurysm wall, shear stress exerted on the aneurysm wall is exposed to a steep increase.

TAWSS values for the healthy aorta follow a more monotonous trend compared to the aneurysm model. TAWSS slightly increases throughout the healthy aorta due to the geometrical structure of the vessel. Although TAWSS steeply decreases near the aorta outlet, the overall TAWSS is still considerably higher compared to the aneurysm model. This signifies the absence of flow separations in the aorta. As mentioned in the previous section, the decrease in TAWSS near the outlet resulted from the minor expansion.

4.5.2.2 OSI

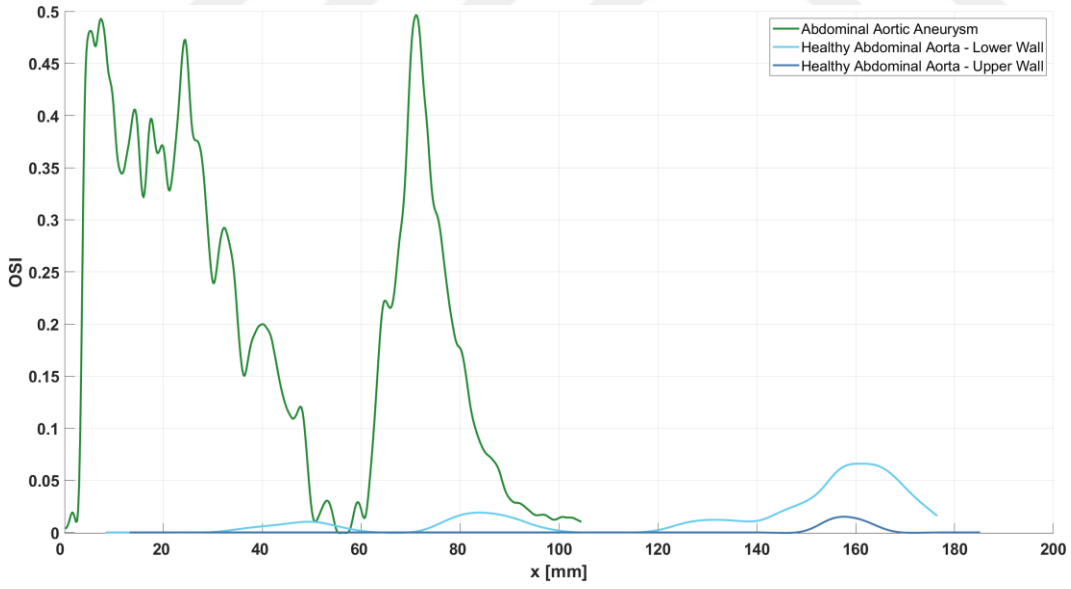

Figure 4.26. Comparison of OSI values for the healthy aorta and AAA

When OSI distributions for the healthy aorta and the aneurysm are compared, the deviation between the two models becomes significantly more dramatic. As discussed in Section 2.7.2, OSI indicates the oscillatory characteristic of the WSS exerted on the vessel wall. This oscillatory behavior is the sign change of the WSS during a cardiac cycle.

Figure 4.26 presents the OSI distribution for the healthy aorta and the aneurysm. Please note that the unphysical oscillations seen on the OSI plot for the aneurysm is a consequence of the experimental method used to calculate wall shear stresses. The experimental errors during the measurement of the near wall velocity values and the additional errors resulted from the derivatives and other computations that rely on the velocity measurements are causing these oscillations. As can be observed from the figure clearly, the oscillatory characteristic of the healthy aorta is significantly less compared to the aneurysm. The OSI parameter takes the maximum possible value of 0.5 at two points of the aneurysm wall. When the location of these two points is examined, these points are most probably the flow separation and reattachment points in the aneurysm sac. If the flow patterns around the separation and reattachment zones are studied, sudden flow direction changes around these points can be observed. These sudden direction changes can trigger the formation of large OSI values on the aneurysm wall.

In the healthy aorta case, the absence of the separation and flow reattachment zones results in minor OSI values on the aorta wall. The deviations from the zero OSI are often formed in the areas where the vortical regions are observed during the cardiac cycle. Additionally, measurement errors should be mentioned during the OSI discussion. The swinging between the positive and negative velocity values for the points adjacent to the aorta wall can arise from measurement errors. These swingings can generate non-zero OSI values. Despite these possible measurement errors, the massive deviation between healthy aorta's and aneurysm's OSI values is undeniable.

4.5.2.3 ECAP

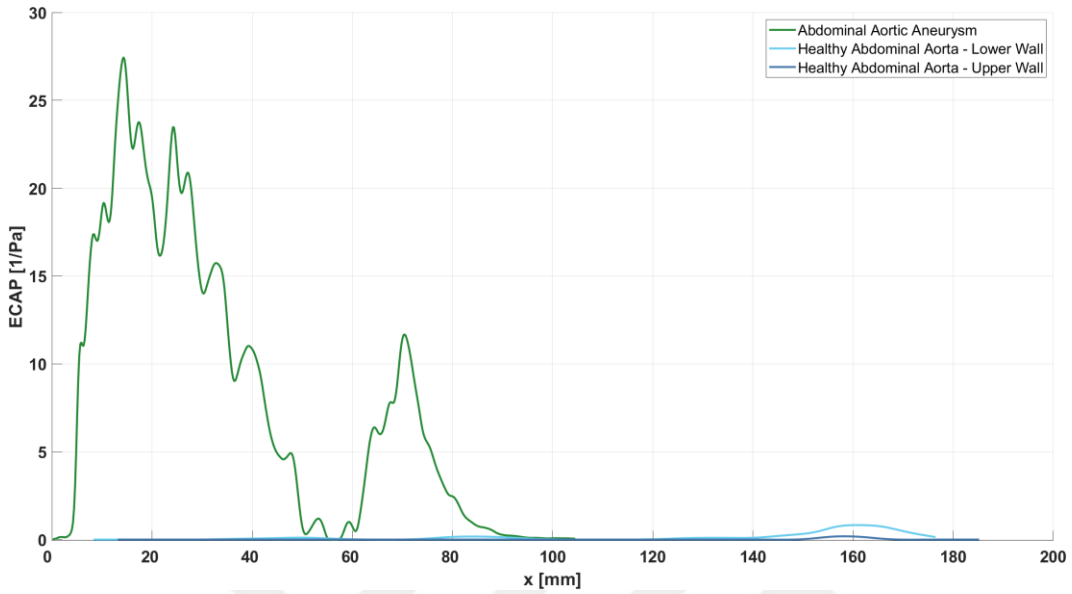

Figure 4.27. Comparison of ECAP values for the healthy aorta and AAA

ECAP is the final parameter that will be discussed. As mentioned in Section 2.7.3, ECAP is a recently developed parameter that describes the blood platelets' potential to hold onto the vessel wall. It may be the most critical parameter for aneurysm studies since ILT formation is seen in most aneurysm patients (Swedenborg & Eriksson, 2006).

In Figure 4.27, a dramatic difference between the ECAP values of the aneurysm and the healthy aorta is apparent. For the aneurysm model, although there are again two peaks at the separation and reattachment zones, the maximum ECAP is much more prominent at the separation zone compared to the second peak at the reattachment zone. The increasing TAWSS values at the reattachment zone are the reason behind relatively low ECAP values.

When the healthy aorta is examined, the ECAP values are insignificant. Only small peaks are observed near the outlet portion. However, these small peaks should not be neglected. The correlation between the higher ECAP numbers and being more

prone to thrombus formation is known from previous studies (Kelsey et al., 2016). These non-zero ECAP regions have the possibility to form ILT. Notably, the healthy aorta's potential to create an ILT layer is low. But if this low possibility comes true over a long period, the case can be pushed to a closed loop, leading to the aneurysm formation. This closed loop can be explained by the studies that examine ILT's effect on the vessel wall. Although ILT is formed as a response to disturbed hemodynamics, many studies show that ILT formation damages the mechanical strength and integrity of the vessel wall (Kazi et al., 2003; Mutlu et al., 2023). In other words, the body's natural response to protect the arterial wall can cause more damage in the long term. The patient is prone to aneurysms when the vessel deterioration due to ILT combines with degradation due to aging. Eventually, while the ECAP values on a healthy aorta seem insignificant compared to an aneurysm, the areas where the ILT formation potential is non-zero can lead to an AAA formation.

CHAPTER 5

CONCLUSION

Abdominal Aortic Aneurysm (AAA) is known to be one of the most fatal diseases. Therefore, understanding the mechanism behind the formation and the rupture of the AAA is of great importance. This study aims to compare the hemodynamics inside the healthy and aneurysmal abdominal aortas and to propose an experimental method that can be used to obtain WSS fields from the patient-specific aneurysm geometries. An experimental setup that can provide a physiological flow pattern to the abdominal aorta models is used to achieve this goal. A 2D-PIV system is embedded in the experimental setup to obtain the velocity field from the selected measurement plane.

With the above-mentioned experimental setup, a 2D velocity field is obtained from the abdominal aorta. Later on, the swirling strength (λ_{ci}) method is applied to observe the formation and migration of vortical structures. This study does not present the remaining vortex identification methods since all methods introduce parallel results. The Q-criterion separates from the rest since it can exclude the boundary layers. The most apparent difference between the healthy abdominal aorta and AAA is the strength of the vortical structures. It is observed that the formed vortices inside the aneurysmal abdominal aorta are much stronger than the healthy aorta. Sudden expansion just after the aorta inlet and the steep deceleration phase in the cardiac cycle result in flow separation. This separation then rolls into a strong vortex inside the AAA. The apparent vortical structures in the healthy aorta are presumably resulted from the natural geometry of the aorta. Although the strength of the vortices existing in the healthy aorta is much weaker compared to the aneurysmal aorta, there are still vortical structures where the abdominal aorta rotates and expands slightly.

Another aspect of this study is obtaining the WSS field from the patient-specific abdominal aortas. These WSS fields are then used in the calculation of the WSS

parameters. These parameters are TAWSS, OSI, and ECAP. These parameters are helping researchers to understand the effect of the WSS on the AAA formation and rupture mechanisms. The calculations show that due to the large low-velocity recirculation region present in the aneurysmal abdominal aorta, TAWSS values are near zero at most of the aneurysm sac. According to a previous study by the Doyle et al. (2014), regions of low WSS are prone to expansion and also rupture without proper precautions. TAWSS in these regions are observed to be below 0.1 Pa, which is also observed in the investigated aneurysm model in this study. These low velocity regions require further attention since Boyd et al. (2015) reported that the WSS values at the rupture zone of an AAA patient is observed to be approximately 0.02 Pa. The aneurysm sac investigated in this study also yields TAWSS values near 0.02 which is a possible rupture indicator. The healthy aorta presents larger TAWSS values since the flow stays attached to the vessel wall. The OSI values are larger for the AAA compared to the healthy aorta. They take the maximum value of 0.5 in two regions of the AAA. These regions are where the flow separates just after the inlet and then reattaches before the outlet. Qiu et al. also observed regions with the maximum OSI in the aneurysm. OSI values of 0.5 are seen in the aneurysm neck where the flow seperates from the aneurysm wall. Again minor OSI regions different than 0 can be observed in the healthy aorta. These are again due to the natural geometry of the aorta. In the areas where the aorta expands slightly, the OSI shows minor deviations from 0. These deviations are also reflected in the ECAP. While the ECAP values reach nearly 30 in the AAA, the healthy aorta deviates from the 0 slightly near the outlet. Although ILT formation potential can be seen as significantly low for the healthy aorta, this potential still can not be neglected. It should be remembered that the low potential can still cause ILT accumulation in these regions throughout human life. ILT accumulation and the resultant modifications in the aorta wall can lead to aneurysm formation and growth.

The final detail of this study that should be mentioned is the difference in flow patterns between the two aorta models. This difference likely results from the increased fluid mass in the aneurysmal abdominal aorta. It should be noted that the

exact same flow pattern is provided from the pump to the experimental setup. However, the flow pattern measurements are taken from the inlet portion of both abdominal aorta geometries, i.e., aneurysmal and healthy abdominal aorta models. Another side note is the obtaining procedure of the flow patterns. Flow rate values from 20 points in the cardiac cycle are used to plot these flow patterns. A polynomial is fitted between these 20 points, and the flow patterns for both geometries are obtained using these polynomials. This deviation can also result from errors during this polynomial fitting procedure.

5.1 Recommendations for the Future Work

Since the viscosity of the glycerol is highly dependent on its temperature, monitoring and controlling the BMF temperature is critical for the experimental accuracy. For that reason, the tank is heated and the BMF temperature is monitored regularly with a precise thermocouple. To control the BMF temperature in a more effective and efficient way, a heat exchanger can be added to the experimental setup.

Another recommendation for future work is a non-Newtonian BMF. It is acknowledged that within the aneurysmal abdominal aorta there exists small regions where the blood exhibits a non-Newtonian characteristic. Although blood behaves as a Newtonian fluid across the majority of the abdominal aorta, the accuracy of the measurements can be enhanced by employing a non-Newtonian BMF. Adding Xanthan gum to the BMF brings the shear thinning characteristics closer to that of human blood. Using non-Newtonian BMF also has a potential to further increase the accuracy of the WSS calculations.

PIV systems equipped with two cameras, i.e., stereoscopic PIV, enable to obtain the third velocity component utilizing multiple 2D measurement planes. While 2D-PIV effectively captures the velocity components in the main flow direction, considering the third velocity component can also add valuable insights to the discussion about

the flow field inside an AAA. Capturing 3D vortical structures experimentally can further help to understand hemodynamics within an aneurysmal aorta.

Experimental WSS calculation method also needs further improvements. Due to measurement errors of the PIV near the wall, the velocity values may contain errors. To decrease the errors induced, regression lines may be used as the velocity profiles replacing profiles those strictly pass from the measured velocity points.

REFERENCES

Aaronson, P. I., T., Ward. J. P., Connolly, M. J. (2013). The Cardiovascular System at a Glance. Wiley-Blackwell.

Asbury, C. L., Ruberti, J. W., Bluth, E. I., & Peattie, R. A. (1995). Experimental investigation of steady flow in rigid models of abdominal aortic aneurysms. Annals of Biomedical Engineering, 23(1), 29–39. https://doi.org/10.1007/bf02368298

Bauer, A., Wegt, S., Bopp, M., Jakirlić, S., Tropea, C., Krafft, A. J., Shokina, N., Hennig, J., Teschner, G., & Egger, H. (2019). Comparison of wall shear stress estimates obtained by laser Doppler velocimetry, magnetic resonance imaging and numerical simulations. Experiments in Fluids, 60(7). https://doi.org/10.1007/s00348-019-2758-6

Bluestein, D., Niu, L. N., Schoephoerster, R. T., & Dewanjee, M. K. (1996). Steady flow in an aneurysm model: correlation between fluid dynamics and blood platelet deposition. Journal of Biomechanical Engineering, 118(3), 280–286. https://doi.org/10.1115/1.2796008

Brindise, M. C., Busse, M. M., & Vlachos, P. P. (2018). Density- and viscosity-matched Newtonian and non-Newtonian blood-analog solutions with PDMS refractive index. Experiments in Fluids, 59(11). https://doi.org/10.1007/s00348-018-2629-6

Budwig, R., Elger, D., Hooper, H., & Slippy, J. (1993). Steady flow in abdominal aortic aneurysm models. Journal of Biomechanical Engineering, 115(4A), 418–423. https://doi.org/10.1115/1.2895506

Centers for Disease Control and Prevention, National Center for Health Statistics. About Multiple Cause of Death, 1999–2019. CDC WONDER Online Database website. Atlanta, GA: Centers for Disease Control and Prevention; 2019. Accessed February 1, 2021

Chen, Q., Zhong, Q., Qi, M., & Wang, X. (2015). Comparison of vortex identification criteria for planar velocity fields in wall turbulence. Physics of Fluids, 27(8). https://doi.org/10.1063/1.4927647

Cleveland Clinic. (n.d.). Aorta.

https://my.clevelandclinic.org/health/articles/17058-aorta-anatomy

Corbett, T. J., Molony, D., Kavanagh, E. G., Grace, P. A., Walsh, M., & McGloughlin, T. M. (2011). Experimental analysis of endovascular treatment of AAA and predictors of long term outcomes. In Studies in mechanobiology, tissue engineering and biomaterials (pp. 247–284). Springer Nature. https://doi.org/10.1007/8415_2011_74

Çengel, Y. A., & Cimbala, J. M. (2006). Fluid Mechanics: Fundamentals and Applications. McGraw-Hill Science/Engineering/Math.

Darwood, R., Earnshaw, J., Turton, G., Shaw, E., Whyman, M. R., Poskitt, K. R., Rodd, C. D., & Heather, B. P. (2012). Twenty-year review of abdominal aortic aneurysm screening in men in the county of Gloucestershire, United Kingdom. Journal of Vascular Surgery, 56(1), 8–13. https://doi.org/10.1016/j.jvs.2011.12.069

Davis, M. A., Harris, M. P., & Earnshaw, J. (2013). Implementation of the National Health Service Abdominal Aortic Aneurysm Screening Program in England. Journal of Vascular Surgery, 57(5), 1440–1445. https://doi.org/10.1016/j.jvs.2012.10.114

Deplano, V., Guivier-Curien, C., & Bertrand, E. (2016). 3D analysis of vortical structures in an abdominal aortic aneurysm by stereoscopic PIV. Experiments in Fluids, 57(11). https://doi.org/10.1007/s00348-016-2263-0

Deplano, V., Knapp, Y., Bailly, L., & Bertrand, E. (2014). Flow of a blood analogue fluid in a compliant abdominal aortic aneurysm model: Experimental modelling. Journal of Biomechanics, 47(6), 1262–1269. https://doi.org/10.1016/j.jbiomech.2014.02.026

Di Achille, P., Tellides, G., Alvarez, F., & Humphrey, J. D. (2014). A haemodynamic predictor of intraluminal thrombus formation in abdominal aortic aneurysms. Proceedings of the Royal Society A: Mathematical, Physical and Engineering Sciences, 470(2172), 20140163. https://doi.org/10.1098/rspa.2014.0163

Doyle, B. J., & Hoskins, P. R. (2017). Aneurysms. In Springer eBooks (pp. 307–329). https://doi.org/10.1007/978-3-319-46407-7_16

Durst, F., Kikura, H., Lekakis, I., Jovanovic, J., & Ye, Q. (1996). Wall shear stress determination from near-wall mean velocity data in turbulent pipe and channel flows. Experiments in Fluids, 20(6), 417–428. https://doi.org/10.1007/bf00189380

Egelhoff, C. J., Budwig, R., Elger, D., Khraishi, T., & Johansen, K. H. (1999). Model studies of the flow in abdominal aortic aneurysms during resting and exercise conditions. Journal of Biomechanics, 32(12), 1319–1329. https://doi.org/10.1016/s0021-9290(99)00134-7

Epps, B. P. (2017). Review of Vortex Identification Methods. https://doi.org/10.2514/6.2017-0989

Fathipour, A. (2022). Experimental investigation of hemodynamics in abdominal aortic aneurysm. METU.

Ferreira, A. G., Egas, A. P. V., Fonseca, I., Costa, A. C., Abreu, D. C., & Lobo, L. (2017). The viscosity of glycerol. The Journal of Chemical Thermodynamics, 113, 162–182. https://doi.org/10.1016/j.jct.2017.05.042

Geoghegan, P., Buchmann, N., Spence, C. J. T., Moore, S., & Jermy, M. (2012). Fabrication of rigid and flexible refractive-index-matched flow phantoms for flow visualisation and optical flow measurements. Experiments in Fluids, 52(5), 1331–1347. https://doi.org/10.1007/s00348-011-1258-0

Gerhart, P. M., Gerhart, A. L., & Hochstein, J. I. (2017). Munson’s fluid Mechanics.

Hochareon, P. (2003). Development of particle image velocimetry (PIV) for wall shear stress estimation within a 50cc Penn State artificial heart ventricular chamber (thesis).

Hose, D. R., & Doyle, B. J. (2017). Modelling of the cardiovascular system. Cardiovascular Biomechanics, 193–205. https://doi.org/10.1007/978-3-319-46407-7_10

Hoskins, P. R., & Hardman, D. (2017). Blood and blood flow. In Springer eBooks (pp. 37–63). https://doi.org/10.1007/978-3-319-46407-7_3

Hoskins, P. R., & Hose, D. R. (2017). The arterial system I. Pressure, flow and stiffness. In Springer eBooks (pp. 65–81). https://doi.org/10.1007/978-3-319-46407-7_4

Hoskins, P. R., Semple, S., White, P. J., & Richards, J. H. (2011). Imaging of aneurysms. In Springer eBooks (pp. 35–65). https://doi.org/10.1007/8415_2010_64

Hoskins, P. R. (2017). Introduction to cardiovascular biomechanics. In Springer eBooks (pp. 25–35). https://doi.org/10.1007/978-3-319-46407-7_2

Israel, R. J., & Rosner, D. E. (1982). Use of a Generalized Stokes Number to Determine the Aerodynamic Capture Efficiency of Non-Stokesian Particles from a Compressible Gas Flow. Aerosol Science and Technology, 2(1), 45–51. https://doi.org/10.1080/02786828308958612

Jeong, J., & Hussain, F. (1995). On the identification of a vortex. Journal of Fluid Mechanics, 285, 69–94. https://doi.org/10.1017/s0022112095000462

Karthikesalingam, A., Holt, P. R., Vidal-Diez, A., Ozdemir, B. A., Poloniecki, J., Hinchliffe, R. J., & Thompson, M. (2014). Mortality from ruptured abdominal aortic aneurysms: clinical lessons from a comparison of outcomes in England and the USA. The Lancet, 383(9921), 963–969. https://doi.org/10.1016/s0140-6736(14)60109-4

Kazi, M., Thyberg, J., Religa, P., Roy, J., Eriksson, P., Hedin, U., & Swedenborg, J. (2003). Influence of intraluminal thrombus on structural and cellular composition of abdominal aortic aneurysm wall. Journal of Vascular Surgery, 38(6), 1283–1292. https://doi.org/10.1016/s0741-5214(03)00791-2

Kelsey, L. J., Powell, J. T., Norman, P., Miller, K., & Doyle, B. J. (2016). A comparison of hemodynamic metrics and intraluminal thrombus burden in a common iliac artery aneurysm. International Journal for Numerical Methods in Biomedical Engineering, 33(5), e2821. https://doi.org/10.1002/cnm.2821

Khoury, G., Schlatter, P., Noorani, A., Fischer, P., Brethouwer, G., & Johansson, A. V. (2013). Direct numerical simulation of turbulent pipe flow at moderately high Reynolds numbers. Flow, Turbulence and Combustion, 91(3), 475–495. https://doi.org/10.1007/s10494-013-9482-8

Kim, G., Lee, S. K., & Kim, C. D. (2021). Assessment of the physical, mechanical, and tribological properties of PDMS thin films based on different curing conditions. Materials, 14(16), 4489. https://doi.org/10.3390/ma14164489

Kuivaniemi, H., Ryer, E. J., Elmore, J. R., & Tromp, G. (2015). Understanding the pathogenesis of abdominal aortic aneurysms. Expert Review of Cardiovascular Therapy, 13(9), 975–987. https://doi.org/10.1586/14779072.2015.1074861

Kundu, P. K., & Cohen, I. M. (2010). Fluid Mechanics. Academic Press.

Lamb, H. (1945). Hydrodynamics. Courier Corporation

Lederle, F. A. (2011). The rise and fall of abdominal aortic aneurysm. Circulation, 124(10), 1097–1099. https://doi.org/10.1161/circulationaha.111.052365

Levesque, M. J., Liepsch, D., Moravec, S., & Nerem, R. S. (1986). Correlation of endothelial cell shape and wall shear stress in a stenosed dog aorta. Arteriosclerosis, 6(2), 220–229. https://doi.org/10.1161/01.atv.6.2.220

Loudon, C., & Tordesillas, A. (1998). The use of the dimensionless Womersley number to characterize the unsteady nature of internal flow. Journal of Theoretical Biology, 191(1), 63–78. https://doi.org/10.1006/jtbi.1997.0564

Musker, A. J. (1979). Explicit expression for the smooth wall velocity distribution in a turbulent boundary layer. AIAA Journal, 17(6), 655–657. https://doi.org/10.2514/3.61193

Mutlu, O., Salman, H. E., Al-Thani, H., El-Menyar, A., Qidwai, U. A., & Yalcin, H. C. (2023). How does hemodynamics affect rupture tissue mechanics in abdominal aortic aneurysm: Focus on wall shear stress derived parameters, time-averaged wall shear stress, oscillatory shear index, endothelial cell activation potential, and relative residence time. Computers in Biology and Medicine, 154, 106609. https://doi.org/10.1016/j.compbiomed.2023.106609

Nitsche, M. A. (2006). Vortex Dynamics. In Elsevier eBooks (pp. 390–399). https://doi.org/10.1016/b0-12-512666-2/00254-6

Nordon, I. M., Hinchliffe, R. J., Loftus, I., & Thompson, M. (2010). Pathophysiology and epidemiology of abdominal aortic aneurysms. Nature Reviews Cardiology, 8(2), 92–102. https://doi.org/10.1038/nrcardio.2010.180

Petersson, S., Dyverfeldt, P., & Ebbers, T. (2012). Assessment of the accuracy of MRI wall shear stress estimation using numerical simulations. Journal of Magnetic Resonance Imaging, 36(1), 128–138. https://doi.org/10.1002/jmri.23610

Saffman, P. G. (1993). Vortex Dynamics. Cambridge University Press.

Salman, H. E., Ramazanli, B., Yavuz, M., & Yalcin, H. C. (2019). Biomechanical investigation of Disturbed Hemodynamics-Induced tissue degeneration in abdominal aortic aneurysms using computational and experimental techniques. Frontiers in Bioengineering and Biotechnology, 7. https://doi.org/10.3389/fbioe.2019.00111

Salsac, A., Sparks, S. R., Chomaz, J., & Lasheras, J. C. (2006). Evolution of the wall shear stresses during the progressive enlargement of symmetric abdominal aortic aneurysms. Journal of Fluid Mechanics, 560, 19. https://doi.org/10.1017/s002211200600036x

Sibson, R. (1981). "A brief description of natural neighbor interpolation (Chapter 2)". In V. Barnett (ed.). Interpreting Multivariate Data. Chichester: John Wiley. pp. 21–36

Stamatopoulos, C., Mathioulakis, D., Papaharilaou, Y., & Katsamouris, A. N. (2010). Experimental unsteady flow study in a patient-specific abdominal aortic aneurysm model. Experiments in Fluids, 50(6), 1695–1709. https://doi.org/10.1007/s00348-010-1034-6

Svensjö, S., Björck, M., Gürtelschmid, M., Gidlund, K. D., Hellberg, A., & Wanhainen, A. (2011). Low prevalence of abdominal aortic aneurysm among 65-Year-Old Swedish men indicates a change in the epidemiology of the disease. Circulation, 124(10), 1118–1123. https://doi.org/10.1161/circulationaha.111.030379

Swedenborg, J., & Eriksson, P. (2006). The intraluminal thrombus as a source of proteolytic activity. Annals of the New York Academy of Sciences, 1085(1), 133–138. https://doi.org/10.1196/annals.1383.044

Tropea, C., Yarin, A. L., & Foss, J. F. (2007). Springer Handbook of Experimental Fluid Mechanics. Springer Science & Business Media.

Türk, S. (2021). Characterization of wall shear stress in abdominal aortic aneurysm phantom using particle image velocimetry. METU.

Van Ooij, P., Potters, W. V., Guédon, A. C. P., Schneiders, J., Marquering, H. A., Majoie, C. B. L. M., VanBavel, E., & Nederveen, A. J. (2013). Wall shear stress estimated with phase contrast MRI in an in vitro and in vivo intracranial aneurysm. Journal of Magnetic Resonance Imaging, 38(4), 876–884. https://doi.org/10.1002/jmri.24051

Wanhainen, A., Hultgren, R., Linné, A., Holst, J., Gottsäter, A., Langenskiöld, M., Smidfelt, K., Björck, M., & Svensjö, S. (2016). Outcome of the Swedish Nationwide Abdominal Aortic Aneurysm Screening Program. Circulation, 134(16), 1141–1148. https://doi.org/10.1161/circulationaha.116.022305

Wilson, K., Lee, A. J., Hoskins, P. R., Fowkes, F. G. R., Ruckley, C., & Bradbury, A. (2003). The relationship between aortic wall distensibility and rupture of infrarenal abdominal aortic aneurysm. Journal of Vascular Surgery, 37(1), 112–117. https://doi.org/10.1067/mva.2003.40

Yousif, M. Y., Holdsworth, D. W., & Poepping, T. L. (2009). Deriving a blood-mimicking fluid for particle image velocimetry in sylgard-184 vascular models. https://doi.org/10.1109/iembs.2009.5334175

Yu, S. (2000). Steady and pulsatile flow studies in Abdominal Aortic Aneurysm models using Particle Image Velocimetry. International Journal of Heat and Fluid Flow, 21(1), 74–83. https://doi.org/10.1016/s0142-727x(99)00058-2